박 사 학 위 논 문

Ph.D. Dissertation

체외 질병모델의 동적 특성 분석

Dynamic Behaviors of *In Vitro* Pathophysiological Models

2023

김 지 원 (金 智 媛 Kim, Jiwon)

한 국 과 학 기 술 원

Korea Advanced Institute of Science and Technology

박 사 학 위 논 문

체외 질병모델의 동적 특성 분석

2023

김 지 원

한 국 과 학 기 술 원

기계공학과

체외 질병모델의 동적 특성 분석

김 지 원

위 논문은 한국과학기술원 박사학위논문으로
학위논문 심사위원회의 심사를 통과하였음

2022년 12월 9일

심사위원장 신 현 정 (인)
심 사 위 원 김 인 준 (인)
심 사 위 원 서 재 명 (인)
심 사 위 원 전 성 윤 (인)
심 사 위 원 김 형 수 (인)

Dynamic Behaviors of *In Vitro* Pathophysiological Models

Jiwon Kim

Advisor: Jennifer H. Shin

A dissertation/thesis submitted to the faculty of
Korea Advanced Institute of Science and Technology in
partial fulfillment of the requirements for the degree of
Doctor of Philosophy in Electrical Engineering

Daejeon, Korea
December 9, 2022

Approved by

Jennifer H. Shin
Professor of Mechanical Engineering

The study was conducted in accordance with Code of Research Ethics[1)].

1) Declaration of Ethical Conduct in Research**:** I, as a graduate student of Korea Advanced Institute of Science and Technology, hereby declare that I have not committed any act that may damage the credibility of my research. This includes, but is not limited to, falsification, thesis written by someone else, distortion of research findings, and plagiarism. I confirm that my dissertation contains honest conclusions based on my own careful research under the guidance of my advisor.

DME

김지원. 체외 질병모델의 동적 특성 분석. 기계공학과. 2023년. 85+ix 쪽. 지도교수: 신현정. (영문 논문)

Jiwon Kim. Dynamic Behaviors of In Vitro Pathophysiological Models. Department of Mechanical Engineering. 2023. 85+ix pages. Advisor: Jennifer H. Shin. (Text in English)

초 록

본 학위논문에서는 세포의 분석에 역학적 관점을 도입하여 다양한 생리 · 병리현상의 기작을 조명한다. 우선 체내 미세환경조건을 반영한 체외 모델을 확립하였으며, 주로 생세포 이미징을 통해 세포의 이동과 변형에 관련된 변수를 추출하였다. 이를 통하여, 첫째, 지방세포 탈분화 과정의 지질방울 배출 기작을 밝히고 지방세포 간 지질 교환 현상에 관해 보고한다. 둘째, 상이한 강성환경에 노출시킨 되어 서로 다른 특성을 획득한 난소암 세포가 전이과정을 모사한 체외모델 내에서 복수의 계대, 배양 방식을 관통하는 기계적 기억력을 지속함을 보고한다. 셋째, 유방암 스페로이드 모델이 그 제작 방식에 따라 침습 시 서로 다른 결집력을 보임을 보고한다. 넷째, 교모세포종의 스페로이드 모델을 확립하고, 그 다중모드 침습 기작에 대하여 보고한다. 네 챕터에 아우른 위 결과들은 생리현상의 분석에서 정량화가 가능한 여러 역학 지표들이 유전체 및 단백질 발현량 기반 분석 못지않게 강력한 무기가 될 수 있음을 시사한다.

핵 심 낱 말 세포역학, 메케노바이올로지, 지방세포 탈분화, 암 침습, 기계적 기억력

Abstract

This dissertation elucidates the underlying mechanisms of various pathophysiological phenomena, bringing a physical perspective into cell analysis. To do so, we started with establishing *in vitro* models replicating the *in vivo* microenvironments, and parameters describing cellular migration and deformations were extracted from the models primarily using live-cell imaging. In this way, we report the followings in each of the four chapters: First, we explicate the mechanisms of lipid droplet secretion during adipocyte dedifferentiation and report the phenomena of lipid exchange between adipocytes. Second, we reveal that ovarian cancer cells exposed to substrates of different stiffnesses acquire different characteristics and retain their mechanical memory over multi-passages and culture conditions in an *in vitro* model that simulates the peritoneal metastatic process. Third, we find that the spheroid models of breast cancer exhibit different levels of collectiveness during invasion depending on the protocols chosen for the spheroid generation. Finally, we establish spheroid models of glioblastoma and investigated their multimodal invasion mechanisms. The above results suggest that the physical indicators quantifying the physical aspects of cells can be as powerful as the traditional cell analysis based on the expression level of genes or proteins in the study of various pathophysiological phenomena.

Keywords Cell mechanics, Mechanobiology, Adipocyte dedifferentiation, Cancer invasion, Mechanical memory

Contents

List of Tables

List of Figures

Chapter 1. Introduction

1.1 Dynamic Behaviors of Cellular Pathophysiology

Cells are generally perceived as biological or, more broadly, chemical entities. The majority of the publications on cells are concerned with how the biochemical factors within and outside the cells affect cells' ability to survive, proliferate, or differentiate in response to external stimuli, which are also *biochemical*. While there exist cellular responses that are considered to be "physical," such as how fast cells move, how well they deform, and how strongly they bind to each other or the environment, it was not until very recent that researchers began to perceive the cells as a mechanical entity. With the remarkable advancement in optical tools and microfabrication technologies which allow the detection and manipulation of cellular components down to the single-molecule level, we began to appreciate small changes in shapes and motions, i.e., the mechanical properties of the cells, in response to external stimuli, which are now inclusive of both biochemical and *mechanical*. Mechanics is a discipline of science devoted to the action of external *forces* on objects that lead to changes in *shapes* and *motions*. Cells, being a subject of mechanics, sense and respond to the applied external forces by adjusting their shape and motile properties. These cellular alterations can reflect the changes in the *pathophysiological* state of the cells. More detailed demonstrations of the mutual connections will be explored with examples below.

1.1.1 Perspective on the cellular shape

Cellular shape, which can be induced by internal/external forces and the change, is known to correlate with cellular states. Cellular plasticity[a] is a common term used in biology that refers to the cells' inherent property of shifting from one state to another. One powerful evidence of cellular plasticity is found in the developmental processes. Upon fertilization, a single zygote divides into a number of smaller cells while maintaining the total volume up to the morula stage. When the zygote divides only once to produce two cells, one of those cells can develop completely even after another cell is removed [1]. After one or two divisions, when the number of cells reaches four or eight, a single cell is not capable of carrying out full development on its own [2]. However, when it is reintroduced into the chimeras of the remaining seven cells, it may participate in the formation of a normal organism while contributing to every single of the cells, proving that the cells at this stage are fully maintaining their developmental potentials, confirming the homogeneity of the 8 cells [3]. However, another division into the 16-cell-stage halts the replaceability between the cells. Starting from the 16-cell stage, the cells at the boundary take distinct shapes with a polarity (Fig.1.1a) as described by the classic "polarization" model (Fig.1.1b) [4]. Here, the polarized outer

[a] Cellular plasticity refers to the cells' inherent property of shifting readily from one state to another, and it should not be confused with the concept of plasticity defined in solid mechanics, referring to a property where the shape of a solid object changes permanently due to the stresses over a critical yield strength.

cells deactivate the Hippo signaling pathway, while the inner apolar cells activate it (Fig.1.1c), leading to the very first cell fate decision [5].

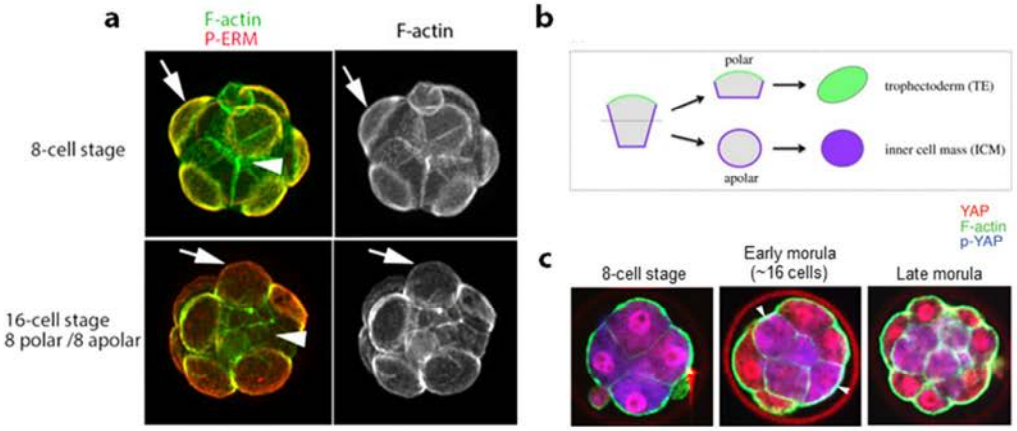

Figure 1.1 Mechanical perturbation between the 8-cell stage and 16-cells stage. a Morphological symmetry at the 8-cell stage breaks at 16-cell stage [5]. **b** Polarization model [4]. **c** YAP expresses similar in every cell in 8-cell stage but not in 16-cell stage. Nuclear expression levels of polar cells exceed that of apolar cells at 16-cell stage [5].

Previously, Waddington depicted the journey of differentiation from the pluripotent cell to mature somatic cells with the landscape with valleys and ridges (Fig.1.2a) [6]. While the essential message of the metaphor remains unchanged, several arrows have been added over time to indicate new alternative paths of going over the ridge (transdifferentiation) or climbing back along the valley (dedifferentiation) (Fig.1.2b) [7].

Another remarkable example of mutual interactions between cellular morphology and cellular state is found in mature adipocytes that feature a unique differentiation with a dramatic shape change. Adipocytes originate from mesenchymal stem cells and undergo adipogenesis to produce fully differentiated adipocytes. Unlike the rest of the cells, adipocytes feature huge volumes and globular forms due to the lipid droplets that make up most cytoplasm. The distinctive morphology of adipocytes makes it easy to recognize when the cellular state is altered.

Emerging evidence suggests that mature adipocytes have a high level of plasticity, filling large knowledge gaps in a variety of vital physiological processes such as lactation, hair follicle cycling, and wound healing [8]. Wang *et al*. reported that adipocytes, accounting for most of the virgin mammary gland tissue, undergo dedifferentiation to demonstrate the signatures of pre-adipocytes during pregnancy when the lactating mammary gland cells develop. After the lactation is over and the mammary gland shrinks, the previously dedifferentiated cells revert into adipocytes, filling up the space where the mammary gland cells have disappeared (Fig.1.2c) [9, 10]. Kruglikov *et al*. found that Hair follicles (HFs) cycling is highly dependent on the extracellular vesicles secreted by dermal white adipose tissues (dWAT) cells of different levels of maturation and morphology (Table.1.1) [11, 12]. HFs have pocket-shaped structures where the roots of the hair are provided with nutrients. Normal HFs have three-phased cycles regulated by dWAT cells, namely

the anagen (hair growth), catagen (regression), and telogen (rest) (Fig.1.2d). Adipocyte dedifferentiation is also involved in wound healing. When the skin is injured, the adipocytes around the wound release the lipid contents to become "skinny" adipocytes. Released free fatty acids activate immune responses and recruit capillaries, expediting the healing processes. Meanwhile, the adipocytes undergo lipolysis, dedifferentiate into myofibroblast, and directly support restoring the lost tissue by synthesizing ECM (Fig.1.2e) [13, 14].

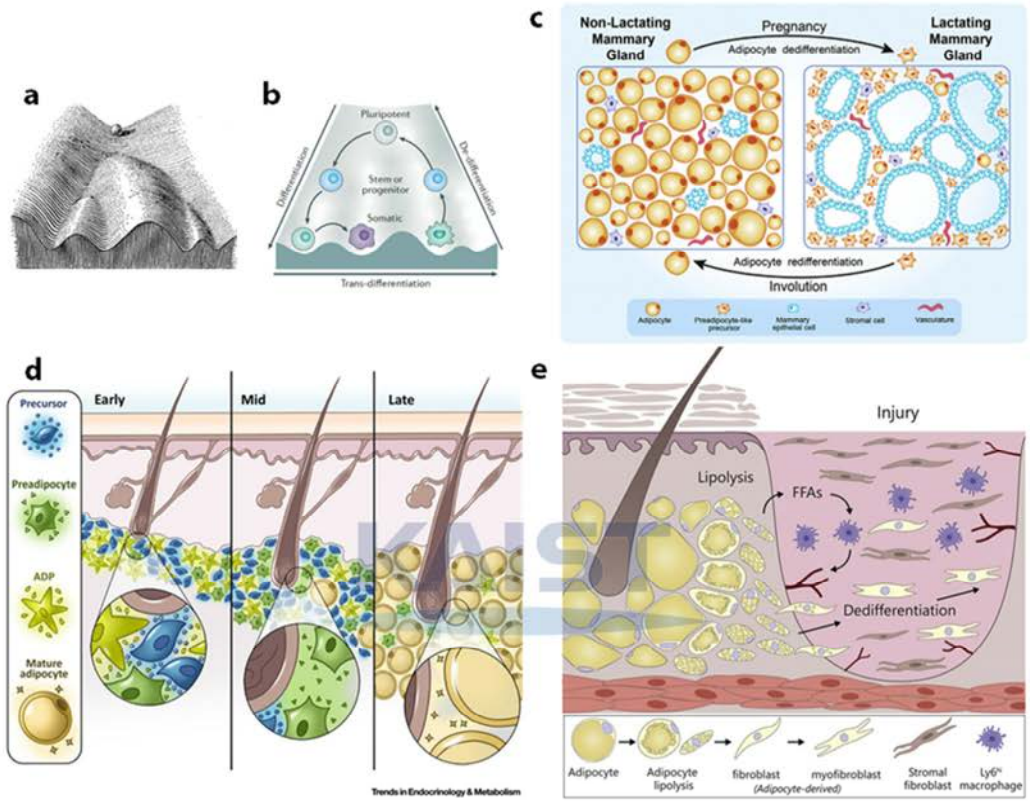

Figure 1.2 Expanded notion of cellular plasticity. a Waddington's epigenetic landscape [6]. **b** Revised version of Waddington's epigenetic landscape [7]. **c** Cyclic dedifferentiation and redifferentiation of mammary adipocyte [10]. d Adipocyte plasticity controlling the HF cycle [12]. **e** Dedifferentiated adipocyte participating in wound healing [14].

Table 1.1 Morphological characteristics and biomarkers involved with adipocyte plasticity [15].

	Skin preadipocytes	→ (Differentiation)	**Mature dermal adipocytes**	→ (Dedifferentiation)	**Skin adipocyte-derived stem cells (ADSCs)**
Morphology	Fibroblast-like		Unilocular with large lipid droplets		Fibroblast-like
Markers	Lin^-, $Sca1^+$, $CD34^+$, $CD29^+$, $Pdgfra^+$, $CD24^-$, $CEBPa^+$		Common adipocyte markers		Lin^-, $Sca1^+$, $CD34^+$, $CD29^+$, $CD24^+$, $Pdgfra^+$

From embryonic development to adipocyte dedifferentiation, the examples of cell plasticity discussed above were all physiological phenomena essential for life activities accompanied by cellular *deformations*. Cells were transformed by the external microenvironments, and the altered cellular state also affected the

surroundings. The cellular deformation is both a cause and a consequence of cellular plasticity simultaneously, as well as an indicator making it recognizable.

1.1.2 Perspective on cellular motility

According to the latest statistics in 2021, a total of 608,570 people died in the entire US region a year, proving that the war on cancer is not over yet. The reason cancer is a threat mainly lies in its metastatic potential. The two-year survival rate for cancer in the lung and bronchus, which caused the most deaths among many cancer types, drastically decreased if it had spread further at the time of diagnosis (Fig.1.3a) [16].

The invasion-metastasis cascade is a complicated sequential and interconnected process that leads to the production of distant secondary tumors and is one of cancer biology's most critical issues, being a new target of drug research (Fig.1.3b) [17].

It is often accepted that the migration and local invasion of cells into the surrounding extracellular matrix start the chain of metastatic events. However, this statement can be true or not, depending on the metastatic route adopted by cancer. When cancer cells spread, they adopt different paths, often depending on their origin. Carcinomas, such as breast cancer, are known to adopt lymphatic systems, whereas sarcomas, such as bone cancer, commonly take the hematogenous route. Tumors that originated in the intraperitoneal organs, i.e., organs contained in the body cavities (Fig.1.4a), prefer the transcoelomic paths. Ovarian cancer is one of the cases [18].

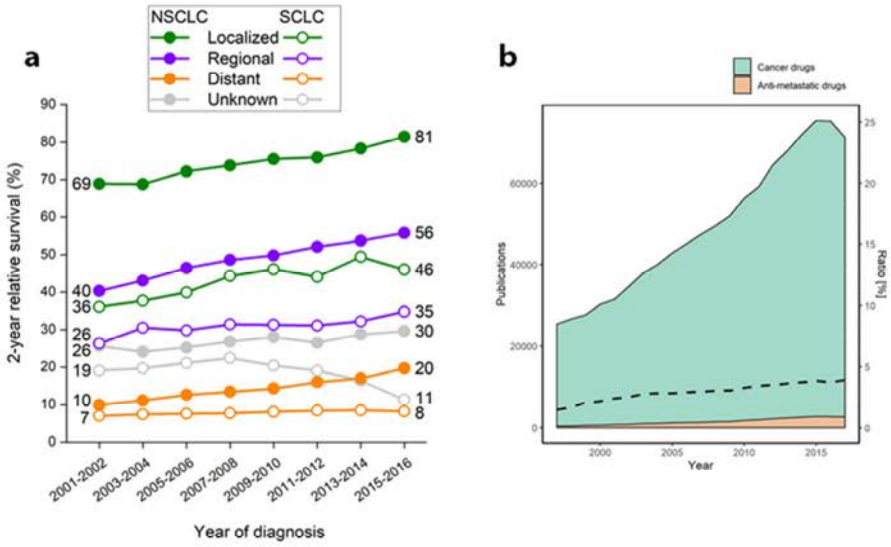

Figure 1.3 Clinical and academical significances of cancer invasion and metastasis. a Trends in 2-Year Relative Survival for Lung Cancer by Subtype and Stage at Diagnosis [16, 17]. **b** Annual publications associated with cancer drugs and antimetastatic drugs [17].

Hematogenous/Lymphatic metastasis, where the circulatory systems are used as conduits for tumor cells, begins with cells losing their polarity and being aggregated into an unorganized mass as they continue to reproduce. The cancer cells recruit stromal cells, particularly fibroblasts, to make them produce and align collagen fibers that will serve as a pathway to blood arteries or lymph vessels. Soon, cancer cells infiltrate into the stroma via perforations in the basement membrane, gaining access to the circulatory system. The action where the cancer cells penetrate surrounding tissues is referred to as invasion. After entering a vessel (intravasation), tumor cells begin to circulate throughout the circulatory system (circulating tumor cell, CTC). When cells discover a niche, they adhere to the vessel wall and eventually escape the vasculature (extravasation). The metastatic process is complete when the cells settle and grow in a new location [19].

On the other hand, in transcoelomic metastasis, invasion belongs to the later step rather than the onset of the metastasis. Unlike the highly occurring breast cancer and lung cancer, ovarian cancer develops at the organ's surface, not displaying notable symptoms. In peritoneal metastasis, cancer cells do not bother to penetrate the dense basement membrane beneath. Instead, TWIST downregulates the cell-cell adhesion molecules like E-cadherin, and the cells shed into the fluid-filled cavity as individual single cells or a clump of multiple cells. The increased interstitial fluid pressure further promotes the loose cells to shed into ascites [18].

Cells that came out from the primary sites would soon encounter hazards from immune surveillance, chemotherapy attack, and anoikis. Among those cells, cells that successfully formed malignant spheroids have higher chances to survive and proceed. The malignant spheroids drift passively by gravity and diaphragmatic movement. As those driving forces apply universally to all patients, there exists a predictable path followed by the floating spheroids, dominantly on the right side of the peritoneal cavity [20]. When surviving spheroids in the ascites come into contact with the mesothelial layer or the underlying stroma, multiple adhesion molecules, including CD44 and integrin β1, establish anchorage on the layer, settling down the spheroids (Fig.1.4b). It is known that the milky spots, where the submesothelial stroma is exposed, are preferred by the spheroids over the intact mesothelial lining. The reason for the tropism still has much to be explored, but one of the plausible explanations is that the abundant collagen I fibers facilitate the implantation of spheroids [21]. Besides, a recent study ascribed this tropism to an unexpected subject. Neutrophils, activated by inflammatory factors derived from the cancer cells, extrude chromatin webs called neutrophil extracellular traps (NETs). NETs can mechanically trap the floating cells in the abdomen (Fig.1.4c). Mice models bearing ovarian cancer and patient at the early stage of ovarian cancer were found to have the NETs in their omentum [22].

When the spheroids settle on the intact mesothelial lining, they use traction forces activated by the integrin-talin-myosin axis to remove the native mesothelial cells beyond simply binding to the outer surface. The exercise of metastasizing cells is referred to as mesothelial clearance and facilitates the further migration into other organs encapsulated by the layer making direct access to stroma underneath the mesothelial lining.

After all the processes, cancer cells reach the submesothelial stroma and invade into surroundings, aided by proteases such as matrix metalloproteinases (MMPs), completing the peritoneal metastasis [23].

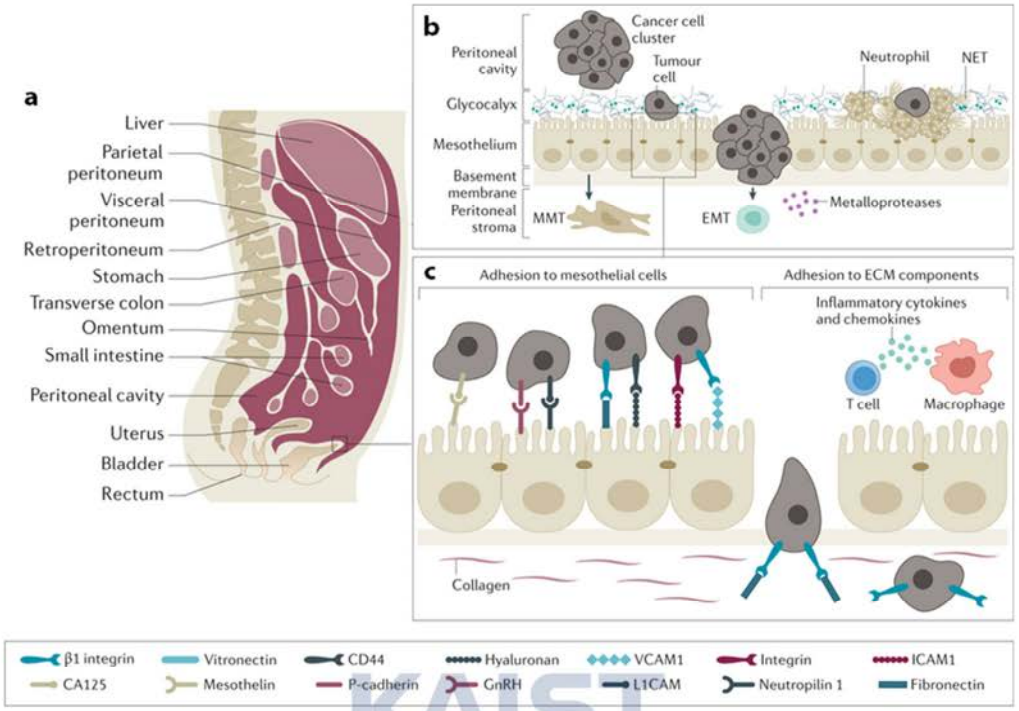

Figure 1.4 Metastatic spread to the peritoneum [18]. **a** Anatomy of the peritoneal cavity. **b** Adhesion of malignant spheroids onto the mesothelial lining and the underneath stroma. **c** Receptor-ligands participating in cell-cell binding and cell-substrate binding in mesothelial metastasis.

Both metastatic routes exploiting the circulatory systems of the body cavity involve cancer invasion at the beginning or end, emphasizing the significance of cellular migration in pathological progressions. The molecular mechanisms underlying the motile phenotypes of metastasizing cancer cells have been explained by the epithelial-mesenchymal transitions (EMTs). EMT is a sophisticated process where the epithelial cells lose multiple features associated with the composition/alignment of cytoskeletons, adherens junctions, and apical-basal polarity while gaining markers and phenotypes characterizing mesenchymal cells, including spindle-like morphologies, front-real polarity, and enhanced motility, and so on [24]. Classic theories describe the EMT as a category of cellular *plasticity* driving cancer metastasis, along with the mesenchymal-epithelial transition (MET), the revert program; where the dissemination of cancer cells from the primary solid tumor is initiated by the EMT, and colonization at the secondary lesion is completed by MET. However, with the emerging evidence proving that such a dichotomy is invalid (Fig.1.5a), the concept and scope of EMT in metastasis have been expanded and subdivided [24]. The evolution of theory includes recognizing partial or hybrid EMT states and acknowledging the heterogeneous extent of EMT among cells consisting of a collectively invading cellular cluster. Indeed, tumor cells expressing combinations of both epithelial and mesenchymal markers excel in circulation (Fig.1.5b), colonization, and development of metastasis [25, 26]. Moreover, it has been turned out that a collective strand penetrating

surroundings consists of cells with different extents of EMT for a more strategic invasion. The leader cell can be a mesenchymal cell that underwent full EMT, cells in the hybrid state between epithelial and mesenchymal cells, or even a basal cell considered a pure epithelial cell (Fig.1.5c) [27].

Besides the EMT state, a more recent study added a metabolic point of view in interpreting the regulating mechanisms of cancer invasion. In collectively migrating cancer cells, leader cells consuming more glucose are substituted by the follower cells when it depletes the energy (Fig.1.5d) [28, 29].

The series of findings are extending our understanding of the deformation and migration of cells in pathophysiological contexts ranging from embryonic development to cancer invasion, that is to say, from the cradle to the grave. The next section will address a current research trend that attempts to illustrate cellular state using those mechanical indices rather than looking into every single base in the genome.

1.2 Paradigm Shift to Cell Mechanics

Pathophysiological phenomena arise from genetic and/or epigenetic alterations. Most alterations are temporary, harmless, and even requisite. However, the accumulation of those alterations likely raises the risk of cancer, underlining the significance of tracking the history of genetic/epigenetic alterations [30].

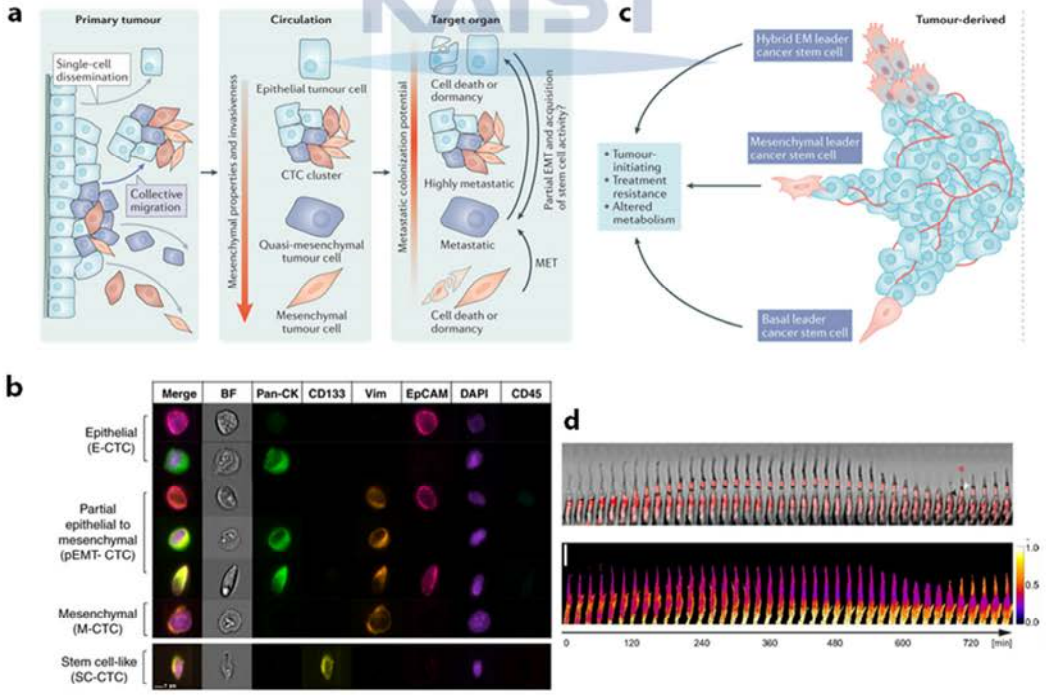

Figure 1.5 Expanded and subdivided concept of EMT in cancer metastasis. a EMT heterogeneity during metastatic colonization [24]. **b** Circulating tumor cells expressing various EMT markers simultaneously [26]. **c** Tumor derived leader cells expressing various EMT states [27]. **d** Follower cells taking over the leader position when the cellular energy level of leader cell decreases [28].

However, it has been challenging to detect those alterations due to the extremely rare frequency of mutations and limitations in technological advances. In addition to the rarity, the size of data also hinders the inspection as the genome size of a single human cell is over 700MB. Considering the epigenetic changes and the intercellular heterogeneity, the number of cases of abnormalities would be innumerable, with some of them having nothing to do with the pathological progress, exacerbating the chaos.

As a result, researchers are working on more efficient prediction approaches rather than struggling with the massive amount of data. Recently, Pei-Hsun Wu *et al*. reported that cellular morphology could be a surrogate indicator of the tumorigenic and metastatic potential of breast cancer. They established 14 single-cell clusters (SCCs) from a parental heterogeneous cell line and extracted morphological features from the SCCs. The features include quantitative values such as area, perimeter, elongation, and various moments defined for specific purposes. One feature vector bearing all the feature values was assigned per one cell and then sorted into one of seven classes. Each SCC was hierarchically classified into 6 morphotypes based on the similarity of the frequencies of the 7 classes that make up each cluster (Fig.1.6a). For comparison, the 14 SCCs were again classified based on the metastatic function measured with *in vivo* experiments (Fig.1.6b,c) and gene expression landscape obtained with microarray transcriptome profiling (Fig.1.6d).

The intriguing point was that the 14 SCCs displayed similar classification patterns regardless of the criteria (Fig.1.6e), verifying that there are mutual correlations between morphotypes, gene expression, and cellular aggressiveness. The morphotyping required only 216 features that were extracted from the cell and nucleus morphology, which is a huge condensation compared to the gene expression landscape of the cells. Besides reducing time and cost, the extraction of mechanical indices based on image analysis has advantages, such as being able to follow the spatiotemporal changes even without cell lysis [31].

The result, however, does not claim that the molecular mechanisms and the biochemical analyses are pointless or inefficient, as the central dogma governs cellular states. The nano-scaled objects still remain the primary goal required to solve the yet-unsolved biological mysteries, but the development speed of assay techniques and data science could not keep up with the growing demands. The mechanical point of view promises high-quality predictions on cellular behaviors *in vivo* with currently available methodologies, being more competent when dealing with phenomena inseparable from deformation or migration, such as cellular plasticity or cancer invasion. While the *morphology* of the cells was mainly discussed as an example of mechanical features, there are other phenotypes associated with cell mechanics, which will be explored in the next section.

1.3 Quantification of Dynamic Behaviors

Cell motility entails plenty of information reflecting cellular states, and the *in vitro* assays can provide a good quantifiable estimation of *in vivo* motility (Fig.1.7). Features directly describing the motility, such as

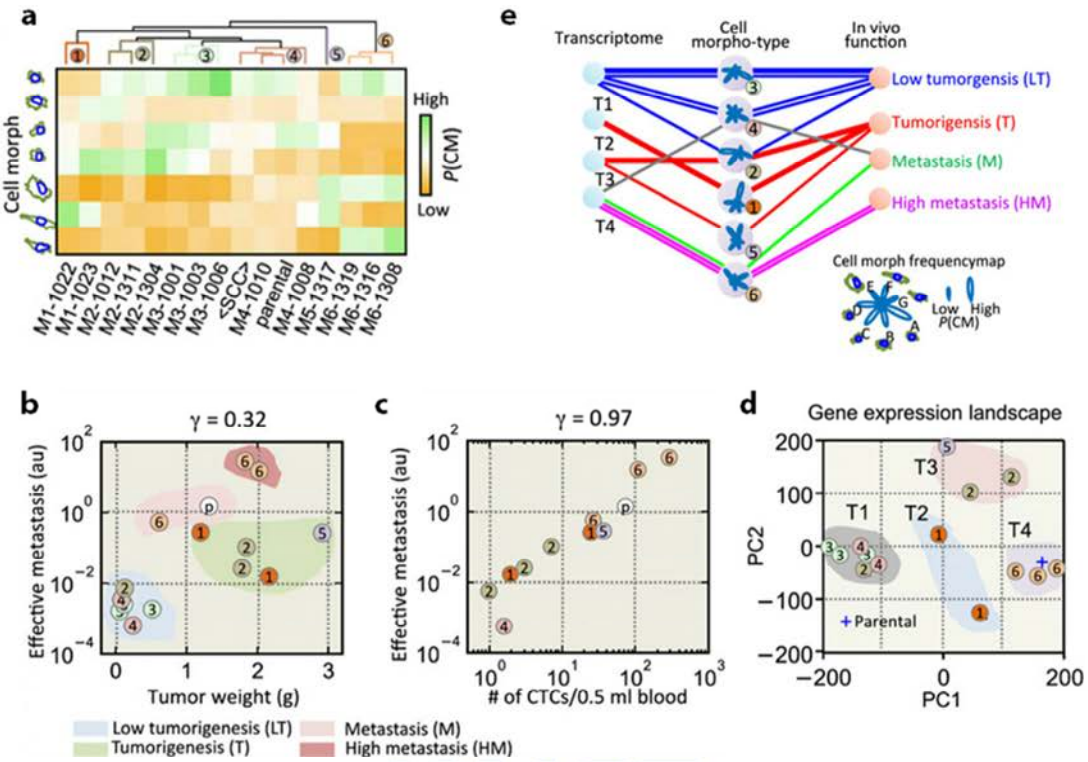

Figure 1.6 Mutual correlation between the cell morphotype, transcriptome, and *in vivo* function[31]. **a** Unsupervised hierarchical clustering of SCCs based on their morphotypes. **B** Unsupervised clustering by the tumor weight and extent of lung metastasis. **c** Arrangement of morphotype-based clusters in a scatter plot showing number of circulating tumors and extent of lung metastasis. **d** Unsupervised clustering by gene expression profile. **e** Diagram showing mutual relations between morphotype, transcriptome, and *in vivo* functions.

velocity and directionality, can be quantified either by manual tracking, or by computational methods like single-particle tracking (SPT), digital particle image velocimetry (dPIV), and optical flow, especially in the case of collective migration. dPIV, the most widespread method, assumes that cells move in a continuous way where the neighboring features of the image would keep similar relative positions from frame to frame. Using correlation functions, dPIV finds how each subregion of the image has been displaced in a subsequent frame to determine an approximate trajectory of the cells in each subregion. The displacement field can be converted into the velocity field [32, 33]. These features can mirror the level of spontaneous motility inherent to individual cells in a comparative way. When the *in vitro* assay involves environmental modifications or any kind of external stimuli, readouts on motile phenotypes can display how the responses of the cells are sensitive to the input and whether the responses are biased or not.

Beyond the visible parameters, tractions exerted by the cells and monolayer stresses existing along the intercellular boundaries also can be measured. TFM measures force by observing the deformation of the elastic substrate to which the sample is adhered, not that of the sample itself. Elastic substrates embedded with fluorescent particles are required for tracking the deformation of the substrate. When a spot on the substrate is displaced by a distance **u**, the stress $\boldsymbol{\sigma}$ exerted to generate the displacement can be calculated

by Hooke's law and the force equilibrium equation in tensor space. The displacement **u** can be calculated by conducting dPIV on the fluorescent particles in the substrate, and the spring constant can be derived from the size of the subset window and material properties of the substrates. Monolayer stresses can also be computed by applying force equilibrium between the tractions obtained previously and the cell-cell stresses. Quantitatively measured cellular forces have been contributing to unraveling the locomotive mechanisms of cells in various pathophysiological contexts, including cancer, musculoskeletal development, and immune responses [33, 34].

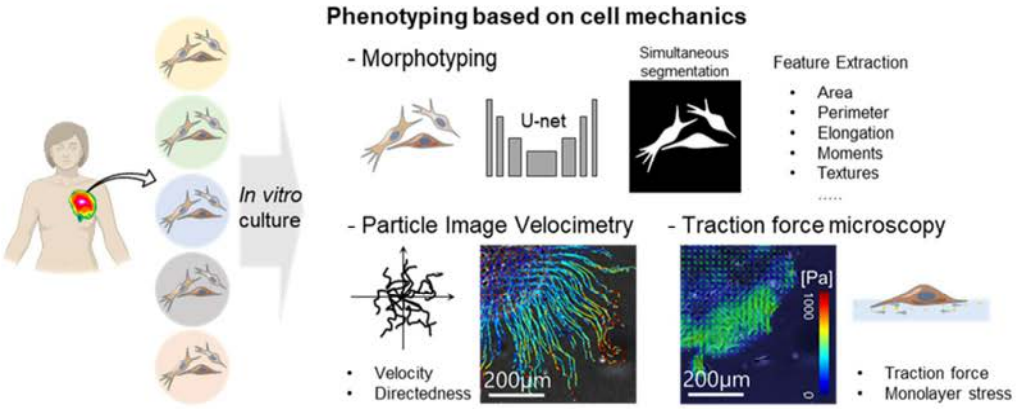

Figure 1.7 Quantification methods for cellular deformation and migration.

This dissertation elucidates the underlying mechanisms of various pathophysiological phenomena, bringing a physical perspective into cell analysis. To do so, we started with establishing *in vitro* models replicating the *in vivo* microenvironments, and parameters describing cellular migration and deformations were extracted from the models primarily using live-cell imaging. In this way, we report the followings in each of the four chapters: First, we explicate the mechanisms of lipid droplet secretion during adipocyte dedifferentiation and report the phenomena of lipid exchange between adipocytes. Second, we reveal that ovarian cancer cells exposed to substrates of different stiffnesses acquire different characteristics and retain their mechanical memory over multi-passages and culture conditions in an *in vitro* model that simulates the peritoneal metastatic process. Third, we found that the spheroid models of breast cancer exhibit different levels of collectiveness during invasion depending on the protocols chosen for the spheroid generation. Finally, we established spheroid models of glioblastoma and investigated their multimodal invasion mechanisms. The above results suggest that the physical indicators quantifying the physical aspects of cells can be as powerful as the traditional cell analysis based on the expression level of genes or proteins in the study of various pathophysiological phenomena.

Chapter 2. Mature adipocyte plasticity regulated by dynamic actin remodeling[b]

2.1 Introduction

As an endocrine and energy-storing organ, adipose tissues play crucial roles in the maintenance of metabolic homeostasis [8, 35]. In addition, adipose tissues can undergo adaptive remodeling in response to a wide range of developmental, physiological, and pathological cues. Notably, the cellular plasticity of mature adipocytes is widely recognized to play a critical role in this process [36].

Adipocytes originate from mesenchymal stem cells and undergo adipogenesis to produce fully differentiated adipocytes. Adipogenesis is divided mainly into two stages: (1) commitment of mesenchymal stem cell (MSC) to the adipocyte lineage and (2) terminal differentiation of the preadipocytes to mature adipocytes [37]. Here, the term *terminal* implies that the process cannot be reversed once differentiation is completed and cells acquire a specific function and morphology. However, recent studies revealed that the *reversion, or dedifferentiation,* of a mature adipocyte into a cell with greater developmental potential, such as a preadipocyte or MSC, can occur both *in vitro* and *in vivo* [8]. During pregnancy, for example, adipocytes in the maternal mammary gland have been shown to dedifferentiate into fibroblast-like cells. Furthermore, after weaning, the lactating mammary glands undergo involution, during which dedifferentiated adipocytes re-differentiate into mature adipocytes and displace regressing mammary gland tissue [9].

The process of mature adipocyte dedifferentiation is important from both a scientific and translational perspective. Dedifferentiated adipocytes, by definition, acquire broader developmental potential, implying that they can be differentiated into other cells besides adipocytes [38]. For example, dedifferentiated adipocyte-derived progeny cells, or DFATs, have been shown to differentiate into osteoblasts [39], chondrocytes [40], smooth muscle cells [41], and endothelial cells [42]. DFATs are emerging as an attractive material for tissue engineering due to their multilineage potential and accessibility of adipose tissue. Besides, adipocytes are more accessible than MSCs from bone marrow, making them considerably easier to harvest with fewer adverse effects [43].

The phenomena of LD secretion by adipocytes has recently been documented as a central event of the dedifferentiation process whereby adipocytes transform into a delipidated state through a mechanism distinct from lipolysis [44, 45]. Recently, electron micrographs of fat tissue biopsies from obese individuals

[b] Contents of this chapter have been published in *Lab on a Chip* with a title of "Ceiling culture chip reveals dynamic lipid droplet transport during adipocyte dedifferentiation via actin remodeling", authored by Jiwon Kim[§], Kun-Young Park[§], Sungwoo Choi, Ung Hyun Ko, Dae-Sik Lim, Jae Myoung Suh[*], and Jennifer H. Shin[*] (§ Equal distribution). The published article and supplementary videos are available at doi: https://doi.org/10.1039/d2lc00428c.

revealed the presence of *in vivo* dedifferentiated adipocytes that had also undergone LD secretion to acquire the delipidated phenotype [46]. Despite its physiological importance, however, the molecular and cellular mechanisms of adipocyte dedifferentiation and LD secretion are poorly understood.

The physical resemblance between DFATs and primary fibroblasts, which are inherent to the stromal vascular fraction (SVF) of adipose tissues, is a major hindrance to studying adipocyte dedifferentiation. Therefore, we utilized *Adipoq*-Cre*;* mT/mG mice to overcome the issue of fibroblast contamination. Because only adipocytes express EGFP in *Adipoq*-Cre*;* mT/mG mice, we were able to unambiguously track the cells that were dedifferentiated from adipocytes, eliminating any concerns regarding fibroblast contamination.

Another challenge of studying primary adipocytes is their low specific gravity, which causes them to float in cell culture media. Various culture techniques have emerged to address this problem since the introduction of Sugihara's ceiling culture method in 1986 [47]. In 2017, Julie Anne Côté *et al*. introduced a ceiling culture model that can be inserted into a six-well plate [48]. This model consists of plastic bushing and detachable coverslips, allowing more flexible designs of experiments. More recently, Matthew J. Harms *et al*. adopted the commercialized trans-well to develop a new platform for adipocyte culture, termed MAAC, which significantly improved adipocyte viability in long-term culture [49]. Akiyo Yokomizo *et al*. took a unique approach based on coaxial microfibers where adipocyte-embedded collagen gel was fabricated as a core fiber sheathed by a layer of permeable alginate gel [50]. While extant methods provide suitable conditions for *in vitro* culture of primary adipocytes, real-time live imaging remains challenging due to the opacity in some of these constructs as well as the geometrical constraints due to microscope focal length. Alternately, methods for the *in vitro* induction of mature adipocytes from adherent cells are being intensively researched. Using the Greek letter 'σ'-shaped microwells, Kim *et al*. were able to capture buoyant adipocyte spheroids made from the human adipose-derived stem cells [51]. Pope et al. utilized fiber networks to hold differentiated mature adipocytes while allowing them to grow into the size of the ones found in obese adults [52]. However, the gene expression profiles of differentiated preadipocytes and primary adipocytes are inextricably distinct [49], and cellular modalities in these limited contexts were only suitable for observing the phenomenon of differentiation, not the reverse "dedifferentiation" process.

Here, we introduce a soft lithography-based, multi-layered ceiling culture platform that allows culturing of non-adherent, floating cell types. To address prior drawbacks, we designed a system where all parts of the chip are transparent, and the height of the ceiling of the cell culture chamber is only 200μm, which is compatible with the short working distance of high magnification objective lenses. Furthermore, our innovative two-layered structure effectively traps floating adipocytes, preventing cell loss while tracking cellular responses in the designated ROIs. The volume of the chip's channel is also as small as 10μl, enabling more cost-effective experiments. Using this platform, we explored different ECM conditions and observed that a fibronectin-coated surface promoted spontaneous dedifferentiation of adipocytes, whereas

the Matrigel inhibited dedifferentiation. Furthermore, utilizing our high-resolution live imaging platform, we discovered two distinct processes of LD secretion in dedifferentiating adipocytes. The first involved remodeling of the actin cytoskeleton to rapidly expel the large central LD out of the adipocyte. The second was the exchange of LD content between neighboring adipocytes in contact with each other.

2.2 Materials and Methods

2.2.1 Animals

Adipoq-Cre [53], *Adipoq*-CreER^{T2} [54], *Pparg*$^{flox/flox}$ [55], *Rosa26*-mT/mG [56], *Lats1*$^{flox/flox}$ [57], *Lats2* $^{flox/flox}$[58], and *Rosa26*-tdTomato [59] mice were bred to generate mice with indicated allele combinations. For all experiments, 6~8-week-old male mice were used. For induction of Cre-mediated recombination in *Adipoq*-CreER^{T2} mice, 75 mg/kg tamoxifen (Cayman Chemical) dissolved in corn oil (Sigma) was administered via intraperitoneal injection at the indicated time points. Mice were housed in a specific pathogen-free facility within the KAIST Laboratory Animal Resource Center, maintained under a 12 h light-dark cycle, and given free access to food and water. All protocols for mouse experiments were approved by the Institutional Animal Care and Use Committee (IACUC) of the Korea Advanced Institute of Science and Technology.

2.2.2 Isolation of primary adipocytes

Subcutaneous (scWAT) and visceral (vWAT) fat pads were dissected and processed for mature adipocyte isolation. Briefly, mouse white adipose tissue (WAT) fat pads were dissected and minced finely with a razor blade. The minced tissue was digested in a 37℃ shaking water bath at 120 rpm with Krebs-Ringer-Henseleit (KRH) buffer (30 mM HEPES, pH 7.4, 1 mM $CaCl_2$, 120 mM NaCl, 4 mM KH_2PO_4, 1 mM $MgSO_4$, 10 mM $NaCO_3$, 200nM adenosine) containing 1.5% bovine serum albumin (BSA), 0.9 mg/ml glucose and 1 mg/ml of collagenase type 1 (Worthington) for 30 min. Collagenase digestion was followed by filtration through a 100 μm nylon mesh strainer (Falcon), and adipocytes were allowed to float for approximately 3 minutes. The floating adipocytes were transferred to a 1.5 ml Eppendorf tube using a wide-bore tip and washed 3 times with a culture medium (DMEM/F12, 10% FBS, 1% Penn/Strep) at room temperature while free-floating. For each round of washing, cells were allowed to float for 3 minutes, and the infranatant was removed with a syringe and needle. After removing the last wash, isolated adipocytes were diluted with culture medium and embedded into Matrigel or transferred to the ceiling culture chip for further experiments. For induction of Cre-mediated recombination in adipocytes isolated from *Adipoq*-CreER^{T2} mice, 1 μM 4-hydroxytamoxifen (4-OHT) was treated for the indicated time.

2.2.3 Labeling of lipid droplets for live cell imaging

Freshly isolated primary adipocytes were incubated in a culture medium including BODIPY (0.2 μg/ml) overnight to label LDs. Incubated cells were centrifuged at 100 RCF in a benchtop clinical centrifuge and then washed with fresh media several times before being transferred to the ceiling culture chip.

2.2.4 Fabrication of ceiling culture chip and cell loading

The standard soft lithography technique was used to fabricate the ceiling culture chip (Fig.2.2c). First, the two-layered SU-8 master mold was fabricated on a silicon wafer using photolithography. Both the first and second layers are 100 μm high, making the central cell culture chamber as high as 200 μm. Next, polydimethylsiloxane (Sylgard 184, 10:1) was poured with caution to avoid air bubbles and cured in the oven at 80℃ for 2 h. Next, the holes for an inlet and an outlet were punched on the cured PDMS replicas, followed by bonding of the punched PDMS block to a coverslip or a glass-bottom dish using oxygen plasma treatment. The ceiling culture chips were then placed in an 80℃ oven for firm bonding and then rinsed with 70% ethanol and tertiary distilled water. Finally, the ceiling culture chips were sterilized under UV light with a wavelength of 365 nm for 15 min.

For the fibronectin-coated condition, fibronectin was diluted in ice-cold PBS to the concentration of 100 μg/ml and loaded into the channel. The channel filled with fibronectin solution was sealed and flipped over to be placed in an incubator overnight. The channel was then rinsed 1~2 times with PBS before 2,000 mature adipocytes were loaded through the inlet in the cell culture chamber. For the Matrigel embedding condition, adipocyte suspension was first diluted in the same volume of growth factor reduced Matrigel (Corning) to be loaded in the sterilized ceiling culture chips. The chips were kept in the incubator for 40 min until the Matrigel solidified. After the cells were loaded, 3 ml of complete media was added to each glass-bottom dish.

2.2.5 Live cell imaging

The ceiling culture chips were mounted on an epifluorescence microscope (Zeiss, Axio Observer series) that was equipped with a custom-made microscope-mountable incubator system to control CO_2 levels and temperature. Images were obtained at intervals of 15 or 20 min with ZEN blue software.

2.2.6 Image processing

The images obtained with ZEN blue software were processed with ImageJ software. Briefly, the outline of cells was marked with the freehand selection tool, and the area, perimeter, position, roundness, circularity, *etc*., were calculated.

2.2.7 Shape index

In this paper, we introduced the shape index to quantify the level of dedifferentiation instead of conventional parameters such as circularity or roundness. The shape index is defined by the formula shown below.

$$\text{Shape index} = \sqrt{(Roundness)\cdot(Circularity)} = \frac{4\cdot(Area)}{(Perimeter)\cdot(MajorAxis)}$$

We defined the shape index because we empirically found that circularity and roundness did not yield adequate results in our hands. For example, the circularity was consistent with the subjective scoring of cell morphology irregularity, but it did not reproduce the same result on the same cell morphology depending on cell size or image resolution. On the other hand, roundness showed robust results, but it was not consistent with subjective scoring (Fig.2.1). Therefore, we defined a shape index that was more robust than circularity and more intuitive than roundness.

Irregularity (Subjective)	Perfectly circular	Irregular	More irregular	Extremely irregular
Circularity	0.899	0.635	0.272	0.161
Roundness	1	0.658	0.348	0.496
Shape index	0.948	0.646	0.308	0.282

Irregularity (Subjective)	Perfectly circular	Perfectly circular	Perfectly circular
Circularity	0.928	0.912	0.902
Roundness	1	1	1
Shape index	0.963	0.955	0.950

Figure 2.1 Comparison of various indices for morphological quantification.

2.2.8 Immunostaining

Cells in the ceiling culture chips were fixed with 4% paraformaldehyde for 15 min at room temperature. Fixed cells were gently washed with PBS 2 times, permeabilized with 0.2% Triton X-100 for 15 min, and blocked with 3% (w/w) bovine serum albumin. Samples were then incubated with phalloidin (Abcam) at 4℃ for 20 min and washed with PBS several times. Lastly, the chips were filled with a mounting medium (Dako) to prevent photobleaching.

2.2.9 Confocal microscopy

The confocal microscope (ZEISS, LSM780) and z-stack module of ZEN blue software were used to reconstruct the 3-D structure of cells undergoing dedifferentiation. The pinhole size was adjusted to make the diameter of the airy disc ~1μm, and the step size was set to 0.5 μm.

2.2.10 Statistical analysis

Origin software was used for statistical analysis. The two-tailed t-test with Welch correction was performed to determine significant differences between pairs of datasets, and one-way analysis of variation (ANOVA) with Fisher LSD *post hoc* analysis was used when there were more than two datasets. The significance

cutoff was 0.05 (*: $p<0.05$, **: $p<0.01$). All the I-shaped bars drawn on the data represent the mean value ± standard deviation range.

2.3 Results

2.3.1 Ceiling culture chip facilitates long-term observation of adipocytes under varying ECM conditions

Because adipocytes float and do not attach to the bottom of the cultureware, imaging them is challenging unless they are embedded in a hydrogel. However, many natural/synthetic hydrogels, including Matrigel, are likely to influence the cellular states of adipocytes. To address this concern, we developed a ceiling culture chip system. Due to the two-layer construction that confines buoyant cells within the cell culture chamber, the isolated primary adipocytes in the ceiling culture chip can be readily imaged. Furthermore, the unique chamber design allows imaging of the cells either attached to the ECM-coated ceiling or embedded within hydrogels, enabling us to explore various ECM conditions in both 2D and 3D (Fig.2.2a).

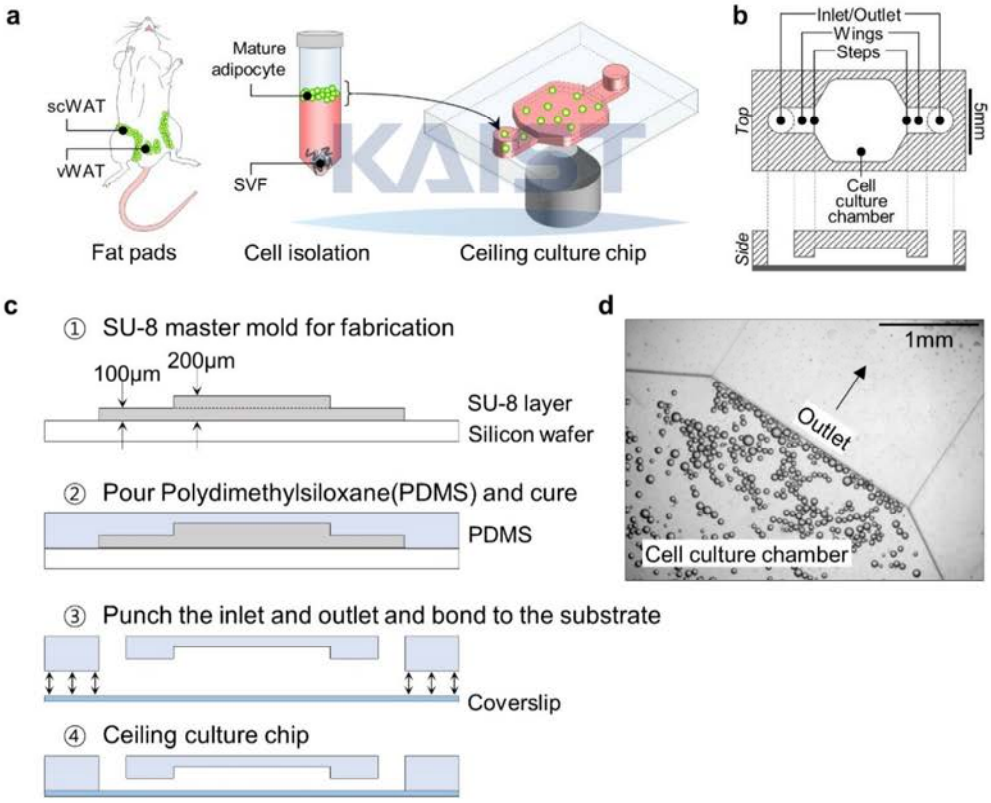

Figure 2.2 Schematic presentation of the experiment. a Mature adipocytes were isolated from scWAT and vWAT of mice and then transferred to the ceiling culture chip. **b** Detailed design of the ceiling culture chip. Not drawn to scale in the z-direction. **c** Fabrication of ceiling culture chip. **d** Image was taken immediately after loading the mature adipocyte into the channel. Cells trapped in the cell culture chamber cannot escape through the outlet.

When viewed from the top, our ceiling culture chip is symmetrical with a cell culture chamber in the middle having an inlet and outlet holes on each end of the chamber, connected by the wings. The ceiling culture

chip was fabricated using a two-layered master mold, thereby featuring a step between the wing and the cell culture chamber. The height of the cell culture chamber is 100 μm higher than its two wings (Fig.2.2b, c). The step feature on the chamber ceiling keeps adipocytes from escaping through the outlet once loaded in the chamber (Fig.2.2d).

Also, since the microscale chip was completely filled with culture media, there was no flow within the chamber. Thus, mature adipocytes with low binding affinity to the substrate remain stationary throughout long-term culture even under the continuous motion of the microscope stage or during the medium change. Furthermore, because the ceiling is only 200μm high from the bottom of the chamber, the platform could fit within the short working distances of the high magnification imaging system.

2.3.2 Fibronectin promotes adipocyte dedifferentiation while Matrigel inhibits it

The ECM microenvironment significantly impacts adipocyte differentiation and plasticity [60]. For example, previous studies have reported that about 60% of SVF from the breast of 25~45-year-old women completed adipogenesis on Matrigel-coated substrate, whereas only 40% and 20% of SVF differentiated on fibronectin-coated or non-coated plastic surfaces [61]. Therefore, based on the effect of ECM type on adipogenesis, we hypothesized that ECM type might also influence the reverse process, adipocyte dedifferentiation.

To verify this, we first generated a transgenic mouse model by crossing mice with a Cre transgene under control of the adiponectin promoter (*Adipoq*-Cre) with mice carrying the membrane-targeted tdTomato/membrane-targeted EGFP (*Rosa26*-mT/mG or mT/mG) Cre reporter allele, which expresses EGFP in adipocytes and tdTomato in others, allowing permanent and subsequent tracing of adipocytes (Fig.2.3a). Using this mouse model (hereafter, referred to as *Adipoq*-Cre; mT/mG), we isolated mature adipocytes from subcutaneous adipose tissue (scWAT) and visceral adipose tissue (vWAT) and cultured them in three different ECM conditions: untreated PDMS (P) as a control, Matrigel-coated (M), and Fibronectin-coated (F). The adipocytes in the chamber were imaged once every two days. Since adipocytes undergo a morphological change from a perfectly spherical shape (Fig.2.2d) into irregular shapes as dedifferentiation progresses, we employed the shape index as a metric to assess the degree of dedifferentiation. The shape index shown below ranges from 0 to 1, where an index value of 1 indicates a perfect circle. As the shape becomes irregular, the shape index approaches 0 (Fig.2.3b).

In the case of mature adipocytes isolated from scWAT, the shape indices of all cells under conditions P, F, and M are approximately 1 on Day 1, which means that the cells are mostly circular in shape. On Day 3, all the groups have dedifferentiated when compared to the ones on Day 1, evidenced by the changes in the shape indices. Though there was no significant difference between the shape indices of cells under the conditions P and M, the cells under condition F showed significantly lower values of shape indices. On Day 5, the cells seeded on the untreated PDMS chip exhibited a similar distribution of shape indices to that

of cells under condition F on Day 3. For condition F, the shape indices of the cells on Day 5 became considerably smaller than those on Day 3, and their distribution was also significantly narrowed. On the other hand, the cells for condition M did not dedifferentiate further compared to Day 3. None of the three conditions made cells further dedifferentiate between Days 5 and 7. Collectively, mature adipocytes under condition F dedifferentiated the fastest. However, condition P also induced the cells to dedifferentiate to a similar degree, only taking longer than condition F. Adipocytes embedded in the Matrigel were resistant to dedifferentiation, retaining LDs with high shape indices (Fig.2.3c, d).

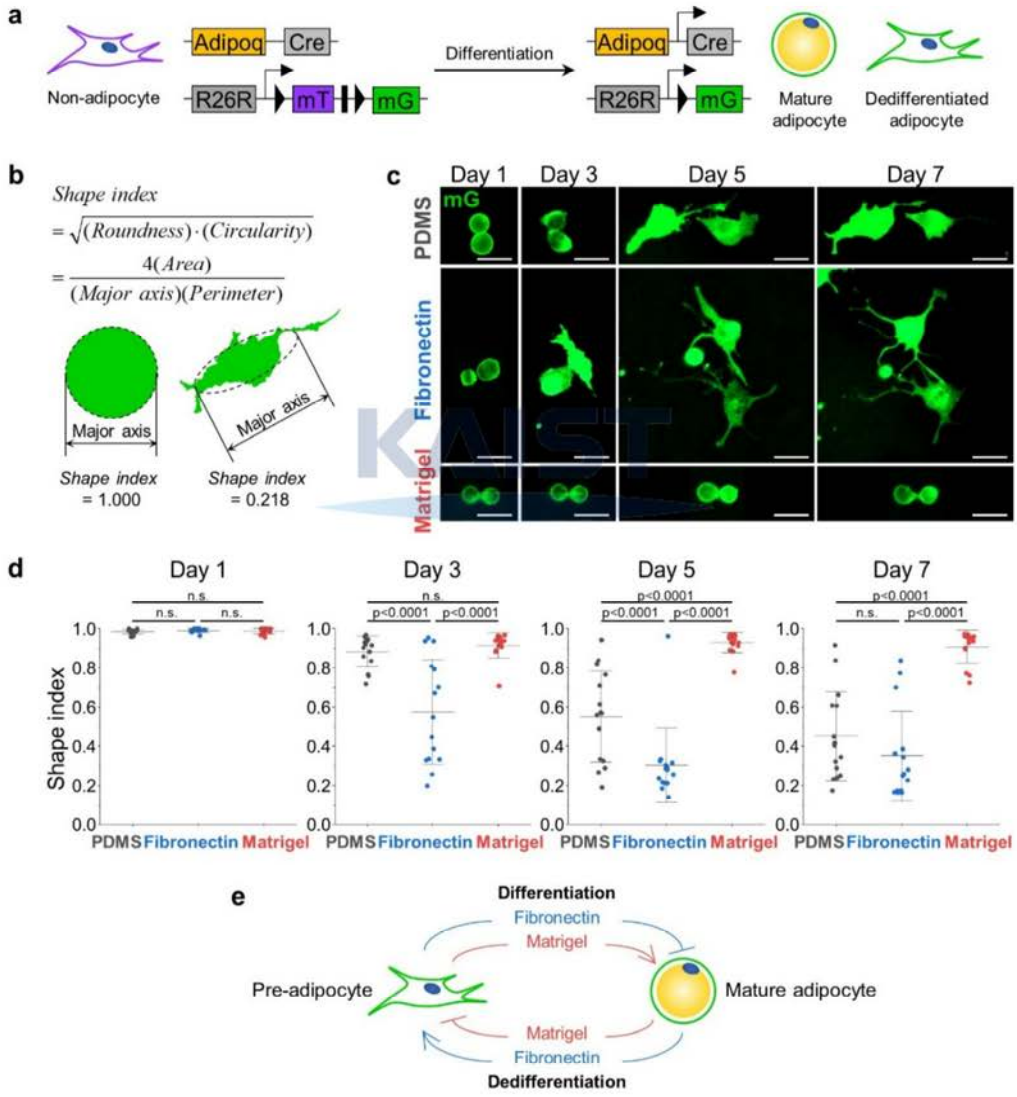

Figure 2.3 The change in shape index is ECM-dependent. The fibronectin condition promoted the dedifferentiation while the Matrigel condition inhibited it. a Schematic diagram for specific labeling and tracing of adipocytes using *Adipoq*-Cre; *mT/mG* mice. **b** Example of shape index used to quantify the degree to which adipocytes are dedifferentiated. Mature adipocytes have shape indices of 1. **c** Representative images of primary adipocytes cells undergoing dedifferentiation at each condition on day 3, 5, and 7. (P: Adipocytes were embedded in untreated PDMS chamber, F: Adipocytes were seeded in PDMS chip coated with 100 μg/ml fibronectin, M: Adipocytes were embedded in 50% Matrigel medium). **d** Shape index distributions of scWAT adipocytes over time. I-shaped bars represent mean ± s.d. n=15 each. p-value from one-way ANOVA with Fisher's LSD *post hoc* test. t-value from two-tailed t-test v.s.

Day n-2 data of the same group. **e** Schematic representation of promoting/inhibiting effect of ECM type on adipocyte differentiation and dedifferentiation.

Adipocytes isolated from vWAT exhibited similar changes in shape indices with those isolated from the scWAT (Fig.2.4). These results suggest that ECM conditions that restrict or promote adipogenesis have an opposite effect on adipocyte dedifferentiation. Notably, the findings establish a set of culture conditions that are either permissive or non-permissive to adipocyte dedifferentiation, as defined by ECM conditions. This result can also be explained by the fact that collagen VI and laminin are the common major components of *in vivo* adipose tissue and Matrigel [62], suggesting that the physiologically relevant 3D soft microenvironment constructed by Matrigel may contribute to the maintenance of adipocyte integrity, hindering the dedifferentiation process. As summarized in Fig.2.3e, we found that the ECM condition that inhibits adipocyte differentiation, specifically fibronectin, promoted adipocyte dedifferentiation.

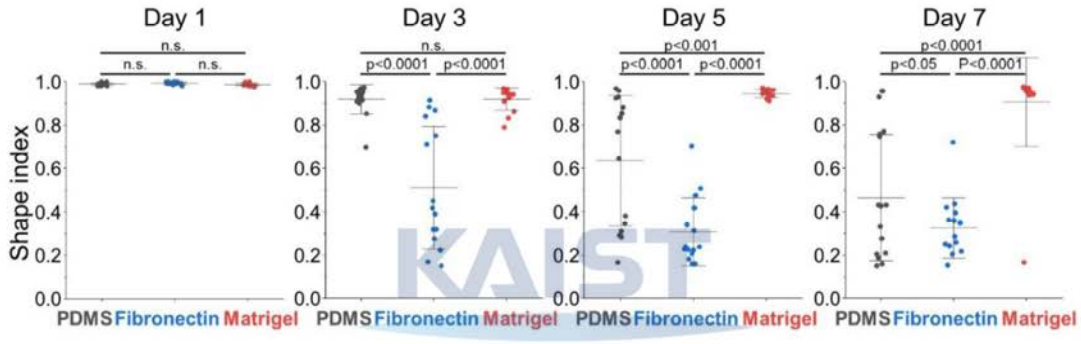

Figure 2.4 Shape index distributions of vWAT adipocytes over time. I-shaped bars represent mean ± s.d. n=15 each. p-value from one-way ANOVA with Fisher's LSD post hoc test. t-value from two-tailed t-test v.s. Day n-2 data of the same group.

2.3.3 Suppression of Hippo or activation of Hedgehog signaling pathways induce adipocyte dedifferentiation

Here, we investigated whether the concept illustrated in Fig.2.3e could also be applied to signaling pathways that regulate adipogenesis. In particular, the Hippo signaling pathway has been identified as a key regulator that promotes adipogenesis [63, 64], whereas the Hedgehog signaling pathway inhibits adipogenesis [65].

Thus, we sought to evaluate whether the suppression of the Hippo or activation of the Hedgehog signaling pathway would promote adipocyte dedifferentiation. To this end, we isolated mature adipocytes from the scWAT of *Adipoq*-Cre; mT/mG mice and treated them with XMU-MP1, a Hippo signaling inhibitor, or SAG21k, a Hedgehog signaling activator (Fig.2.5a). Based on our findings in the preceding section, we chose Matrigel as the ECM material to eliminate the influence of ECM-induced dedifferentiation. Indeed, both XMU-MP1 and SAG21k treatment potently induced adipocyte dedifferentiation even under Matrigel

culture conditions which were non-permissive for dedifferentiation in vehicle-treated control adipocytes (Fig.2.5b, c).

2.3.4 Deletion of PPARγ in mature adipocytes induces dedifferentiation

Peroxisome proliferator-activated receptor γ (PPARγ) is well-known as the master regulator of adipocyte differentiation and function [66-69]. Therefore, we speculated that deletion of PPARγ would also promote the dedifferentiation of adipocytes. To test this notion, we established a mouse model in which both deletion of PPARγ and fluorescent labeling of mature adipocytes could be simultaneously induced by tamoxifen administration. This model was developed by crossing three different transgenic mice (*Adipoq*-CreER^{T2}; *Pparg*$^{flox/flox}$; mT/mG, herein, *Pparg* iAKO) (Fig.2.5d). Following tamoxifen administration to *Pparg* iAKO mice, primary adipocytes from scWAT were isolated and embedded in Matrigel (Fig.2.5e). As anticipated, PPARγ-deleted adipocytes labeled with EGFP displayed numerous small LDs and enlarged, irregular cytoplasmic regions (Fig.2.5f, g), which are a characteristic feature of dedifferentiated adipocytes [47]. Altogether, these observations highlight the crucial roles of Hippo/Hedgehog signaling pathways and PPARγ in maintaining mature adipocyte identity in addition to their roles during adipogenesis. This result also emphasizes how the direct activation or suppression of downstream regulators can override Matrigel's effect in inhibiting adipocyte dedifferentiation.

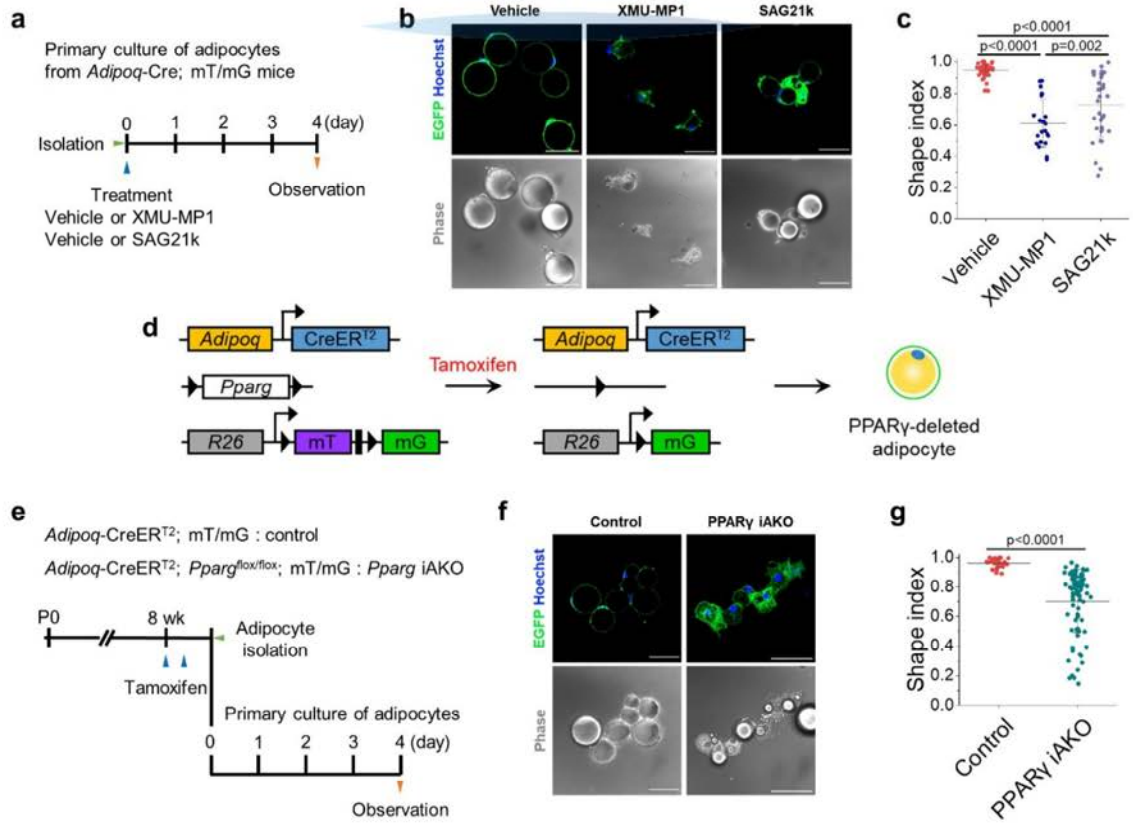

Figure 2.5 Inhibitors of adipogenesis and deletion of PPARγ are molecular cues that induce adipocyte dedifferentiation. a Experimental scheme for isolating primary adipocytes from *Adipoq*-Cre; mT/mG mice and their analysis 4 days after culture **b** Confocal images of adipocytes isolated from *Adipoq*-Cre; mT/mG mice and treated with 10 μM XMU-MP1 or 1 μM SAG21k for 4 days. Vehicle (DMSO) is used as a control. **d** Experimental scheme for isolation of primary adipocytes from control (*Adipoq*-CreER^{T2}; mT/mG) or *Pparg* iAKO mice after tamoxifen administration and their analysis 4 days after culture. e Confocal images of adipocytes isolated from control or *Pparg* iAKO mice 4 days after culture. Nuclei are stained with Hoechst (blue). Scale bar, 50 μm.

2.3.5 Dynamic cellular deformations accompany LD secretion during adipocyte dedifferentiation

Next, we took advantage of our ceiling culture chip to perform time-lapse imaging with high-spatiotemporal resolution while adipocytes were undergoing adipocyte dedifferentiation. Here, we used adipocytes derived from mT/mG mice without the Adiponectin-Cre transgene, such that all cells express a membrane-targeted tdTomato signal. Adipocytes were then labeled with BODIPY FL to allow the simultaneous analysis of LD dynamics. In the early stage of the dedifferentiation, adipocytes featured a large LD and several tiny LDs around the large one. Interestingly, some cells exhibited protrusive motion with well-developed pseudopodia (Supplementary Video 2.1), which is atypical behavior for fully differentiated adipocytes. In mature adipocytes that come into contact with the ceiling, the large central LD, which was initially spherical in shape, flattened to conform to the ceiling surface, generating many pseudopodia. (Fig.2.6a, 1st column). The temporal changes in the aspect ratio of lipid droplets shown in Fig.2.6b implied that these LDs were likely subject to intracellular compressive stress (Fig.2.6a, 2nd~3rd column). The vibrational motion is shown in Fig.2.7a in detail. As soon as it is extruded out of the cell, the LD restored its initial spherical shape, as shown in Fig.2.6a, 4th column, and Fig.2.6b, suggesting the immediate release of compressive stress upon extrusion. Prior to extrusion, the LDs exhibited vigorous vibrations, quantified as the periodic fluctuations in the angle θ between the x-axis and the major axis of the LD (Supplementary Video 2.2, Fig. 2.6b). As the aspect ratio becomes 1, neither the major axis nor the angle θ could be defined further (Fig.2.6b, c). Some cells even displayed a rope-like structure, shown as a crescent-shape band, squeezing the LD to suddenly extrude it from the cell (Fig.2.7b, Supplementary Video 2.3). This structure appeared to be reminiscent of the contractile ring typically appearing during the telophase of the cell division. Subsequently, the rim through which the LD exited gradually shrank to finally close like a purse-string, completely isolating the extruded droplet from the parental body (Fig.2.6a, 5th~9th column). The black dotted line in the last row of Fig.2.6 indicates the contracting rim structure, which was traced in the phase image by following the interface of the extruded LD in contact with the ceiling. After the rim structure was closed, the extruded LD departed from the cell body and was still wrapped by the plasma membrane, evidenced by the purple tdTomato signal (Fig.2.6a, 10th~14th column).

We analyzed liposecretion events between 24 and 144 hours after the mature adipocytes were seeded in the fibronectin-coated chip. Based on the common characteristics of the liposecretion, different modes of liposecretion can be categorized as follows (Fig.2.7): (1) Secretion involving mechanical vibration (Fig.2.6, Fig.2.7a), (2) secretion involving crescent-shaped band structure (Fig.2.7b, Supplementary Video 2.3), and (3) secretion involving sudden cellular elongation (Fig.2.7c). Regardless of the mode of liposecretion, lipid

extrusion seems to be made possible by intracellular mechanical contractility. Interestingly, it seems that there are correlations between the liposecretion modes and the extent of cellular deformation where the specific radius r^* refers to the ratio of r (radius of lipid droplet after the lipo secretion) over c (smallest radius of the lipid droplet before the liposecretion) and the curvature κ refer to the minimal curvature of the lipid droplet (Fig. 2.7d). This can be explained by the analogy between adipocytes and double emulsion where the cell is the sheath fluid and the lipid droplet is the core fluid. Then the cells with small curvatures would have small capillary pressure, making it easier for that of the lipid droplet to overcome.

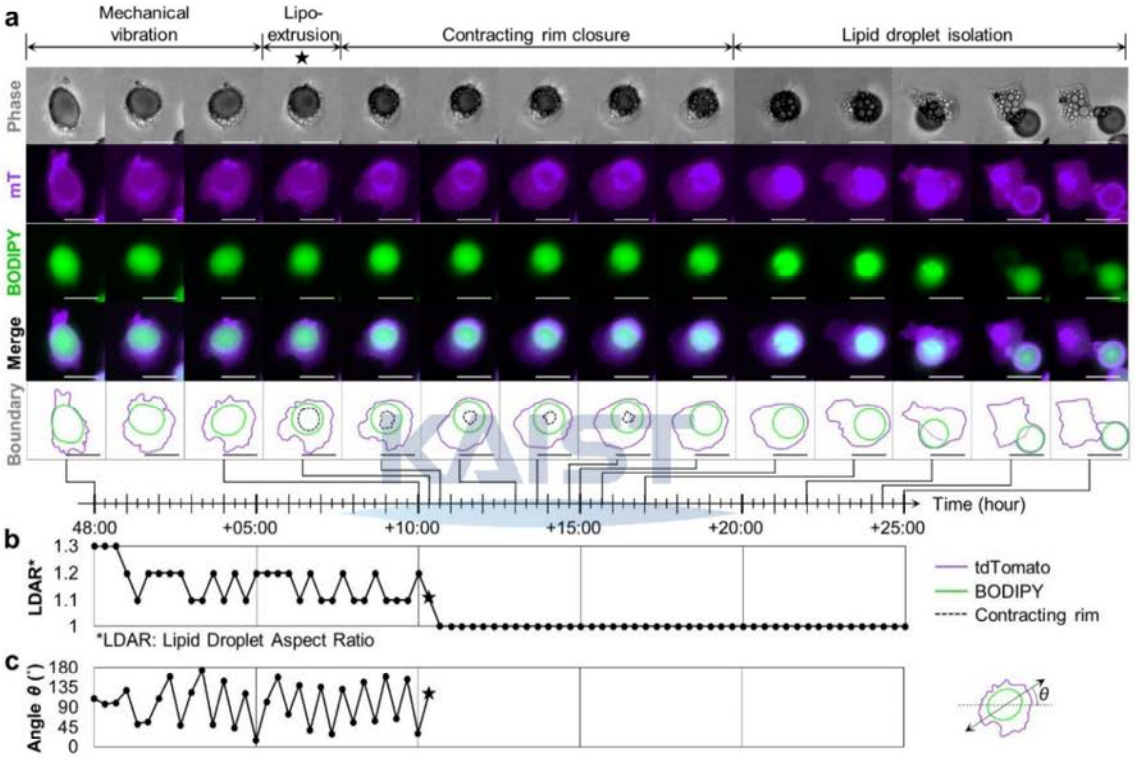

Figure 2.6 LD secretion accompanies dynamic deformation of LD. a Time-lapse image shows the entire process of LD secretion where the LD encapsulated in the dedifferentiating cell escapes from the cell body. The shape of the LD, which was initially flattened and trembling, suddenly restored its original spherical morphology. In phase images, a rim-like structure seemed to contract and then closed completely. After the closure, the LD could move freely. The secreted LD seemed to be still enclosed in the cell membrane (scale bar = 100μm, relative time). **b** The abrupt change in the aspect ratio of an LD upon LD extrusion at +10:20 hr (marked by a star) indicates immediate release of compressive stress. **c** The angle θ between the x-axis and the major axis of the LD displays regular fluctuations.

Fully differentiated mature adipocytes do not proliferate. However, a number of reports have suggested that adipocytes regain proliferative capability during the dedifferentiation process[43, 47]. Similarly, our EGFP$^+$ *Adipoq*-Cre; mT/mG adipocytes undergoing the LD secretion process were shown to proliferate, passing down the LDs to the daughter cells during cell division (Supplementary Video 2.4).

2.3.6 Dynamic actin remodeling mediates LD secretion in dedifferentiating adipocytes

As is the case for many dynamic cellular processes, the whole LD secretion process that features oscillation and extrusion likely involves intracellular actin-mediated force generation. To determine how the F-actin structures of mature adipocytes are remodeled to extrude the largest organelle, i.e., the central LD of a unilocular adipocyte, out of the cell, we examined the structural organization of F-actin. First, wild-type adipocytes undergoing dedifferentiation were fixed and stained in the ceiling culture chip. Then, we arranged the images of fixed cells along a virtual time axis based on the extent to which the LDs had emerged from the cell. This arrangement allowed us to estimate the dynamic remodeling of the actin structures at each designated step of LD secretion (Fig.2.6). Here, we divided the LD secretion phenomenon into three phases: the pre-secretion, secretion, and post-secretion phases. Each phase was again divided into two sub-phases (Fig.2.8a).

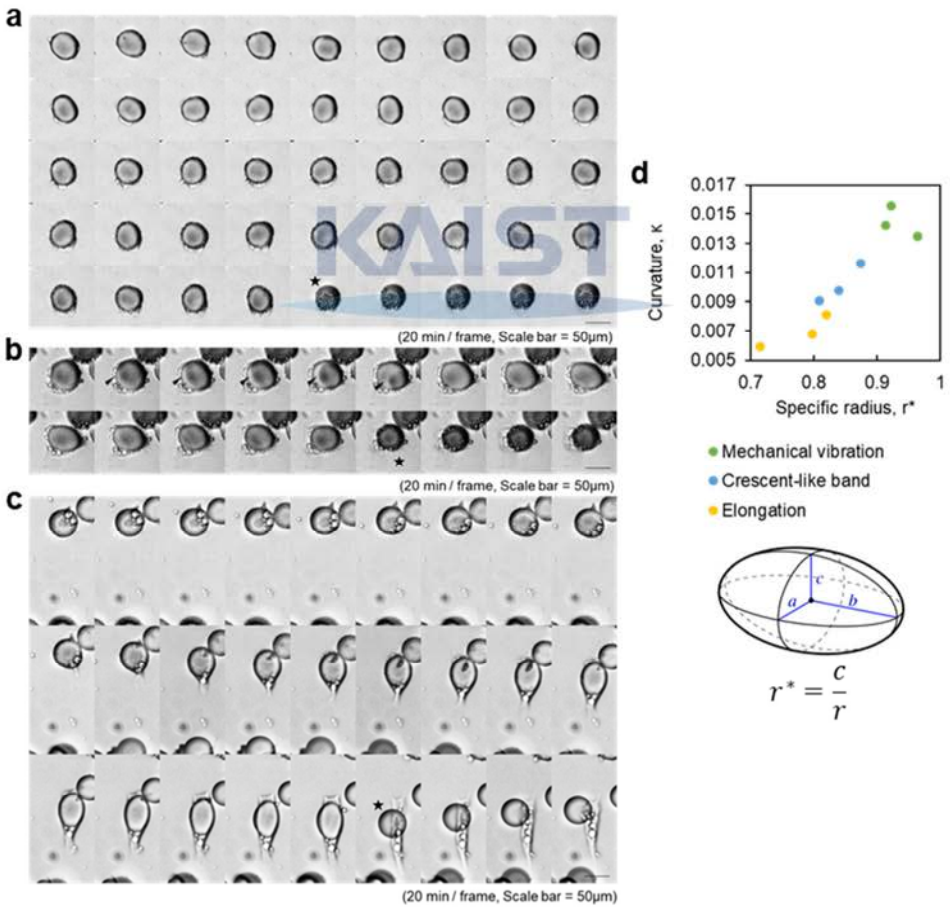

Figure 2.7 Liposecretion events can be categorized into three different modes. a Secretion involving mechanical vibration: The lipid droplet vibrates vigorously before the secretion. **b** Secretion involving crescent-shaped band structure: A rope-like structure, shown as a crescent-shaped band, appears and squeezes the LD to suddenly extrude it from the cell (Supplementary Video 2.3). Band structure is indicated by solid arrowheads. **c** Secretion involving sudden cellular elongation: Lipid droplets get extruded soon after the sudden elongation of the cell. **d** Cells have different secretion mode of liposecretion depending on the cellular curvature.

At the pre-secretion phase, cells formed pseudopodia on the ceiling. The cells at the first sub-phase featured flattened LDs with actin filaments distributed everywhere except the inside of the LD, what we called an actin shell (Fig2.8a, b). Occasionally, the actin shell developed holes of varying sizes along the surface of the LDs (Fig.2.8a, c).

At the beginning of the main secretion phase, the small actin rims merged into one or two larger ones (Fig.2.8a, d). The large holes in the actin shell were also observed by the orthogonal views of 3D-reconstructed F-actin images obtained with confocal microscopy (Fig.2.8h). Despite the presence of the holes, some cells still contained the LDs deformed by the actin band. Based on the morphological clues from Fig.2.6, the subsequent process would be the extrusion of LDs through the opening, now identified as the rim structure made of actin. The deformed LDs in Fig.2.8d were consistent with what was shown in the trembling cells shown in Fig.2.6, Supplementary Video 2.2. Therefore, we hypothesize that the vibrational movements of LDs were caused by the interactive forces between the contracting actin band and the resistance of the plasma membrane. Following the extrusion, three-dimensional actin bands rolled up to condense onto a ring structure on the ceiling (Fig.2.8a, e).

After being pushed out, the LD eventually departed from the site of exit, leaving behind a hollow actin ring structure (Fig.2.8a, f). Those voids, the consequences of LD secretion, are unique signatures of dedifferentiated adipocytes that are not present in normal fibroblasts. Cells that have secreted most LDs finally began to develop stress fibers, placing themselves in a different state (Fig.2.8a, g). In summary, we identified the existence and the role of rearranging actin structures during rapid LD secretion by mapping the snapshots of stained cells in selected essential phases on the virtual time axis of real-time images.

2.3.7 Inhibition of non-muscle myosin suppresses adipocyte dedifferentiation

Actomyosin structures are critical in various intra- and inter-cellular activities that require mechanical forces, including cell division, migration, tissue morphogenesis, and muscle contraction. Actomyosin bundles can generate force through the sliding motion between actin filament and myosin units, represented by the closure of the contractile ring in cytokinesis and the rear contraction of a migrating cell. Based on the observations that cells displayed mechanical vibrations and that the actin structures were remodeled during the LD secretion process, we hypothesized that the LD secretion is induced by the contractility of non-sarcomeric actomyosin. To investigate the involvement of myosin in the squeezing motion during the extrusion process, blebbistatin treatment was used to specifically inhibit the ATPase activity of myosin II. Mature adipocytes derived from scWAT of *Rosa26*-mT/mG mice were isolated and loaded in a fibronectin-coated ceiling culture chip. The control group was treated with BODIPY FL, and the blebbistatin treated group was treated with BODIPY FL and 50 μM blebbistatin. Over 5 days, the cells of the control group underwent dedifferentiation, featuring prominent pseudopods and active migration, while some of them completed LD secretion (Fig.2.9a, cell **α**, **β**). However, those of the blebbistatin-treated group failed to

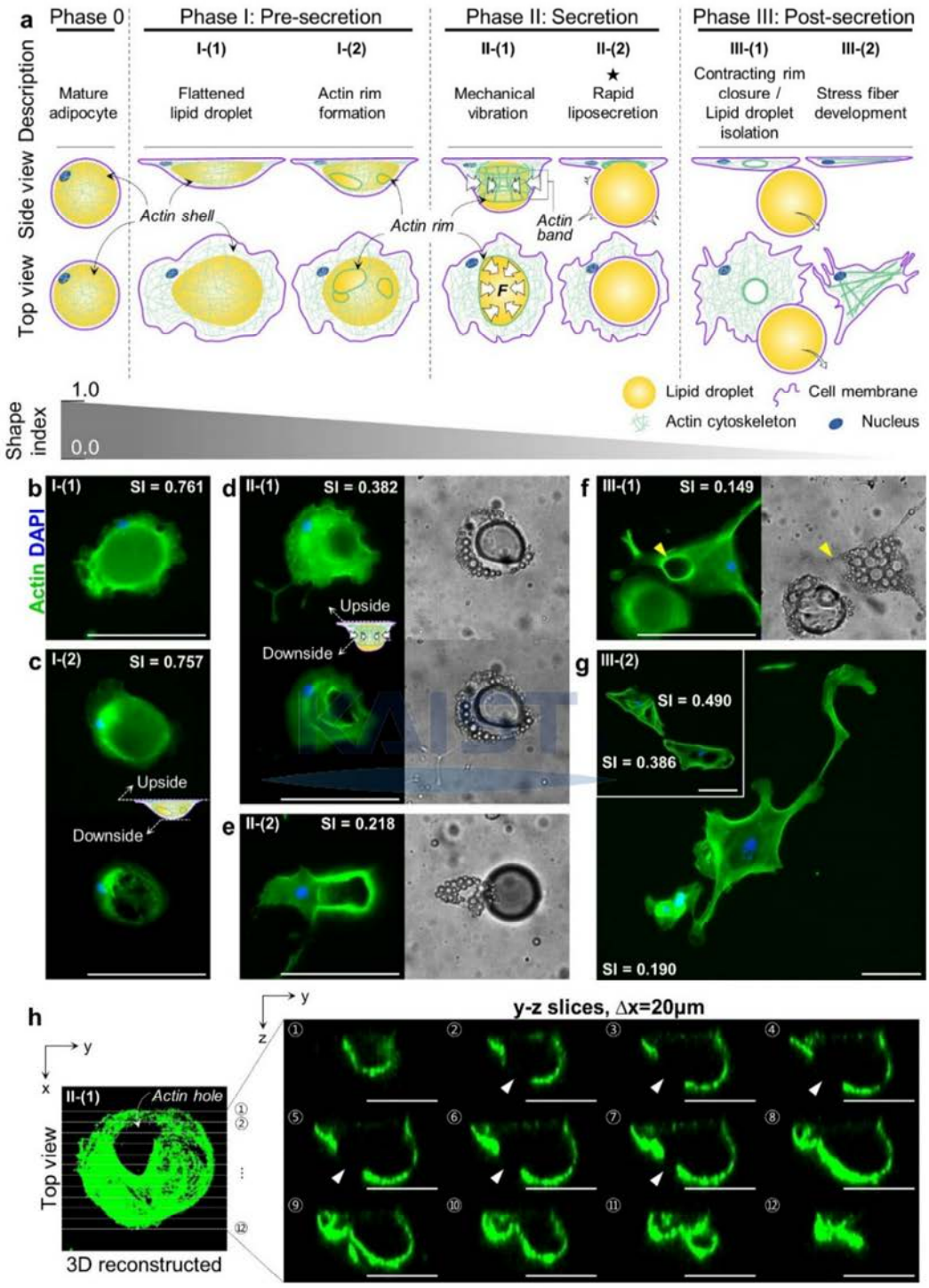

Figure 2.8 Rapid LD secretion is accompanied by dynamic actin cytoskeleton remodeling. a Schematic representation showing each phase of rapid LD secretion. **b** Actin structure of representative cell at phase I-(1). **c** Cell at phase I-(2) having actin holes at the downside. **d** Cell at phase II-(1) showing actin band that is squeezing the LD. **e** The large LD squeezed out of the main cell body restores its original spherical shape. The actin band is rolled into a thick ring-like structure. **f** The actin band remains where the LD has gone (yellow arrowhead). **g** LDs are completely secreted. (subset) Stress fibers are developed after LD secretion. Holes in the actin mesh still exist. **h** Orthogonal y-z slices of the cell at phase II-(2). A large hole in the actin shell is clearly observed at the top view (white arrow) and the orthogonal slices (white arrowheads) (scale bar = 100μm).

secrete LDs and exhibited negligible movements or deformations (Fig.2.9b). While there were no differences between the shape indices of the two groups on Day 1, the blebbistatin-treated group showed significantly higher shape index values than the control group on Day 5 (Fig.2.9c), implying that the dedifferentiation was suppressed by inhibition of myosin II. These results indicate that LD secretion and dedifferentiation are mediated by actomyosin-dependent contractility.

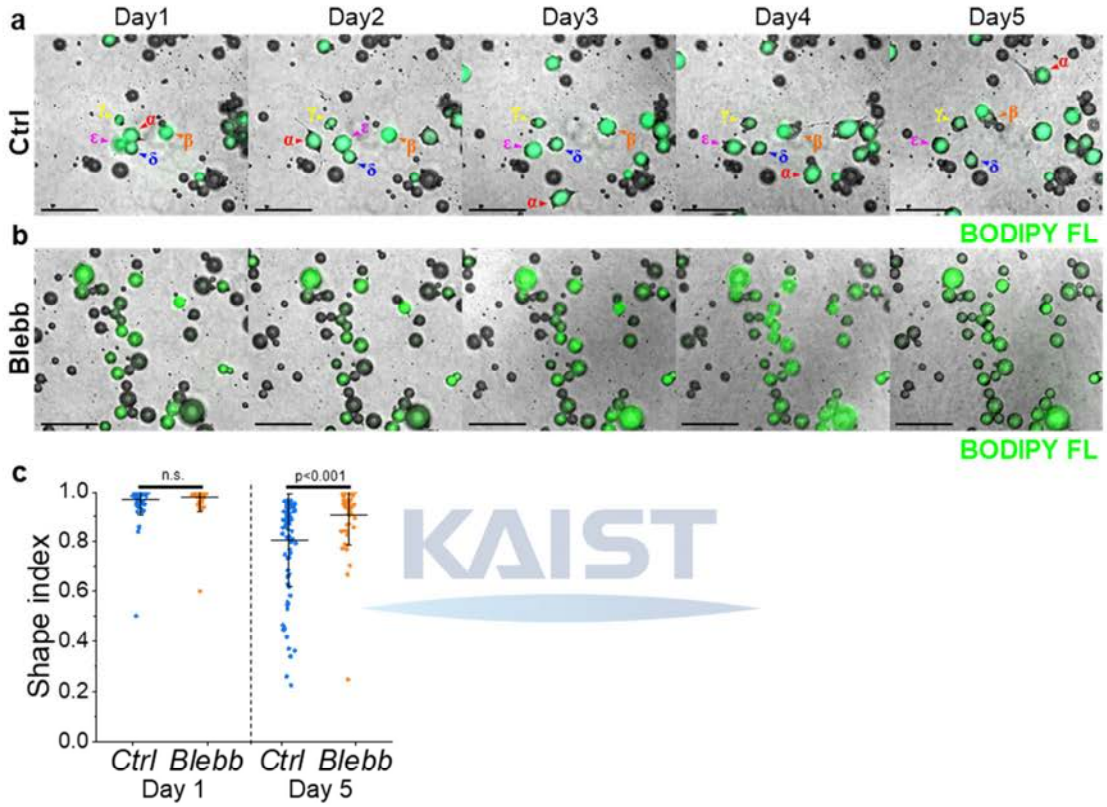

Figure 2.9 Blebbistatin suppresses LD secretion. a Representative image of dedifferentiation of the control group. Cells undergoing dedifferentiation moved around dynamically (scale bar = 200μm). **b** Representative images of 50μM lebbistatin treatment group. Cells are in a motionless state compared to the control group (scale bar = 200μm). **c** Shape indices of control group and blebbistatin treatment group. On day 5, the shape indices of the blebbistatin treatment group are significantly higher than those of the control group. t-value from two-tailed t-test. n=76, 50, 87, and 54 for Ctrl Day 1, Blebb Day 1, Ctrl Day 5, and Blebb Day 5 respectively.

2.3.8 Lipid droplet contents can be transported to adjacent adipocytes

Most dedifferentiating cells discharged their LD contents via the dynamic actin cytoskeleton remodeling processes (Fig.2.8). However, a few cells were spotted to inject their LD contents directly into their neighboring cells, evidenced by the size change of the cells in contact with others. As the diameter of the donor cell decreased, that of the receiver cell increased, supporting the transfer of LD droplet content. Cells participating in this transfer process were usually round in shape, indicating that only minimal dedifferentiation had occurred. Once the donor cells passed over their LD to the receiver cells, they either departed or shrunk on the spot (Fig.2.10a, b, Supplementary Video 2.5).

To confirm that the observed phenomenon was the LD transfer between two adjacent cells, not the simultaneous lipogenesis and lipolysis in two neighboring cells, we co-cultured WT mice cells and mT/mG mice cells, with only the LD contents of WT mice cells stained with BODIPY prior to the co-culture. In this setup, the mT/mG mice cells expressed membrane-targeted tdTomato signal, and WT mice cells expressed BODIPY FL signal on their LDs (Fig.2.10c). Over time, it was observed that the WT donor cells appeared to inject some of their BODIPY^{+} LD content into mT/mG receiver cells, making the LD of the receiver mT/mG cell fluoresce green (Fig.2.10d, e, Supplementary Video 2.6).

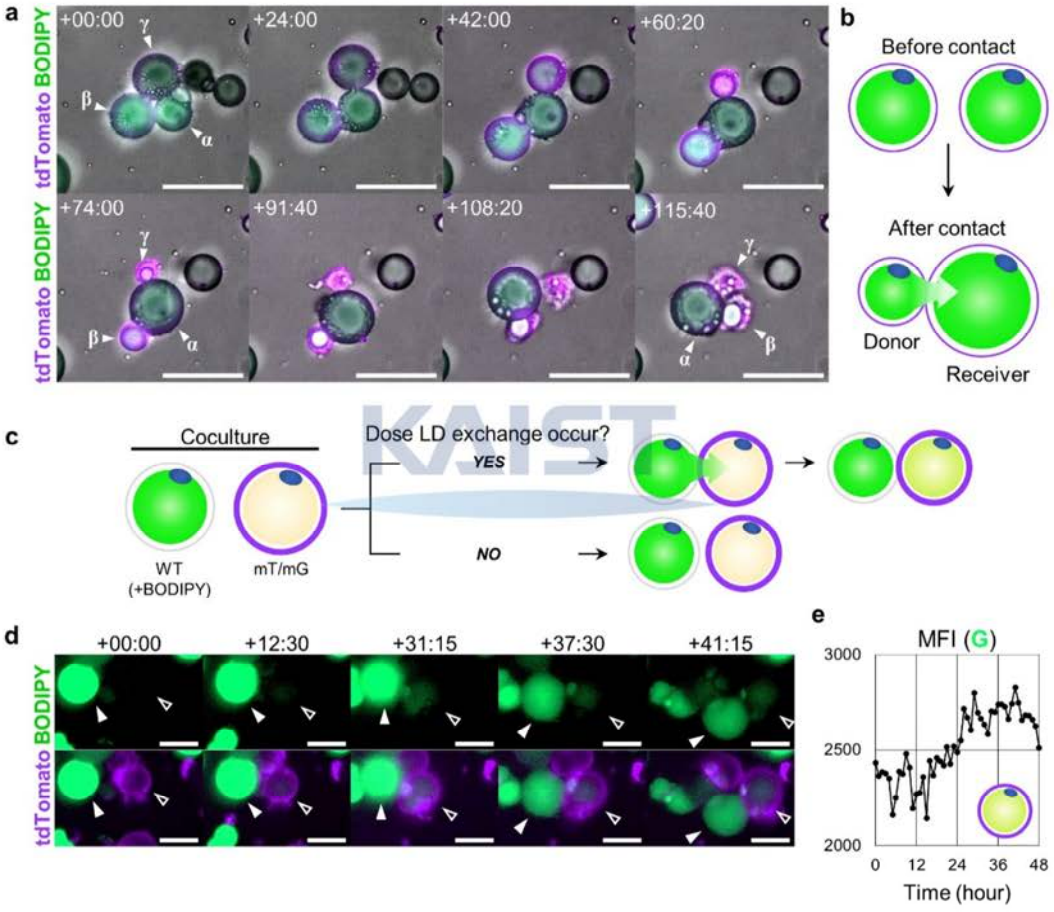

Figure 2.10 LD secretion by intercellular LD injection. a Time-lapse image showing the LD injection phenomenon (Scale bar = 100 μm). Cells **β** and **γ** transfer their LD to cell **α**. **b** Schematic representation of LD injection between two different cells. **c** Schematic representation of experimental setting. WT cells with LDs dyed with BODIPY and mT/mG cells were co-cultured in the ceiling culture chip. **d** The LD in the mT/mG cell did not express GFP at first, but over time, it gradually expressed GFP. This is evidence that mT/mG cells (empty arrowhead, acceptor) have received the BODIPY labeled LDs from neighboring WT BODIPY+ cells (filled arrowhead, donor) (Scale bar = 50 μm, Relative time from 1d:4h:30m).

2.3.9 Neighboring adipocytes exchanges their lipid droplet contents

As previously shown in Fig.2.5b and c, pharmacological suppression of the Hippo pathway by XMU-MP1 induced adipocyte dedifferentiation. To further investigate the Hippo pathway function in maintaining the mature adipocyte state, we genetically blocked the Hippo pathway in adipocytes by creating *Adipoq-*

CreER^{T2}; *Lats1/2*$^{flox/flox}$; tdTomato mice (referred to as *Lats1/2* iAKO) (Fig.2.11a), with *Adipoq*-CreER^{T2}; tdTomato mice as control. Adipocytes from both *Lats1/2* iAKO and control mice were loaded to the non-coated ceiling culture chip and treated with 2 μM of 4-hydroxytamoxifen to induce Cre recombination (Fig. 2.11b). On day 5, the shape indices of *Lats1/2* iAKO cells were significantly lower than that of control cells (Fig.2.12).

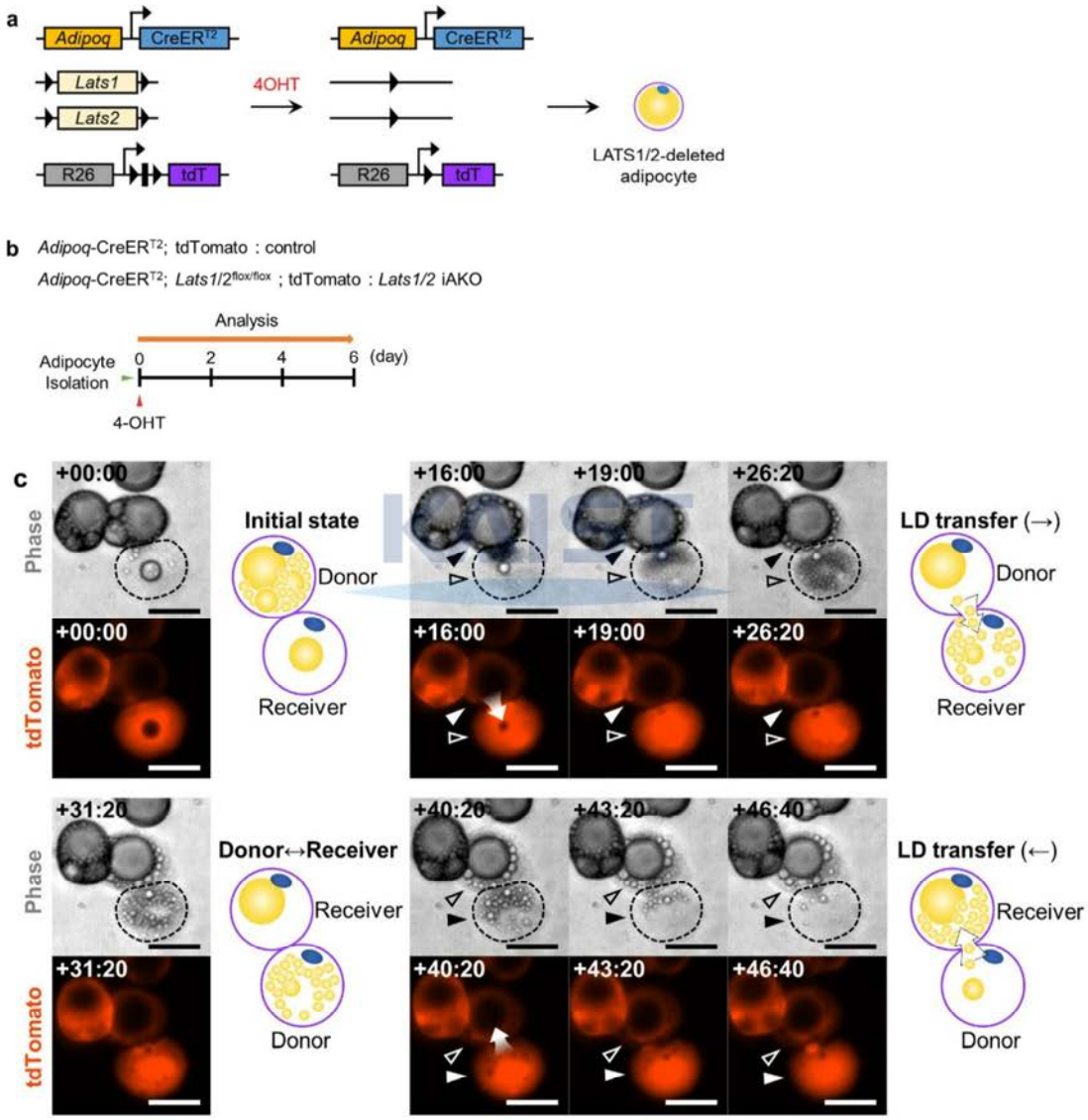

Figure 2.11 Adipocyte-specific suppression of the Hippo pathway induces a unique mode of LD secretion into adjacent adipocytes. a Schematic diagram for 4-hydroxytamoxifen (4OHT)-inducible *Lats1/2* knockout and labeling primary adipocytes from *Lats1/2* iAKO (*Adipoq*-CreER^{T2}; *Lats1/2*$^{flox/flox}$; tdTomato) mice. **b** Experimental scheme for adipocyte isolation and deletion of LATS1/2 in adipocytes from control (*Adipoq*-CreER^{T2}; tdTomato) or *Lats1/2* iAKO mice and their analysis for 6 days. **c** Time-lapse imaging of intercellular lipid exchange between adipocytes isolated from *Lats1/2* iAKO mice. Relative time from 4d:18h:45m. Scale bar, 50μm.

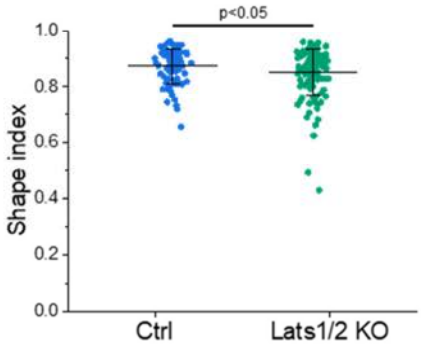

Figure 2.12 Shape index distributions of control mT/mG mice adipocytes and *Lats1/2* iAKO mice adipocytes at Day 5. t-value from two-tailed t-test. n=82 and 124 for Ctrl and *Lats1/2* KO respectively.

Using this *Lats1/2* iAKO model, we report another novel cellular activity revealed by the use of our ceiling culture chip, which is the intercellular LD exchange in granular form (Fig.2.11c). This is distinct from the LD content injection shown in Fig.2.10, where the LD contents were simply injected into the neighboring cell in a unidirectional manner. In the intercellular lipid exchange, LD contents were delivered in several small vesicles. This type of LD transfer was bi-directional and occurred while maintaining their sizes (Supplementary Video 2.7). The mechanism governing such bi-directional LD transfer between two neighboring adipocytes is an intriguing subject that merits further investigation.

2.4 Discussion

Obesity and related metabolic diseases continue to increase, demanding further efforts to better understand adipocyte biology and pathology. In particular, to gain more complete knowledge of the regulatory mechanisms of adipocytes, it is important to study not only adipogenic differentiation but also the dedifferentiation of mature adipocytes. One reason the latter has been understudied is due to the inherent characteristics of mature adipocytes as buoyant and fragile, making it difficult to culture and observe them *in vitro*. As a workaround, many studies begin with preadipocytes that will be differentiated into adipocytes *in vitro* rather than with primary mature adipocytes since the induced adipocytes are adherent, making them easier to handle. However, those induced cells display relatively large cytoplasm with multiple droplets, not sharing key characteristics with the primary adipocytes [49]. To address these challenges, our novel ceiling culture chip provides a platform for easy trapping of buoyant primary adipocytes for better imaging.

Furthermore, cultured adipocytes that have undergone dedifferentiation are indistinguishable from remnant stromal cell types after primary adipocyte isolation. Thus, the impurity of stromal fibroblasts can be misinterpreted as dedifferentiated adipocytes. In this regard, the origin of the fibroblast-like cells has always been of question. The use of the *Adipoq*-Cre; mT/mG system, however, successfully resolved the issue by differentially labeling dedifferentiated adipocytes and stromal fibroblasts.

Equipped with the ceiling culture chip and *Adipoq*-Cre; mT/mG system, we established specific conditions that either promoted or inhibited adipocyte dedifferentiation. Based on well-documented studies of adipogenesis, a condition that would inhibit adipogenesis was hypothesized to promote adipocyte dedifferentiation and *vice versa*. We then validated our hypothesis using four specific conditions known to suppress differentiation from progenitor cell to mature adipocyte (use of fibronectin, suppression of Hippo or activation of Hedgehog signaling pathway, and the deletion of PPARγ) also promoted dedifferentiation.

Furthermore, by taking full advantage of the ceiling culture chip for high-resolution live imaging of adipocyte dedifferentiation, we uncover novel aspects of the LD secretion process. Based on real-time observation, images of fixed and immuno-stained cells could be sorted in order according to the extent of LD secretion. Here, actin cytoskeletal structures were shown to be dynamically remodeled, featuring the development of holes in the actin shell functioning as an exit for LDs. To the best of our knowledge, this study is the first report of such holes produced as a result of actin remodeling.

Another phenomenon observed with our ceiling culture chip was the transfer of the LD content between adipocytes in contact with each other. Previously, Hu et al. have reported the direct communication between cells of eWAT explant via gap-junctional couplings [70], that aligns with the LD content exchange between neighboring adipocytes observed in our study. The transfer events were shown to occur over the course of 20 h either unidirectionally or bidirectionally. Interestingly, during the unidirectional transport, donors shrank dramatically following the transfer. This phenomenon may be interpreted as a cell's effort to preserve nutrient resources by transferring the lipid stored in the unhealthy cells to healthy neighbors. On the other hand, the latter events of mutual exchange were extremely rarely observed, specifically in the *Lats1/2* iAKO strain. Based on morphological analysis, the process seems to be associated with the dedifferentiation process. In addition, we developed and applied the shape index in order to quantitatively indicate the degree of dedifferentiation of adipocytes. Conventionally, the expression levels of preadipocyte markers, such as *Sca1*, *Cd34*, and *Pref1*, were profiled to identify the extent of dedifferentiation. Instead, the shape index can be measured without any antibody or agent, serving as a dynamic metric to characterize cells that are undergoing dedifferentiation. Despite the general perception of mature adipocytes as being rather static, we confirmed that adipocytes were, in fact, very dynamic, involving the active generation of mechanical stresses during the pathophysiological events. Furthermore, two fascinating phenomena of LD extrusion and LD transfer lead to new perspectives and opportunities for further studies in identifying the key regulators of accumulation and release of mechanical stresses through cytoskeletal remodeling during the dedifferentiation process.

Chapter 3. Modulation of metastatic potential of ovarian cancer model by mechanical memory[c]

3.1 Introduction

Throughout the process of metastasis, cancer cells are subject to spatiotemporally varying conditions of microenvironments, forced to adapt by altering their phenotypes. Among many, mechanical factors like tissue stiffness greatly impact the pathological behaviors of cancer via mechanotransduction signaling pathways. Many solid tumors, including breast cancer [71], colon cancer [72, 73], liver cancer [74], pancreatic cancer [75], and ovarian cancer [76, 77], tend to get stiffer than normal tissues, and this elevated stiffness leads to the emergence of the malignant phenotype in those cancer cells [78].

Less than half of patients with ovarian cancer survive for more than five years, making it a fatal disease [16]. Shear wave elastography (SWE) and atomic force microscopy (AFM) studies have shown that cancerous ovaries have inherent heterogeneities in Young's modulus that range several orders of kPa, up to >100kPa [79, 80]. Given that Young's modulus of the ovaries of young and healthy women is as low as 1.79 ± 0.08kPa [81], it is evident that the pathological condition must have caused significant alterations in the mechanical properties of the cancerous tissue. Furthermore, the heterogeneity in the stiffnesses is likely to result in a spectrum of cancerous phenotypes of constituent cells in a reciprocal manner between the cancer cells and their surroundings [78, 82, 83].

Emerging evidence also suggests that the mechanical footprint of the cells should be included in a holistic analysis of the interplay between the tumor and the microenvironment. For example, Nasrollahi *et al*. reported that cancer cells have *mechanical memory*, which means that the phenotypes they acquired as a result of cues from the prior environments remain even after the cues disappear. The authors demonstrated the existence of mechanical memory by culturing cells in a novel hydrogel-based platform that features spatially discontinuous stiffness gradient [84]. Cells that were initially primed on the stiff part sustained pro-migratory phenotypes even after they were moved to the compliant gel. The YAP activity was suggested as the cause of the mechanical memory in this paper. While this work provided a basis for the needs to consider the spatiotemporal changes in mechanical microenvironment experienced by the cells, especially in the metastatic cancer cells that travel through sites of varying mechanical stiffness, little has been studied due to the complexity involved with the metastatic routes.

Ovarian cancer metastasizes through the unique peritoneal route. First, the epithelial ovarian cancer cells, developed on the surfaces of the ovary, detach from the surface and into the peritoneal cavity [85]. The

[c] Contents of this chapter is in preparation with a title of "Mechanical memory regulates the metastatic potential of ovarian cancer in a spheroid-based *in vitro* peritoneal metastasis model", authored by Jiwon Kim, Hyuntae Jeong, Chanhong Min, and Jennifer H. Shin*.

detached cells then spontaneously form 3D aggregates for survival while those that failed to form spheroidal aggregates in the ascites have less chance to survive due to the lack of mechanical homeostasis and the vulnerability to immune surveillance. Spheroidal aggregates then attach to the peritoneum to disseminate. On the peritoneal surface, there are lymphatic portals open to the inside of the peritoneal cavity. These structures, called *milky spots*, lack basement membranes and expose the collagen I matrices, facilitating the adhesions of malignant spheroids [86-88]. Interestingly, peritoneal metastasis does not involve the complex microarchitectures of the circulatory system, thus making it feasible to construct an *in vitro* model for it.

In this study, we established an *in vitro* peritoneal metastasis model where ovarian cancer cells were mechanically primed on initial substrates of different stiffness to investigate how the prior exposure to varying mechanical environment impact the pathological behavior of the metastatic cells. Engineering approaches have been employed to recapitulate four essential stages of peritoneal metastasis: (i) primary cancer cells on different stiffness levels by mechanical priming on tunable hydrogels, (ii) floating malignant spheroids by hanging drop culture, (iii) attachment and dissemination on the milky spot by spreading assay on a 2D substrate, and (iv) further invasion into stroma by invasion assay in 3D ECM gel.

Intriguingly, soft-primed spheroids displayed slower spreading and less invasiveness than stiff-primed spheroids, hampered by the dense actin cage enveloping the soft-primed spheroid. We report that the ovarian cancer cells display mechanical memory that can be inherited over multiple passages, and the prior route of peritoneal metastatic paths facilitates the cells to sustain the memory by orchestrating conformational changes in the spheroidal cytoskeletons.

3.2 Materials and Methods

3.2.1 Cell line and reagents

The human epithelial ovarian adenocarcinoma cells, SKOV-3, were cultured in RPMI 1640 (Gibco; 11875) medium supplemented with 10% heat-inactivated fetal bovine serum (Welgene; S101-01) and 1% penicillin-streptomycin (Welgene; LS202-02).

3.2.2 Mechanical priming

Cover glasses with the size of 24×50 mm^2 were sterilized and dried in an 80˚C oven. The bind silane solution was made freshly before use with 40ml of 3-(trimethoxysilyl)propyl methacrylate diluted 1:200 in ethanol and 1.2ml of glacial acetic acid diluted 1:10 in di-water. The cover glasses were treated with the bind silane solution for 3 minutes and then rinsed with ethanol. While the glasses were dried, precursors for polyacrylamide (PA) gels with the stiffness of 1.2kPa, 11kPa, and 90kPa were prepared as previously known [89].

The PA-gel precursors were put on the pretreated glasses and covered by another piece of a non-treated cover glass. After polymerization, the covering glasses were carefully removed, and the PA gels were soaked with 0.05M HEPES buffer. Subsequently, sulfo-SANPAH solution diluted in 0.05M HEPES buffer was added to the PA gels, and the PA gels were exposed to UV light with the wavelength of 365nm for 15 minutes. The excessive sulfo-SANPAH solutions were eliminated by serial washing with 0.05M HEPES. 400μl of 100μg/ml collagen type I was laid on each PA gel and incubated overnight at 4˚C. The PA gels were washed with DPBS several times, and 5×10^4 SKOV-3 cells were seeded on the PA gel to be mechanically primed. The duration of mechanical priming was set to be 3 days to allow enough time for phenotypic adaptation. SKOV-$3^{1.2/11/90kPa}$ cells refer to the SKOV-3 cells primed on the PA gel with the stiffness of 1.2kPa, 11kPa, and 90kPa, respectively. Those cells were enzymatically detached with trypsin/EDTA from the PA gels to be examined or to aggregate into 3D spheroids.

3.2.3 Traction force microscopy and monolayer stress measurement

The PA gel of 3kPa was chosen for traction measurement based on the physiologically relevant elastic modulus of rodent peritoneal membrane [78], taking into account the amount of bead displacements for accurate calculation of traction. In addition, 3kPa does not overlap with any of the three priming stiffnesses, hindering cells primed in certain stiffness from having advantages in adapting to the new environment. The same PA gels as shown in 2.2 but with the fluorescent beads were fabricated. PDMS masks with an array of circular patterns with a diameter of 500μm were covered on the PA-gels. Being covered by the masks, the PA gels were treated with sulfo-SAPAH and coated with 100μg/ml collagen type I. SKOV-$3^{1.2kPa/11kPa/90kPa}$ cells were seeded on the gels through the holes of the PDMS masks. In 1 hour, the masks were removed with caution, and the excessive cells were washed off. The confined circular geometry was used to assess cellular stresses while restricting their motility as in the case of epithelial monolayer (Fig.3.2a). Furthermore, 20μM of thymidine was added to the media to arrest the cell cycle to minimize the undesired effects of actively dividing cells within the monolayer. The movements of cells and the fluorescent beads embedded in the gels were captured with an epi-fluorescence microscope (Zeiss, Axio Observer series) equipped with a microscope-mountable incubating system. On the day 2, the reference bead images were obtained by releasing the PA gels with trypsin/EDTA. Cellular traction was calculated based on the beads displacements and the monolayer stress was computed as described earlier [90].

3.2.4 Hanging drop culture

The previously described hanging drop culture method was adopted here. Briefly, a thin layer of PDMS (Sylgard 184, base:cure = 10:1) precursor mixture was poured on the lids of 100Φ Petri dishes and cured at 80˚C. After curing, the lids were cooled down at room temperature and sterilized. SKOV-$3^{1.2kPa/11kPa/90kPa}$ cells that had been primed for 3 days were detached from each PA gel and diluted to the concentration of 75,000 cells/ml. Each drop of suspension with a volume of 20μl containing 1,500 cells was placed on the PDMS-coated lids. The lids were flipped over on their own dishes containing 10ml of PBS. In 2 days, the

cells settled down near the surfaces of the drops and then aggregated into 3D spheroids. The spheroids were harvested with a pipette for further investigations.

3.2.5 Spreading assay

PA gels tuned to the stiffness of 3kPa were fabricated and coated with collagen type I as described in 2.2. SKOV-3$^{1.2kPa/11kPa/90kPa}$ spheroids were harvested at 48h and transferred gently to the 3kPa PA gels separately. To ensure that spheroids do come into contact with each other throughout the assay, care must be taken to widen the distance between the spheroids. The PA gels were mounted on an epi-fluorescence microscope equipped with an incubation system after 1-hour incubation to guarantee firm adhesion between the spheroids and PA-gels. Spreading spheroids were imaged for 24 hours with an interval of 1 hour. The extent to which the spheroids spread was quantified with the index of efficient radius, R_{eff}, as shown in Fig.3.9b.

3.2.6 Invasion assay

Collagen gel precursor with 2.0mg/ml concentration was prepared by diluting ice-cold collagen type I (CORNING, 354236) extracted from rat tail with autoclaved di-water and 10× PBS of a volume corresponding to 1/10 of the total volume. A few drops of 0.5M NaOH were added to adjust the pH to 6.8~7.2. All mixing procedure was done swiftly in an ice tray to prevent untimely solidification. Harvested SKOV-3$^{1.2kPa/11kPa/90kPa}$ spheroids were embedded in the collagen gel precursor. The dishes containing the precursor and spheroids were flipped over and over to prevent the sedimentation of spheroids. Complete solidification of the collagen-spheroid gel took 45 minutes in the incubator. The spheroids were imaged for 96 hours with an interval of 30 minutes. The sizes of growing center masses were quantified with the efficient Radius, R_{eff}. The extents to which the scattered cells infiltrated into the surrounding collagen matrix were quantified with the index of the distance to the tip, D_{tip}. D_{tip} represents the distance from the initial boundary of the center mass measured on the day of embedding to the tip of each scattered cell. Both R_{eff} and D_{tip} are illustrated in Fig.3.10b.

3.2.7 Unsupervised clustering

The phase-contrast images and binarized images were used for the extraction of texture features and morphological features, respectively. Basic morphology features, including Zernike moments, and Haralick texture features, were extracted from the images. Features with communality lower than 0.4 and ones of a pair of features with correlation values higher than 0.9 were dropped out for filtering out less significant and redundant features, respectively. The remaining features were used for factor analysis and subsequent unsupervised K-means clustering. In K-means clustering, the number of clusters was determined with the Elbow method. Hierarchical analysis was conducted based on Euclidean distance and the Ward method.

3.2.8 Cryosectioning

Harvested hanging drop spheroids were gently washed twice with PBS and then immersed in 4% Paraformaldehyde and 8% sucrose in PBS at 4˚C overnight. Serial immersions in 15% and then 30% sucrose solution each for more than 6 hours were followed. Then the spheroids were transferred to molds with an OCT embedding compound. After the spheroids settled down, the molds were snap-frozen and kept in -80˚C. The frozen block was sliced at 5~10 μm thickness in a cryostat set to -20~-15 ˚C and then collected onto adhesive slides.

3.2.9 Immunostaining

SKOV-3$^{1.2kPa/11kPa/90kPa}$ cells in 2D monolayer form, after mechanical priming, were washed twice with PBS and then fixed with 4% Paraformaldehyde for 20 minutes at room temperature. Fixed cells were again washed 3 times with PBS for 3 minutes each. Then the cells were moved onto an ice block to be permeabilized for 15 minutes with permeabilization buffer (0.2% (v/v) Triton X-100 in PBS). Next, Permeabilized cells were rinsed three times with PBS, 10 minutes each. After washing, blocking buffer (3% (w/v) BSA in PBS) was added for non-specific binding. The buffer was replaced with a fresh buffer in 30 minutes. In another 30 minutes, the blocking buffer was removed.

When the target proteins were membrane proteins, live cells were treated with ice-cold pre-treatment buffer (4% paraformaldehyde and 0.2% Triton X-100 in PBS) for 3 minutes and then washed twice with chilled PBS prior to the usual fixation process. In this case, the permeabilization step was skipped. When staining the cryostat sections, excessive fixation was avoided. Being rehydrated with PBS for 15 minutes, the sections were permeabilized and blocked as usual. 0.2% Triton X-100 was supplemented in every staining and washing process.

After blocking, the cells were incubated at 4˚C overnight with the primary antibody diluted according to the manufacturer's recommendations. Next, cells were washed three times with PBS for 30 minutes each and incubated with secondary antibody diluted in 3% BSA (200:1) for 2 hours at room temperature, being in the dark. Depending on the cases, the cells were stained with another pair of primary and secondary antibodies or stained with Alexa Flour conjugated Phalloidins diluted in 3% BSA (50:1) for 30 minutes at room temperature. Finally, cells were washed three times for 10 minutes each with PBS, before and after being stained with 300nM DAPI solution for 3~5 minutes. The stained cells were immersed with a few drops of mounting medium and sealed with a coverslip and nail polish.

3.2.10 qPCR

SKOV-3$^{1.2kPa/11kPa/90kPa}$ in 2D monolayer form or in 3D spheroidal form were washed twice with PBS. mRNAs were collected with RNAiso Plus (Takara, 9109) according to the manufacturer's instructions. Briefly, washed cells were dissolved with 1ml of RNAiso Plus for every 5×10^6 cells at room temperature.

Chloroform of 0.2 volume of RNAiso Plus was added to the solution. After being vortexed vigorously, the solution was centrifuged at 12,000*g* for 15 min at 4˚C. Only the transparent top layer was separated, and isopropanol of 0.5~1.0 volume of RNAiso Plus was added here. The mixture was kept at room temperature for 10 minutes and centrifuged at 12,000*g* for 10 min at 4˚C. Precipitated mRNA was cleaned with 75% ethanol and air-dried. mRNA precipitation was dissolved in RNase-free water to measure purity and concentration by Nanodrop spectrophotometer (ND1000, Thermo fisher). cDNA was synthesized using the iScript™ cDNA kit (BioRad, 1706691). qPCR was performed with iQ™ SYBR® Green supermix (BioRad, 1708582) and C1000™ thermal cycler (BioRad), according to the manufacturer's instruction. Sequences of the primers are shown in Table S1. The level of mRNA expression was compared based on the -ΔC(t) values normalized by *GAPDH*.

Table 3.1 Sequences of primers used in the qPCR

mRNA	Forward	Reverse
GAPDH	CTGGGCTACACTGAGCACC	AAGTGGTCGTTGAGGGCAATG
ECAD	ATTTTTCCCTCGACACCCGAT	TCCCAGGCGTAGACCAAGA
NCAD	AGCCAACCTTAACTGAGGAGT	GGCAAGTTGATTGGAGGGATG
PCAD	TGGAGATCCTTGATGCCAATGA	GCGTCCAGATCAGTGACCG
INTβ1	CCTACTTCTGCACGATGTGATG	CCTTTGCTACGGTTGGTTACATT
INTβ4	CTCCACCGAGTCAGCCTTC	CGGGTAGTCCTGTGTCCTGTA
HDAC3	TCTGGCTTCTGCTATGTCAACG	CCCGGTCAGTGAGGTAGAAAG
HDAC8	TCGCTGGTCCCGGTTTATATC	TACTGGCCCGTTTGGGGAT
YAP1	TAGCCCTGCGTAGCCAGTTA	TCATGCTTAGTCCACTGTCTGT
RUNX2	TGGTTACTGTCATGGCGGGTA	TCTCAGATCGTTGAACCTTGCTA

3.2.11 Statistical analysis

When the independent variables have only one level, one-way ANOVA and Tukey *post hoc* were selected for statistical analysis. In the case that the independent variables have two levels, two-way ANOVA and Tukey *post hoc* were selected to measure the q-, p-values, and interactions. All statistical analyses were conducted with Origin Pro (OriginLab) software.

3.3 Results

3.3.1 Establishment of an *in vitro* peritoneal metastasis model

Primary ovarian tumor is known to feature a broad range of mechanical stiffness over its surface. Ovarian cancer cells from the tumor surface of heterogeneous stiffness exfoliate into the peritoneal effusion in the abdominal cavity to metastasize along the peritoneal metastatic route. Because cells are known to take different phenotypes on the surfaces of different mechanical stiffness [78, 82], we hypothesized that the exposure to different stiffness of the primary tumor site may result in a spectrum of distinct phenotypes of departing cells. To investigate how the metastatic ovarian cancer cells of different phenotypes respond to newly encountered secondary tumor sites, we established an *in vitro* model for the peritoneal metastasis.

Mimicking the step of the primary tumor, where the cells are still attached on the ovarian surface of heterogeneous stiffness, we cultured SKOV-3 cells on the PA gels of different Young's moduli: 1.2kPa, 11kPa, and 90kPa. This process was described as *mechanical priming* and the primed cell groups were named as SKOV-3$^{1.2kPa}$, SKOV-3^{11kPa}, and SKOV-3^{90kPa}, with the designated values of priming stiffness (Fig.3.1). As illustrated in Fig.3.1, ovarian cancer cells detach themselves from the tumor surface into the peritoneal cavity as the first step to the peritoneal metastasis, and the detached cells aggregate into compact clusters among themselves. To best simulate the anchorage-lacking cavity environment, we induced cells to form spheroidal aggregates for 2 days using *hanging drop culture* methods to exclude any contacts between the cells and solid substrates (Fig.3.1). As a final step, the clusters of malignant cells land on the milky spots of the peritoneal membrane and penetrate into the connective tissue *in vivo*. We defined both the spreading (2D) and invading (3D) behavior on the milky spots as the metrics to assess metastatic functions of ovarian cancer and tested whether our spheroids primed on substrates of different stiffnesses have differential behaviors that reflect the memory from prior experience. To comparatively analyze their metastatic potentials, SKOV-3$^{1.2kPa/11kPa/90kPa}$ spheroids were either placed on 3kPa PA gels coated with collagen type I for 2D spreading assay and embedded in the collagen block for the 3D invasion assay as shown in Fig.3.1. In following sections, each step of the metastatic route is evaluated by employing appropriate experimental tools. First of all, the efficacy of the mechanical priming is assessed by comparing the stress distributions and gene expression levels of SKOV-3$^{1.2kPa/11kPa/90kPa}$. The spheroids to model malignant clusters are characterized by checking both gene and protein expressions. Finally, the metastatic functions of the tumor cells on milky spot are tested by 2D spreading and 2D invasion assays.

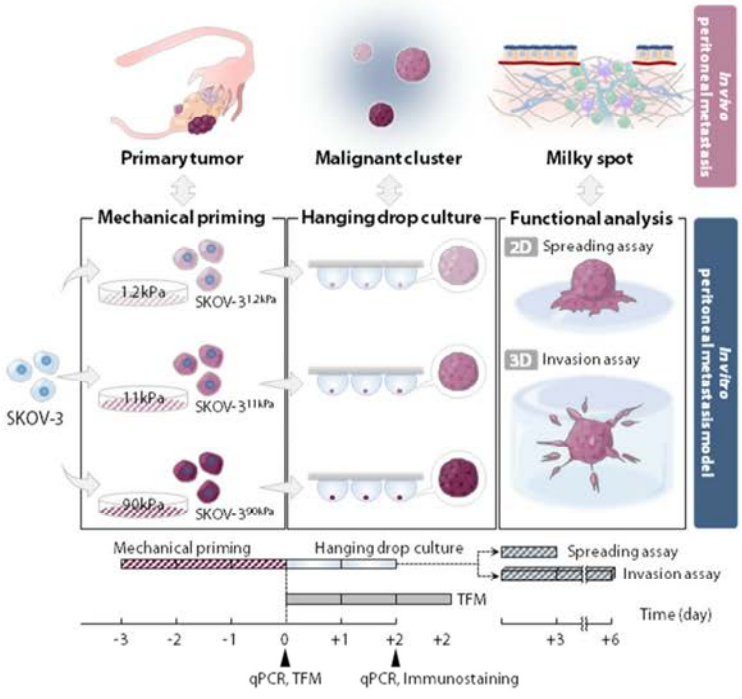

Figure 3.1 Establishment of an *in vitro* peritoneal model. SKOV-3 ovarian cancer cells were primed on collagen-coated PA-gels tuned to three different stiffness levels, 1.2kPa, 11kPa, and 90kPa. Primed cells, namely the SKOV-$3^{1.2kPa/11kPa/90kPa}$, were aggregated into hanging drop spheroids. The metastatic potentials of SKOV-$3^{1.2kPa/11kPa/90kPa}$ in 2-/3-D microenvironments were tested with spreading/invasion assays, respectively (**a**). The timeline of experiment (**b**).

3.3.2 Efficacy of mechanical priming: Soft-primed cells behave more cohesively than stiff-primed cells

To test the efficacy of mechanical priming on the substrates of different stiffness, we cultured SKOV-3 on three different substrates (1.2kPa, 11kPa, and 90kPa) for 3 days. We then measured cellular traction force to quantify the difference in the physical state of the cells cultured on different priming substrates. As the adherent cells cultured in a monolayer continuously exert stresses against the substrate and the neighboring cells, which vary depending on the extent of cell-substrate and cell-cell interactions, the traction and monolayer stress can be regarded as integrated indicators of the cellular state[91, 92]. The PA gel of 3kPa was chosen as the testing substrate to estimate both traction and monolayer stress. Fig. 3.2b-d display the priming stiffness-dependent spatiotemporal distributions in both traction and monolayer stress. During the early hours (first 12 hours), the traction (t_r) maps of all three samples feature similar patterns, with the peripheral cells exerting intense inward tractions while the inner layer cells resist with opposite tractions (Fig. 3.2b-d). Between 12-24 hours, the resisting outward traction disappears in the SKOV-$3^{1.2kPa}$ while the intercellular stresses are highly intensified with the intensity peak at the center of the circular monolayer. These results confirm that the long-range intercellular stress spans over the length scale of the entire monolayer, holding the whole pack of cells together, which requires the traction forces on the peripheral cells to be balanced by the ones at the opposite end, as schematically illustrated in the bottom panel of Fig.3.2b. Beyond 24 hours, as the intercellular stresses decay, the intercellular stress range becomes shorter, resulting in alternating traction polarities. On the other hand, the intercellular stress map of SKOV-3^{90kPa} exhibited a much lower average value. Along with the traction map, the decrease in the intercellular stress can be comprehended as a result of the stress in the boundary cells being counterbalanced by the adjacent inner cells that are polarized oppositely (Fig.3.2d). Given that the cellular proliferation was inhibited by thymidine treatment, the monolayer stresses in the central region are more likely to have been transmitted from the boundary cells rather than arisen on that spot spontaneously (Fig.3.2b, e). By comparison, SKOV-3^{11kPa} exhibited intermediate trends of tractions and intercellular stresses, implying a coherent correlation between the priming stiffness and the resulting phenotypes (Fig. 3.2c).

3.3.3 Efficacy of mechanical priming: Genes involved in cell adhesion express regardless of the priming stiffness

In order to find a clue on how the SKOV-3 cells acquired different behavioral traits by the mechanical priming phase on the different priming stiffnesses, we checked the gene level expression of a few well-known key players responsible for cell-cell adhesions and cell-substrate adhesions. First of all, despite the clear difference in stress maps between SKOV-3^{90kPa} and SKOV-$3^{1.2kPa}$, the difference in the E-cadherin mRNA expression levels of in SKOV-$3^{1.2kPa}$ and SKOV-3^{90kPa} was not significant (Fig.3.3b, Table.3.2).

Similarly, the P-cadherin expression level was lower in SKOV-3^{90kPa} than in SKOV-3$^{1.2kPa}$, but the difference was not statistically significant (Fig.3.3d, Table.3.2). Both E-cadherin and P-cadherin were expressed mainly in the cytoplasm, not at the membrane (Fig.3.4).

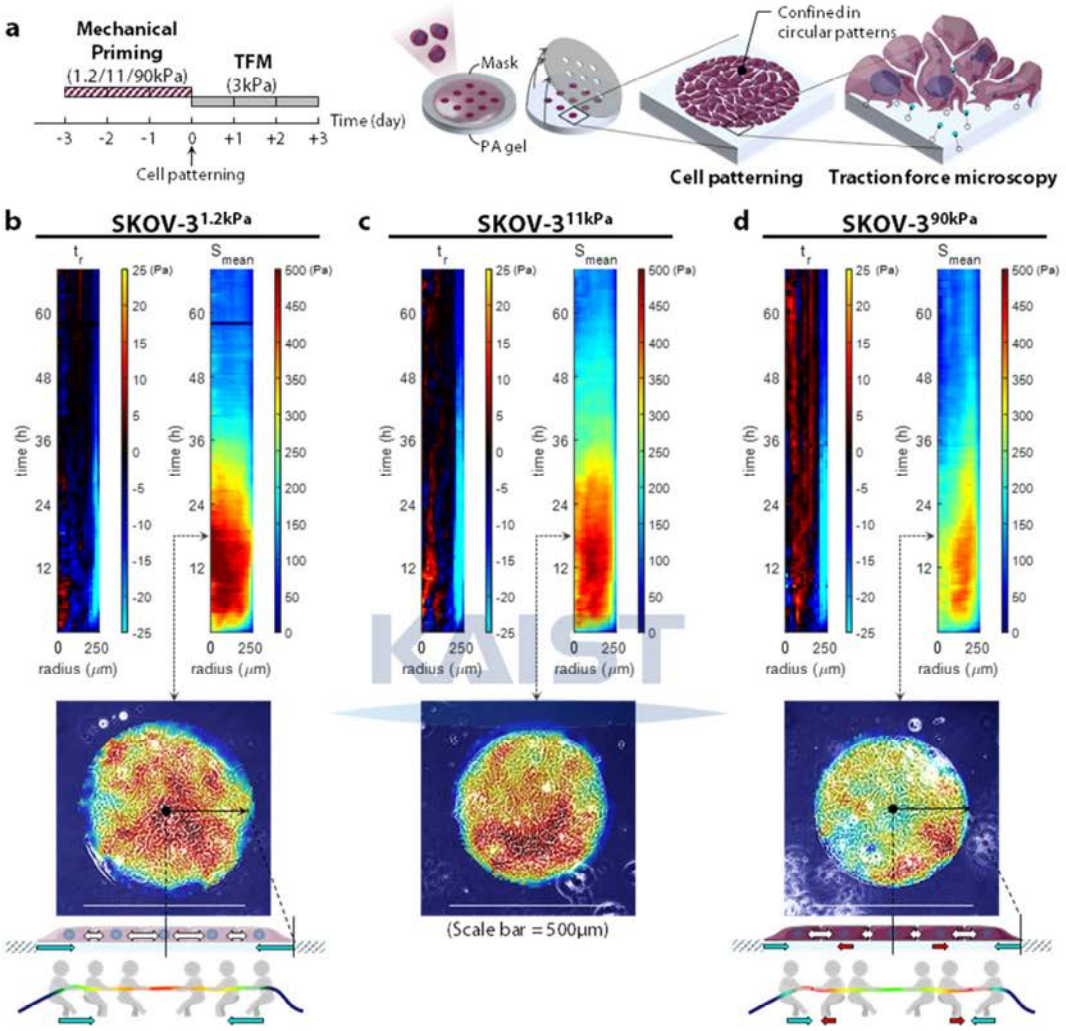

Figure 3.2 Soft-primed and stiff-primed cells represent different modes of tractions and intercellular stresses. SKOV-3$^{1.2kPa/11kPa/90kPa}$ cells were patterned in confined circular patterns with a diameter of 500μm right after the mechanical priming. 1 μM of Thymine was treated to inhibit the uncontrolled proliferation (**a**). SKOV-3$^{1.2kPa/11kPa/90kPa}$ cells showed similar distributions of tractions at first. However, the inner and outward components (indicated as red color close at radius = 0) diminished in SKOV-3$^{1.2kPa}$, while flourishing in SKOV-3^{90kPa}. As a result, SKOV-3$^{1.2kPa}$ exhibited a high accumulation of intercellular stress at the center of the circular pattern. On the contrary, stresses in the SKOV-3^{90kPa} patch could not be delivered inward and became weak at the periphery. SKOV-3^{11kPa} showed intermediate trends (**b-d**). The accumulation of stresses in SKOV-3$^{1.2kPa}$ indicates that the stress occurring at the boundary was easily transferred inward, likely owing to high cell-cell interactions (**e**). However, the peripheral and core cells of the SKOV-3^{90kPa} patch are polarized in opposite directions, being in a relatively independent mechanical state (**f**).

We also explored other junction proteins responsible for the cell-ECM adhesion and cell-cell cohesiveness, but neither of N-cadherin, Integrin β1, and Integrin β4 expressed depending on the priming stiffnesses. Instead, E-cadherin, P-cadherin, and Integrin β4 expressed significantly higher in cells after being made into hanging drop spheroids than in 2D cells right after mechanical priming (Fig.3.3c, e, f, Table.3.2).

Therefore, we concluded that there would be other reasons for the disparities in the cellular cohesivity shown previously other than the immediate effects the gene expression levels of the adhesion molecules.

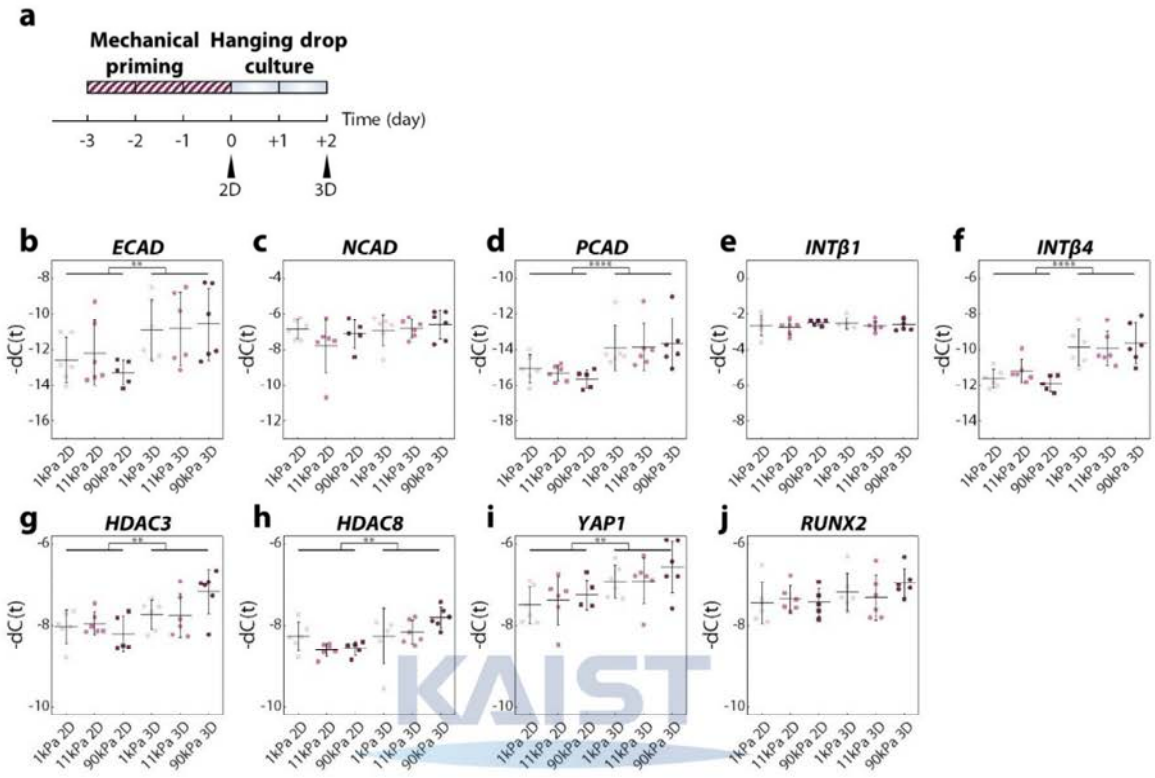

Figure 3.3 Both after mechanical priming (2D) and after hanging drop culture (3D) (**a**), SKOV-3$^{1.2kPa/11kPa/90kPa}$ cells did not show significantly different expressions of mRNA that are involved in cytoskeletal structures (**b-f**) or to epigenetic regulation (**g-j**). E-cadherin, P-cadherin, Integrin β4, HDAC3, HDAC8, and YAP1 expressed higher in hanging drop spheroids than in 2D monolayer (**j**). Two-way ANOVA test with Tukey *post hoc*.

Table 3.2 Two-way ANOVA test with Tukey *post hoc* on qPCR results (Fig.3.3b-j).

mRNA	Dimension		Priming stiffness		Interaction	
	F-val	P-val	F-val	P-val	F-val	P-val
ECAD	11.06578	**0.0024**	0.1691	0.84525	0.47072	0.62924
NCAD	2.41396	0.1311	0.8518	0.43705	1.00807	0.37735
PCAD	18.65809	**1.67014E-4**	0.08226	0.92124	0.44158	0.64727
INTβ1	0.07561	0.78529	0.59837	0.55635	0.37186	0.69269
INTβ4	38.40724	**9.28185E-7**	0.19463	0.8242	1.02611	0.37104
HDAC3	11.63622	**0.00192**	0.64272	0.53319	3.15858	0.05741
HDAC8	10.30655	**0.00323**	0.8749	0.42762	2.96695	0.06725
YAP1	11.04383	**0.00242**	1.05398	0.36152	0.1087	0.89737
RUNX2	3.09834	0.08892	0.32862	0.72256	0.69913	0.5052

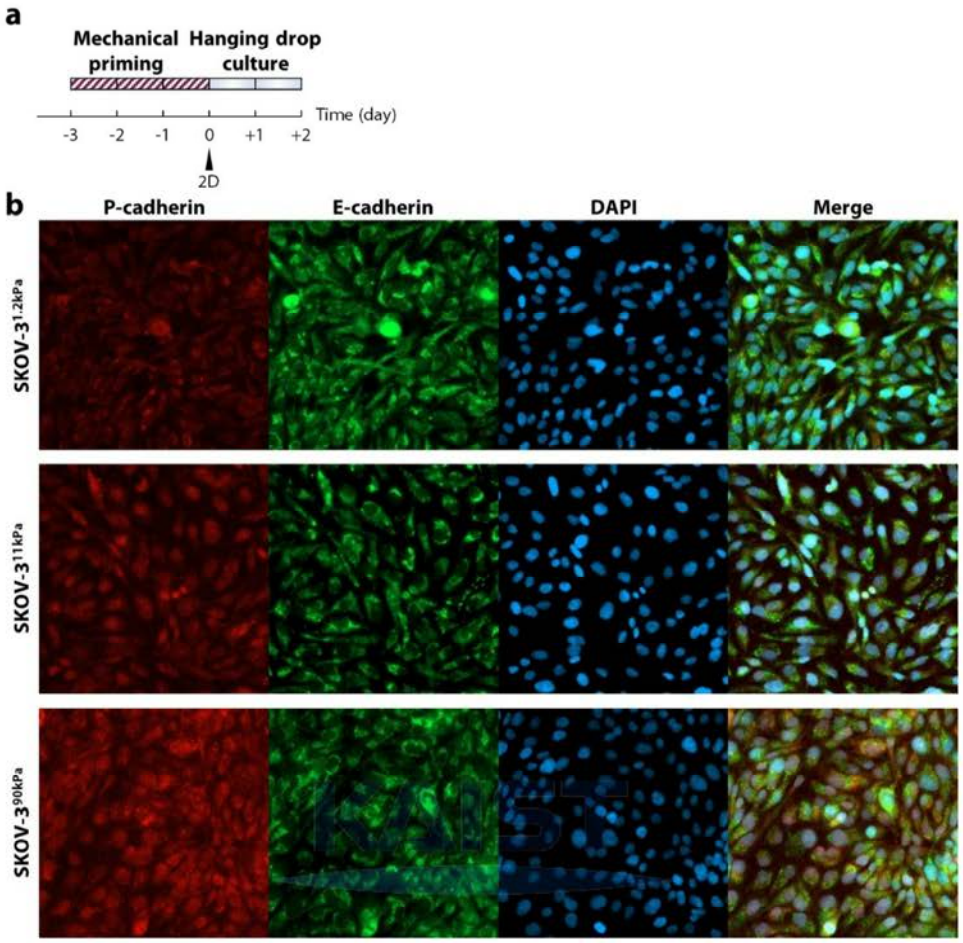

Figure 3.4 SKOV-3$^{1.2kPa/11kPa/90kPa}$ after mechanical priming (a) expressed E-/P-cadherin mostly in cytoplasm, not localized in cell surfaces (b).

3.3.4 Assessment of spheroids: 3D aggregation of cancer cells elevates genes related to epigenetic plasticity

External stiffness cues are transmitted along the ECM-integrin-cytoskeleton axis and converted into chemical signals to alter the cell's fate in both transient and permanent manner [93]. Recent studies on cancer pathology and developmental biology have clarified that these mechanical cue induced regulatory events on cell fates incur epigenetic plasticity [7]. For example, histone deacetylases (HDACs) modify histone structure by trimming acetylation on a histone protein, and HDAC3 and HDAC8 are known to induce stiffness-mediated tumorigenicity in breast cancer [94]. In our model, SKOV-3 cells of all priming stiffness showed increase in HDAC3 and HDAC8 expressions after having aggregated through the hanging drop culture (Fig.3.3g, h, Table.3.2). Especially, SKOV-3^{90kPa} cells showed the most significant increase in both HDAC3 and HDAC8. Furthermore, Yes-associated protein (YAP), one of the most well-known mechanotransducers, was upregulated after hanging drop culture with a weak dependence on the priming stiffness, evidenced by the mean fluorescence intensity (Fig.3.5b, c). While YAP is generally known to participate in a positive feedback loop of epigenetic regulation induced by a stiff environment [95], YAP was shown to play an indispensable role in maintaining mechanical memory [84]. Runt-related transcription

factor 2 (RUNX2), involved in the stiffness-induced epigenome [96], also displayed similar trends with YAP (Fig.3.3j, Table.3.2), consistently supporting the sustained mechanical memory during the spheroidal aggregation via hanging drop culture. The phase of cellular aggregation that mimics the *in vivo* formation of malignant spheroids must maintain the stiffness-induced mechanotransduction even after the primed cells departing from the stimulating source of the stiff environment.

3.3.5 Assessment of spheroids: Soft-primed cells form compact spheroids featuring actin cage structure

In a hanging drop, the cells gather at the bottom of the drop to form loose aggregates, which will then undergo compaction over time. To track down the compaction processes, we monitored the aggregation process at 24 hours and 48 hours from the seeding. Between two time points, the effective diameters (D_{eff}) of SKOV-$3^{1.2kPa}$ aggregates have dropped the most. The ratios of the averaged D_{eff} on Day 2 to those on Day1 of the hanging drop culture (Formula 1) were 88.7%, 92.1%, and 91.2% for SKOV-$3^{1.2kPa/11kPa/90kPa}$, respectively, demonstrating most compaction in the SKOV-$3^{1.2kPa}$ aggregations (Fig.3.6b, Table.3.3). This strong compaction of the aggregates aligns with the above-mentioned the stronger cohesiveness of SKOV-$3^{1.2kPa}$.

$$\frac{\frac{1}{n}\sum (D_{eff})_{Day2}}{\frac{1}{m}\sum (D_{eff})_{Day1}} (\%) \quad (1)$$

Furthermore, the harvested SKOV-$3^{1.2kPa}$ spheroids featured distinct actin structures, where the actin fibers were concentrated along the periphery of the spheroid section with less actin in the core, forming a ring-shaped actin cage. The intensity profiles provide more obvious indication of actin cages, evidenced by prominent peaks on both ends (Fig.3.7b). Some of the SKOV-3^{11kPa} spheroids also displayed actin cages (Fig.3.7c), but none of the SKOV-3^{90kPa} spheroids showed the caging structures. Instead, inner cells in the SKOV-3^{90kPa} spheroids expressed comparable actin levels with the peripheral cells.

To quantitatively compare the expression patterns of the actin, we carried out principal component analysis (PCA) and unsupervised clustering based on the texture features extracted from the actin images of SKOV-$3^{1.2kPa/11kPa/90kPa}$ spheroids (Table.3.4). We set the number of clusters to 2, and the dichotomy concisely sorted the SKOV-$3^{1.2kPa}$ and SKOV-3^{90kPa} spheroids. All SKOV-$3^{1.2kPa}$ spheroids belonged to cluster 1, while all SKOV-3^{90kPa} spheroids belonged to cluster 2, with the SKOV-3^{11kPa} spheroids sitting on the fence (Fig.3.7e).

The structural differences in the spheroids indicate that the prior exposure to the different stiffness levels can influence the subsequent compaction processes during the hanging drop. Furthermore, the priming stiffness-dependent distributions of actin structure, the fundamental component in cell migration, must infer

that the migratory phenotypes of the spheroids can differ, which will be confirmed by the functional assays in section 3.3.6.

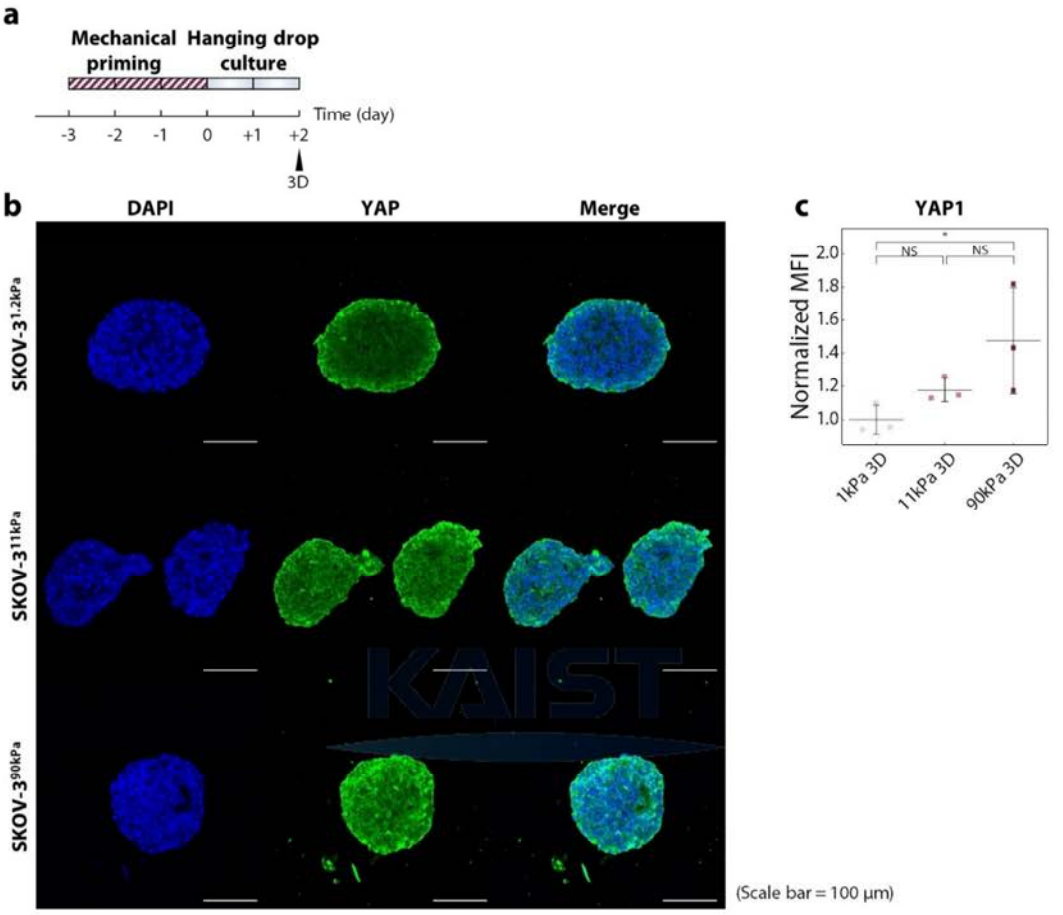

Figure 3.5 After 2 days of hanging drop culture (a), SKOV-3^{90kPa} spheroids expressed YAP1 the highest among SKOV-3$^{1.2kPa/11kPa/90kPa}$. The expressions were mostly not nuclear and concentrated in the peripheral regions (**b,c**). One-way ANOVA test with Fisher's LSD *post hoc*.

3.3.6 Assessment of spheroids: Stiff-primed cells develop spheroids bearing lumen-like voids

The spheroids of different priming stiffnesses exhibited another morphological disparity during the hanging drop culture: Most spheroids displayed lumen-like voids. The number and size of the voids appeared to increase as the priming stiffness increased (Fig.3.7f). The increasing trend was quantified with three indices;

proportion (%) of area accounted by the voids out of the whole spheroidal area, the number of the voids per each spheroid section, and the area of the individual void. Both the number and size of each void significantly elevated with the priming stiffness, resulting in the highest proportion of voids in the SKOV-3^{90kPa} spheroids (Fig.3.7g-i). Interestingly, the spheroids with lumen-like voids resemble the blastruloid-like aggregates found in patients' ascites. Langthasa *et al*. have reported that malignant aggregates extracted from the patients and cellular spheroids generated with immortalized cell lines of ovarian cancer turned out

to feature lumen-like voids and even undergo moruloid-blastruloid transition over time [97]. Along with the actin cage, differences in lumen formation stress that the spheroids exhibit different inner architecture according to their mechanical memories, which are also likely to result in disparities in metastatic potentials [98].

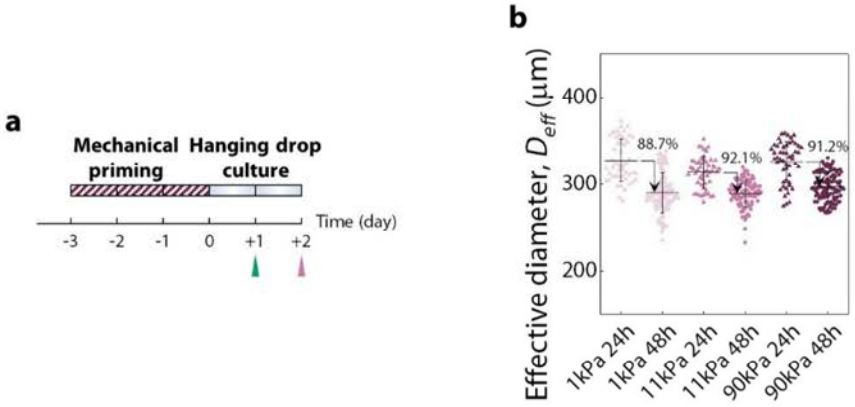

Figure 3.6 From the day 1 to the day 2 of the hanging drop culture (a), SKOV-3$^{1.2kPa}$ spheroids compressed most abruptly, as demonstrated with the smallest compression ratio. $n_{1kPa\ 24h}$= 51, $n_{11kPa\ 24h}$= 53, $n_{90kPa\ 24h}$= 52, $n_{1kPa\ 48h}$= 134, $n_{11kPa\ 48h}$= 118, $n_{90kPa\ 48h}$= 146 (**b**). Two-way ANOVA test with Tukey *post hoc*.

Table 3.3 Two-way ANOVA test with Tukey *post hoc* on the spheroidal compression (Fig.3.7b).

		SKOV-3$^{1.2kPa}$	SKOV-3^{11kPa}	SKOV-3^{90kPa}
mean D_{eff} (μm)	Day 1	327.757 ± 24.672	314.261 ± 18.303	326.063 ± 23.358
	Day 2	290.645 ± 23.123	289.490 ± 15.280	297.456 ± 16.098
Compression ratio		88.7%	92.1%	91.2%
P-val		1.768E-14	4.689E-13	1.719E-11

3.3.7 Functional analysis: Stiff primed spheroids exceed in spreading rates regardless of the initial size

After the investigation of the inner structures at the end of the hanging drop culture, functional assays were carried out to evaluate the invasiveness of the spheroids with histories of mechanical priming on different levels of stiffness. The stiffness of PA gel on which the spreading assays were conducted was determined to 3kPa, as described previously in 3.2. Spheroids were harvested and transferred to the PA gel to be investigated the spreading motion in a 2-dimensional environment mimicking the initial adhesion onto the milky spots in the mesothelium surfaces (Fig.3.9a, b). Upon the transfer, the spheroids lost their original spherical shape, developed pseudopods, and finally spread into two-dimensional cell collectives featuring irregular boundaries. The effective radii (R_{eff}) of the projection area of the cell collectives were quantified (Fig.3.9b). Representative kymographs tracing the temporal course of the spreading show that the spreading functionalities of SKOV-3 spheroids also depend on the priming stiffnesses (Fig.3.8c-e). The subsets show each spheroid at 24 hours of spreading assay, and the white solid lines in the subset indicate the ROIs selected for generating the kymographs. The spreading rate appeared the highest in the SKOV-3^{90kPa}, except for the initial 6 hours (Fig.3.9f). For a detailed analysis, the spreading rates measured every 2 hours were

again averaged within 4 temporal phases of 6 hours each. For the initial 6 hours, there were no significant differences between the spreading rates, except that the spreading rates of the SKOV-3^{90kPa} spheroids showed a much larger standard deviation than that of the other spheroids (Fig.3.9g). However, at 6~12 hours, SKOV-3^{90kPa} spheroids began to outrun the SKOV-$3^{1.2kPa}$ significantly (Fig.3.9h). The trend maintained until 18 hours after the onset of observation (Fig.3.9i), becoming negligible for the last 6 hours (Fig.3.9j). In later phases, only SKOV-$3^{1.2kPa}$ held spheroids whose spreading rates were under 30 μm/2hr (marked as dotted lines). Furthermore, SKOV-$3^{11kPa/90kPa}$ also did not have any spheroid belonging to the lagging group after 12 hours, underscoring that there are inherent gaps between the groups.

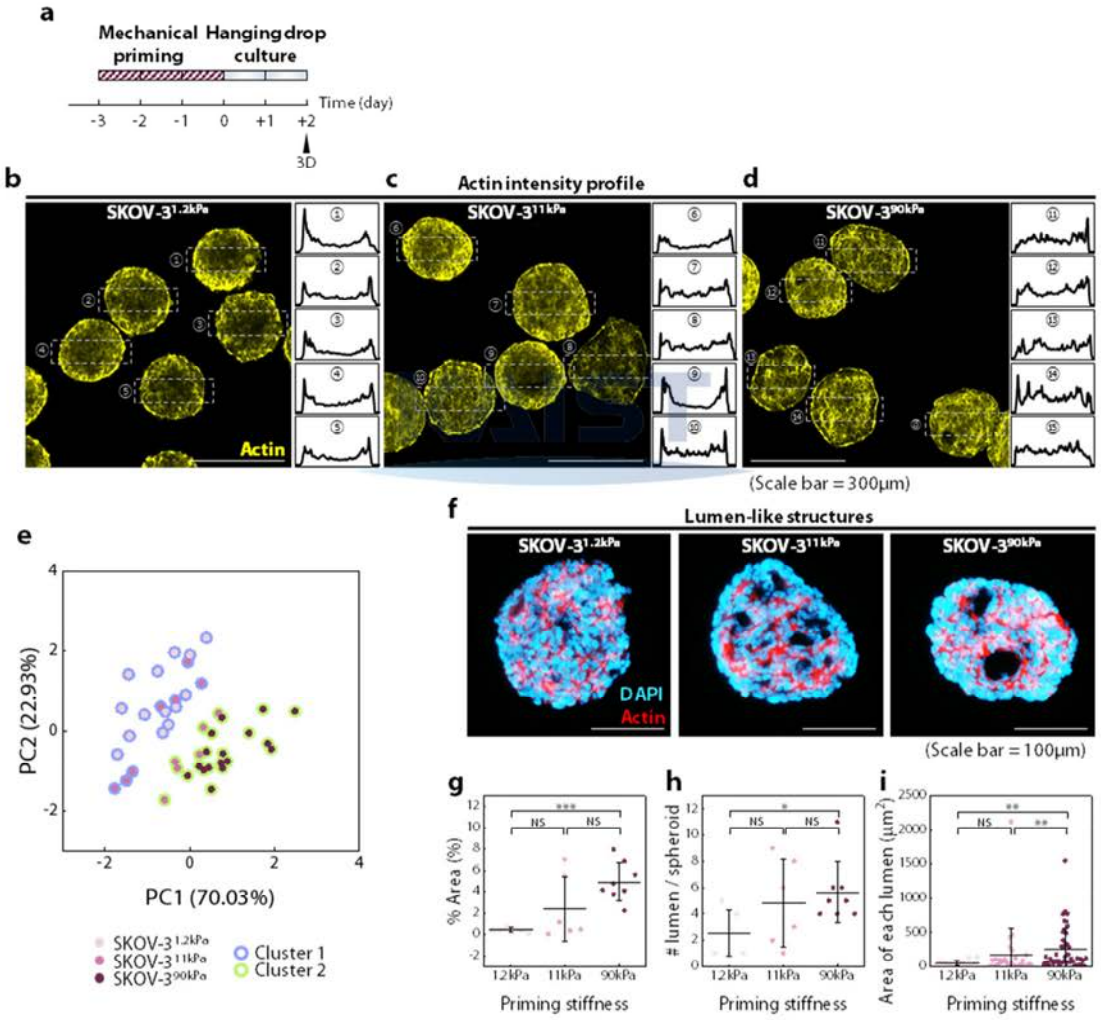

Figure 3.7 On day 2 of hanging drop culture (a), inner architectures of spheroids vary depending on the priming stiffness. Some of the hanging drop spheroids on day2 featured *actin cage structures* inside them (**b**). The spheroids were sorted by the completeness of actin cage structures. SKOV-$3^{1.2kPa}$ spheroids accounted for 86% of spheroids with complete actin cage structures (**c**). SKOV-3^{90kPa} spheroids featured unique lumen structures inside them (**d**). The %Area of voids out of the whole area of each spheroidal cross-section (**e**), number of lumens per each spheroid (**f**), and the area of each lumen itself (**g**) were quantified, and SKOV-3^{90kPa} ranked most high values in three of the quantifying indices. One-way ANOVA test with Tukey *post hoc*.

Table 3.4 Parameters used in unsupervised clustering based on the actin structure of SKOV-3$^{1.2kPa/11kPa/90kPa}$ spheroids (Fig.3.7e).

KMO and Bartlett's test

Kaiser-Meyer-Olkin Measure of Sampling Adequacy	0.687414	
Bartlett's Test of Sphericity	Approx. Chi-Square	3158.083
	Significance	0.0

Parameter	Communality	Eigenvalue	PC1	PC2
1 Angular second moment	0.834577	9.10E+00	-0.90349	0.135246
2 Contrast	0.861982	2.98E+00	0.899707	0.22915
3 Correlation	0.895221	5.48E-01	-0.32037	0.890271
4 Variance	0.921489	1.92E-01	0.762489	0.58318
5 Inverse difference moment	0.98907	1.06E-01	-0.97128	0.213733
6 Sum average	0.911849	4.39E-02	-0.95332	0.055077
7 Sum variance	0.922706	1.47E-02	0.75017	0.599959
8 Sum entropy	0.968248	7.92E-03	0.969808	0.166493
9 Entropy	0.985937	1.40E-03	0.992933	-0.00448
10 Difference variance	0.973954	7.27E-04	-0.98127	0.105216
11 Difference entropy	0.987463	1.45E-04	0.99352	0.019543
12 Information measures of correlation 1	0.970268	2.80E-05	0.708975	-0.68383
13 Information measures of correlation 2	0.862132	-1.53E-16	-0.02345	0.928215
		Eigenvalue	9.10435	2.980546
		Variance	0.700335	0.229273
		Cumulative variance	0.700335	0.929607

Correlation matrix

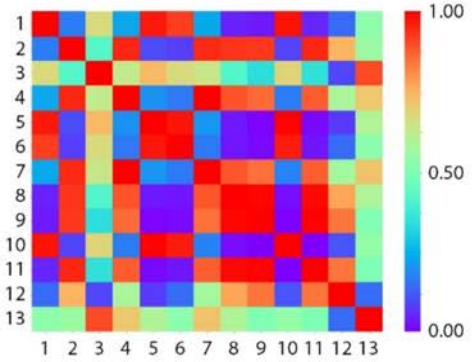

3.3.8 Functional analysis: Stiff primed spheroids invaded the fastest with the slowest growth of center mass

The malignant spheroids found in ovarian cancer patients complete peritoneal metastasis by penetrating into the milky spots where collagen type I is abundant. To recapitulate the context *in vivo* invasion, the spheroids were embedded into a three-dimensional collagen gel. As the timescale of invasion was much longer than that of spreading, the duration of observation was set to 4 days. Two different indices were used to describe the motile phenotypes of spheroids, the effective radius of the center masses, R_{eff}, and distance from the surface of the initial center mass to the tip of an escaping cell, D_{tip} (Fig.3.10a, b). Since a single spheroid can have multiple cells that are penetrating surroundings, a spheroid can have multiple values of

D_{tip}, while only one of R_{eff} at a certain time point. The representative image of this invasion assay shows that the SKOV-3^{90kPa} invaded the farthest, in line with the result of spreading assays (Fig.3.10c-e). Interestingly, the actin cage structure featured in SKOV-$3^{1.2kPa}$ spheroids right after the hanging drop culture was maintained as long as 6 days after collagen embedding. The confocal images were taken from the spheroids that were fixed 2 more days after the 4 days of invasion assay. Furthermore, the intensity profile shows that actin expression remained strong at the surface of the center mass of the SKOV-$3^{1.2kPa}$ spheroid (Fig.3.10f). In the SKOV-3^{90kPa} spheroid, on the contrary, the actin was mostly expressed at the core (Fig.3.10g).

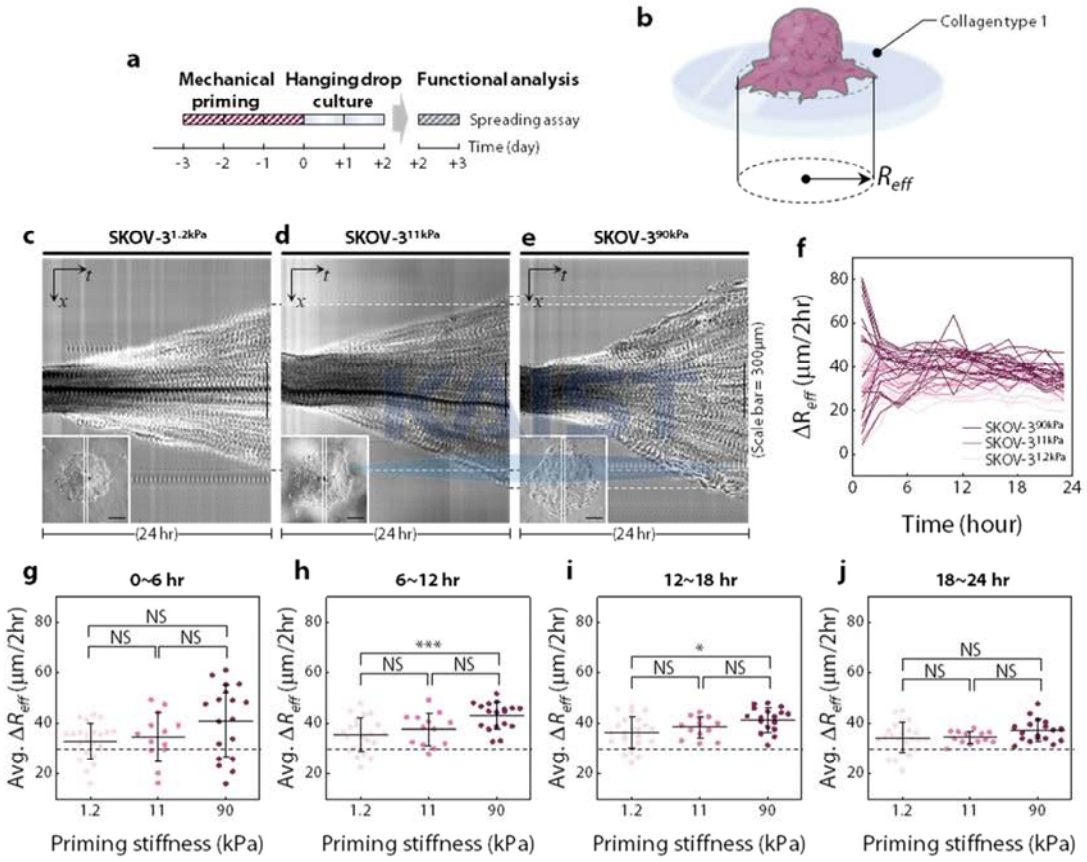

Figure 3.8 Spreading assays on collagen-coated PA gel were conducted as a measurement of metastatic potential of hanging drop spheroids on the 2D microenvironment (a). The extents to which the spheroids spread were quantified with the index of efficient radius, R_{eff} (**b**). Profile of SKOV-$3^{1.2kPa/11kPa/90kPa}$ spheroids at the beginning (0 hr, white line) and at the end (24 hr, yellow line) of the spreading assay, respectively (**c-e**). ΔR_{eff} measured every 2 hours shows that the SKOV-3^{90kPa} spheroid spread at a relatively high rate (**f**). The average value of ΔR_{eff} every 6 hours shows that the spreading rates have no significant differences during the first 6 hours (**g**). However, SKOV-3^{90kPa} exceeded the others during the next 12 hours (**h-i**). The rate becomes similar during the last 6 hours. However, all of the lagging group belongs to the SKOV-$3^{1.2kPa}$ (**j**). N=3, $n_{1.2kPa}$ = 23, n_{11kPa} = 14, n_{90kPa} = 18, n: number of spheroids. One-way ANOVA test with Tukey *post hoc*.

Another noticeable difference between the spheroid groups was the growth rate of the center masses. When quantified with the increment of R_{eff} during 4 days (denoted as R_{final}-$R_{initial}$), the center masses of SKOV-$3^{1.2kPa}$ grew nearly by 50μm, being significantly bigger than that of the SKOV-3^{90kPa} spheroids (Fig.3.10h).

However, the extent of invasion quantified with D_{tip} showed a reversed tendency. Though there were no notable differences during the first day (Fig.3.10i), the invasiveness increased with the priming stiffness from the second day (Fig.3.10j-l). In particular, the SKOV-3^{90kPa} spheroids still exceeded the others on Day 4 of the invasion assay, which is 6 days after the mechanical priming, proving the persistency of mechanical memory.

3.4 Discussion

Herein, we propose a comprehensive model describing how the mechanical memories in the ovarian cancer model arise, persist, and govern the metastatic potential during peritoneal metastasis. Ovarian cancer cells grow and adapt on the surface of the primary tumor with a heterogeneous distribution of mechanical properties. Most ovarian cancer metastases are known to arise from spheroids made of cells that had shed out together, maintaining cell-cell junctions [85]. Thus, it is plausible that the adjacent cells comprising a spheroid would have primed on comparable stiffness in a similar way that we artificially simulated *in vitro*. Cells matured on relatively compliant spots tend to develop high intercellular stresses resulting in cellular cohesiveness, while those on stiff spots demonstrate lower intercellular stresses, being more autonomous. Consequently, how the cells aggregate into malignant spheroids within the peritoneal cavity and the resultant architecture of the spheroids also become diverged. Soft-primed cells are more likely to develop actin cage structures during aggregation, likely due to the high cohesiveness of cells. Instead, the stiff primed spheroids feature unique lumen-like voids, whose causes and effects remain unknown. In addition, the stiff-primed spheroids would exceed the soft-primed spheroids in both spreading and invasion against the secondary lesion because they lack the actin cage structure barricading the cells (Fig.3.11).

We discovered that the alterations in the genes involved in cell adhesion were not primarily responsible for mechanical memory. Besides, genes related to the epigenetic regulation also had nothing to do with the priming stiffness, though they upregulated undergoing the hanging drop culture. The memory instead chose to be transferred in the form of disparities in spheroidal architectures, resulting in different invasiveness. The evolution of mechanical memory from the cellular scale to the spheroidal scale, parallel with the phases of the peritoneal metastasis, made it possible to reinforce and prolong mechanical memory. We regard the above insight as the most fruitful harvest of establishing the in vitro model with full consideration of the metastatic peritoneal route. It would not have been able to verify the persistence of the memory if we just focused on single cells or two-dimensional collective cells, as evidenced by the diminishing gaps between the stress maps of SKOV-3$^{1.2kPa/11kPa/90kPa}$ monolayers over time (Fig.3.2b-d). It may sound counterintuitive, but cells that have undergone the hanging drop culture could maintain their memory despite the multiple passaging and extreme environmental changes.

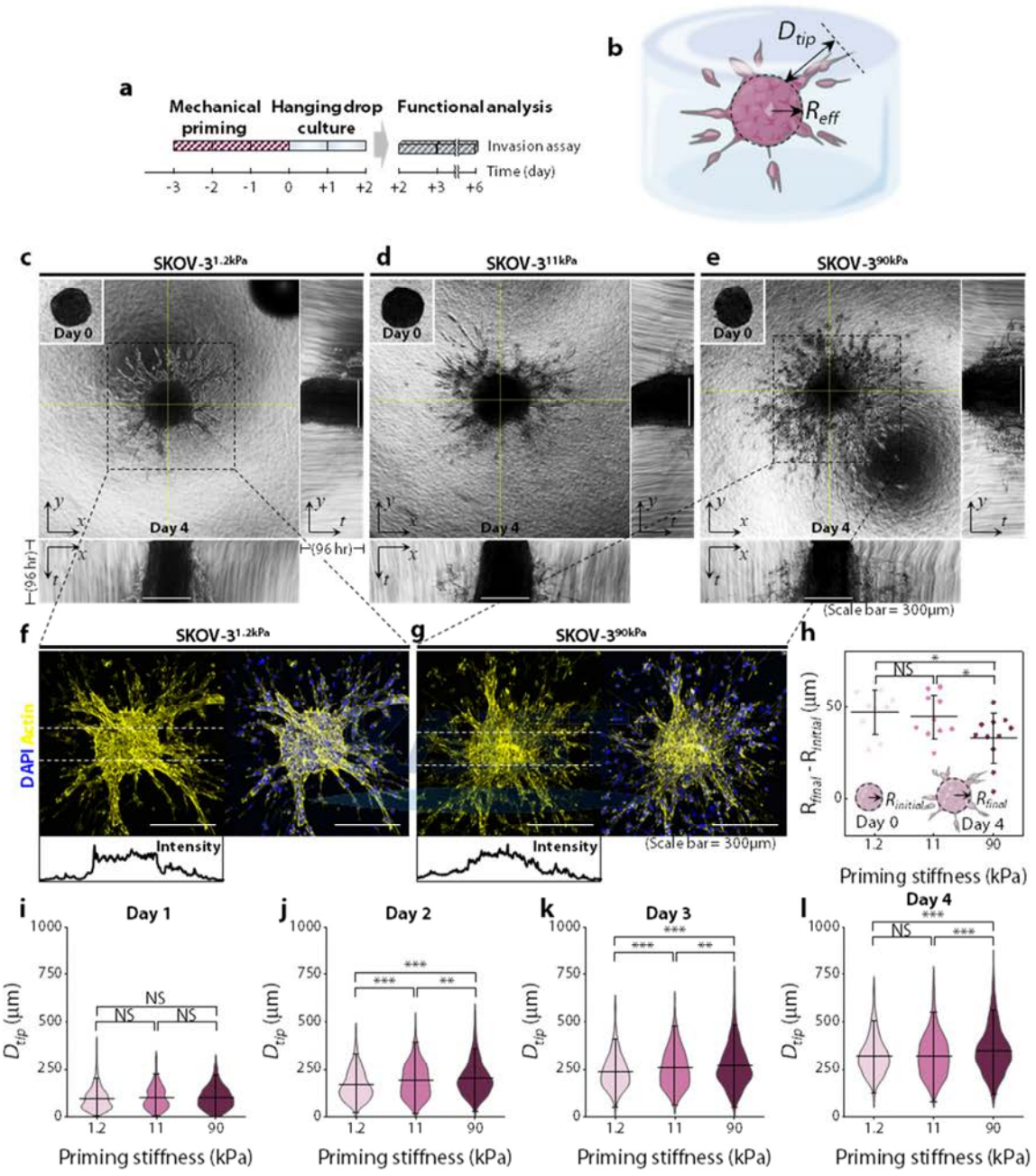

Figure 3.9 Invasion assays in collagen gel were conducted as a measurement of metastatic potential of hanging drop spheroids in the 3D microenvironment (a). The center masses' growths were quantified with the index of efficient radius, R_{eff}, and the extent to which the scattered cells infiltrated were quantified with the index of distance to the tip, D_{tip} (b). Over time, cells scattered from the SKOV-3^{90kPa} featured the longest D_{eff} (c-e, g-j). The growth of effective diameter showed decreasing trends with increasing priming stiffness. In summary, the SKOV-3$^{1.2kPa}$ invade less with more center mass growth while the SKOV-3^{90kPa} invade with less center mass growth. N=3, $n_{1.2kPa}$ = 11, n_{11kPa} = 10, n_{90kPa} = 11, n: number of spheroids. One-way ANOVA test with Tukey *post hoc*.

The actin cage structures deserve special attention. In line with the strong cell-cell interaction identified with the TFM, the actin cage also can account for the lagged spreading/invasion and excessive growth of center masses of soft-primed spheroids in functional assays. The actin cages along the spheroidal surfaces physically barricade the core cells expressing comparatively less actin, which would have hindered the breakaway of the cells. In contrast to the stiff-primed cells that could be released readily, the soft-primed cells would have been more advantageous in building the center mass by repeating cell division rather than escaping from the spheroids holding them firmly.

As well as the actin cage, the lumen-like void structure is another feature that varies according to the mechanical memory. According to the previous study published by Langthasa et al., the lumen-bearing spheroids are closer to the epithelial cells and have lower invasiveness compared to the spheroids without lumen [97], which is contradictory to our observation. Further research is required to determine whether the void structures described in the two papers are fundamentally distinct, or the suppressant effects of the voids are true but overridden by other factors enhancing the invasiveness.

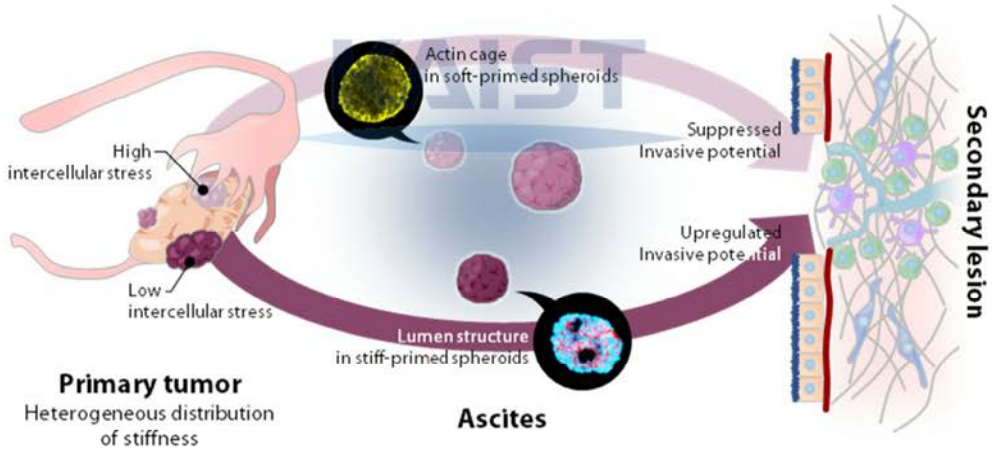

Figure 3.10 Suggested model of the mechanisms where the mechanical memory sustains in the route of peritoneal metastasis of ovarian cancer. The memories obtained from the heterogeneous distribution of stiffness on the primary tumor directly govern the level of intercellular stresses, and the differences later become engraved in the form of cytoskeletal structures in the spheroids. The divergence of the inner structure during the metastatic processes will result in the suppressed/upregulated metastatic potential when the spheroids arrive at the peritoneal membrane, the secondary lesion of most metastatic ovarian cancer.

In conclusion, the mechanical memories of ovarian cancer cells caused by prior exposure to heterogeneous stiffness levels will be maintained and transferred at the spheroid level, ultimately modulating the metastasis potentials onto the peritoneal membrane.

Chapter 4. Engineering breast cancer models with tuned invasion modalities[d]

4.1 Introduction

Over the last few decades, three-dimensional cancer spheroids have gained a reputation as a next-generation cancer model for being structurally similar to *in vivo* tumors. The structural similarity makes the spheroids imitate not only the appearance of the tumor but also the compositions of junctional proteins. In conventional 2D monolayer models, cell-substrate junctions are unusually prevalent compared to the actual tumors and spheroidal cancer models. Since the way a cell interacts with its surrounding environments, governed by the junction proteins, has profound influences on physiological events such as proliferation, differentiation, apoptosis, and migration, 2D monolayer models are insufficient for mimicking tumor pathology [99]. Another key feature of *in vivo* tumors that 2D monolayer models cannot and spheroids can replicate is the metabolic gradient spanning from the core to the periphery of the tumor (Fig.4.1). Unlike the normal cells, cancer cells pile up, sometimes putting themselves in tight spots that make it hard for molecules to get through. Furthermore, vasculatures around the tumor are leaky and have low transport efficiency [100]. Thus, cells near the stroma and vasculatures can be fed with sufficient oxygen and nutrients, while the cells at the core fall into hypoxia. Hypoxic conditions are known to accelerate cancer progression. Hypoxia-inducible factors stimulate the secretion of proteins that bring on angiogenesis, ECM realignment, and almost every stage of metastasis. The quiescence due to hypoxia incapacitates the chemo/radiotherapy. Considering these points, spheroidal cancer models are better *in vitro* models than 2D monolayers for unraveling the unknown mechanisms of cancer propagation Therefore, numerous methods for spheroid culture have been developed. However, it became more challenging for researchers to choose an optimal method as more and more options emerging. One tactic could be to select a protocol that best mimics the most lethal characteristics of cancer, which is the cancer invasion.

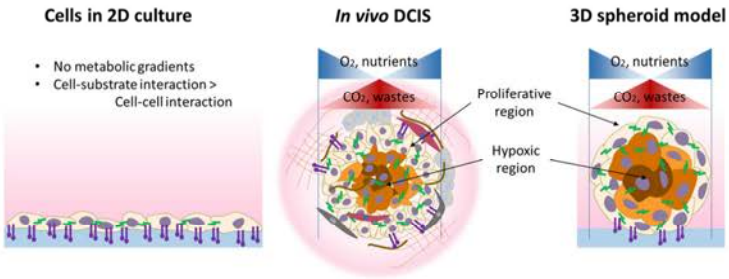

Figure 4.1 Comparisons between the cells in 2D culture, 3D spheroid model, and the *in vivo* DCIS

[d] Contents of this chapter is revised from the part of Master's thesis with a title of "Correlation between spheroidal phenotypes and functionality as cancer model (2018)", authored by Jiwon Kim.

Historically, the ‘single cell dissemination mode’ has been favored as a model of cancer invasion, where the single invasive cancer cells undergo EMT, acquire motile phenotypes, and get access to the circulatory system. However, more recent studies have shown that primary tumor invasion generally involves collective rather than single-cell migration modes.

Identifying the migration mode of cells in a living organism necessitates two prerequisites: High resolution sufficient to capture a single cell; three-dimensional image acquisition. Various non-invasive imaging techniques, including CT, MRI, and PET, allow the 3D reconstruction of multi-slice images. However, the resolutions of the radiologic images are on the millimeters scale, which is not enough to distinguish a solely migrating cell. On the other hand, images acquired from immunohistochemistry conducted after biopsy or surgery have adequate resolution, while these images cannot be reconstructed into 3D. Therefore, schematic presentations of cancer metastasis models published in the early 2010s mostly pre-assumed the single-cell migration mode.

However, substantial evidence in recent years indicates that invading tumor cells migrate in a collective modality. Although immunohistochemical images of single z-plane frequently show tumor buds that appear to be separated from the primary tumor, 3D reconstruction of these images revealed that the buds actually have out-of-slice links to the main tumor. Not a single individually scattered cell was detected in 15 human tumor samples taken from the pancreas, colon, lung, and breast [101]. Furthermore, the expression of membrane E-cadherin was preserved in more than 90% of invasive ductal carcinoma (IDC), indicating that they are likely to move while maintaining cell-cell contacts [102]. The presence of clustered circulating tumor cells also proves that cancer cells migrate collectively before the intravasation. Patients with CTC clusters had a much worse prognosis than those with only single CTCs, and CTC clusters had a 50-fold higher metastatic potential than single CTCs in orthotopic breast cancer mouse models [103]. The polyclonal metastases observed in patients and mouse models also refute the hypothesis of single-cell migration [104]. As these findings become more widely acknowledged, a revised metastasis model emphasizing collective migration was recently published [105]. Taken together, the *in vitro* cancer models, including the spheroidal cancer model, should reproduce the collective migration of the actual *in vivo* tumor.

Though there are hundreds of original protocols for spheroid generation and their optimized versions, most of them can be categorized into the scaffold-free or scaffold-based method [106-108]. In this study, we adopted the most commonly used scaffold-free and scaffold-based methods for generality: Liquid overlay technique using Ultra-Low Attachment surface and pseudo-3D culture using reconstituted basement membrane (Matrigel). The two kinds of cancer models were comparatively analyzed through *in vitro* invasion assay. Here, we observed significant differences between those two models, including the migration modality. We observed that the Matrigel-based model is better suitable for modeling cancer invasion than those created with ULA plates since it consistently demonstrated collective modality and stronger contractility against the surrounding ECM fibers in various concentrations of collagen gel.

4.2 Materials and Methods

4.2.1 Cell maintenance

Human breast adenocarcinoma cell line, MDA-MB-231, was purchased from ATCC. This cell line was maintained in Dulbecco's Modified Eagle's Medium (DMEM; WELGENE) supplemented with 10% heat-inactivated fetal bovine serum (Gibco) and 1% penicillin/streptomycin (Gibco). The cell line was kept at the standard condition of 37°C and 5% CO_2 concentration. Cell culture and 3D cellular spheroid generation were performed when the confluency reached approximately 80%.

4.2.2 Scaffold-free method

Ultra-Low attachment (ULA) plates with a diameter of 60mm were purchased from Corning. Cells were trypsinized and suspended at the concentration of $10e^4$ cells/ml. 6ml of cell suspension was replated in the ULA plate. The plates were handled with extreme care since unnecessary agitation during spheroid growth can form a small number of extremely large cellular aggregates. This is undesirable because it lowers the homogeneity of the spheroid and causes many necrotic cells, leading to inconsistent results. The culture media was resupplied every two days.

4.2.3 Scaffold-based method

Growth Factor Reduced Matrigel Matrix was thawed and applied to the substrate of glass bottom dishes immediately before the matrix solidified. When the surface was covered completely and evenly with Matrigel, the dish was incubated for 30 minutes in the incubator. While the plates were being incubated, cells were trypsinized and resuspended in fresh medium. This cell suspension was diluted in 1ml of pre-warmed culture medium. Then, the same volume of chilled culture medium containing 4% of Matrigel was added to the cell suspension to make the total concentration of Matrigel 2%. The final mixture was placed on the dish covered with solidified Matrigel. The culture medium containing 2% Matrigel was resupplied every two days.

4.2.4 Invasion assay

Collagen gel precursor with 2.0mg/ml and 2.9mg/ml concentration was prepared by diluting ice-cold collagen type I (CORNING, 354236) extracted from rat tail with autoclaved di-water and 10× PBS of a volume corresponding to 1/10 of the total volume. A few drops of 0.5M NaOH were added to adjust the pH level to 6.8~7.2. All mixing procedure was done swiftly in an ice tray to prevent untimely solidification, resulting in heterogeneity in the gel. Harvested spheroids were embedded in the collagen gel precursor. The dishes containing the precursor and spheroids were flipped over and over to prevent the sedimentation of spheroids. The spheroid-embedded collagen gel completely solidified after 45 minutes in the incubator. Once the collagen gels had become translucent, they were mounted on a microscope with incubating system and imaged once an hour.

4.2.5 Measurement of displacement and velocity of cells

Phase images of invading spheroids were binarized with ImageJ. The projected area and perimeter of the binarized images were measured again using ImageJ. The speed and displacement of invading spheroids at $t = i$ were calculated as shown in Fig.4.4a. For example, if the projected area of a spheroid increased by 1,515μm^2 in the 9~10th hour and the perimeter of the spheroid at the 9th hour is 901μm, the invasion speed is 0.028 μm/min.

4.2.6 PIV for quantifying the contractility of spheroids against the collagen fibers

The contractility of spheroids against the collagen fibers was quantified with the radial component of collagen velocity. The velocities in Cartesian coordinates of each node around the spheroids were calculated with PIVlab, a PIV software available with MATLAB. The velocity vectors at every grid point were dot-producted with the unit vector coming out from the centroid of the center mass to measure the contractility.

4.3 Results

4.3.1 ULA and Matrigel spheroids exhibit distinct morphological characteristics

ULA spheroids and Matrigel spheroids look significantly different even though they are made of the same cell line. Previously, Kenny *et al.* categorized cancer spheroids into four groups based on their morphological phenotype: Round, mass, grape-like, and stellate [109]. According to this categorization, the ULA spheroid falls into the grape-like group, where the cell-cell adhesions are very weak, and the arrangements of nuclei are disorganized (Fig.4.2a). The ULA spheroids required to be gently handled; otherwise, they easily got crumbled. However, the Matrigel spheroids belong to the mass group where the cell-cell adhesions are more robust (Fig.4.2b). The sizes of the spheroid quantified with the projected area were significantly larger in the ULA spheroids than the Matrigel spheroids, which is likely due to the convection flows in ULA plates enabling the smaller aggregations to bump and fuse with each other (Supplementary Video 4.1). The Matrigel spheroids were bound to the substrate, having lower chances of getting closer to the neighboring cells (Fig.4.2c). Instead, they grew steadily rotating, resulting in higher circularity (Fig.4.2d, Supplementary Video 4.2).

qPCR results showed that mRNA expression levels of Integrin β1 were similar in both spheroids, which is interesting because the ULA spheroids could not form any cell-substrate junctions (Supplementary Video 4.1). However, E-cadherin was expressed significantly higher in the Matrigel spheroids than in the ULA spheroids, as inferred from the compact morphologies (Fig.4.2e). According to the result and since E-cadherin is in charge of intercellular connections, it is plausible to expect that the Matrigel spheroids have more chance to migrate in a collective way than the ULA spheroids.

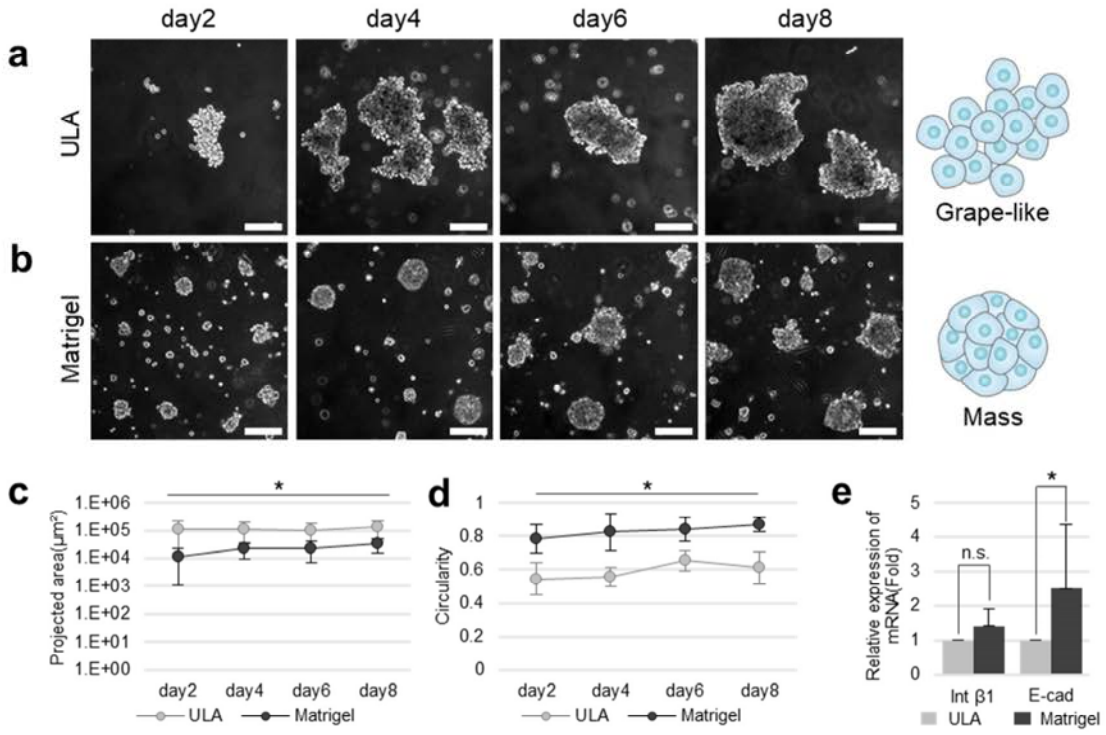

Figure 4.2 Morphological characterization of cancer models fabricated with ULA or Matrigel. The spheroids made with ULA are classified to grape-like group (**a**), which have disorganized nuclei and low integrity (Kenny *et al*. 2007). On the other hand, the MCSs made with Matrigel are classified into mass group (**b**), which also have disorganized nuclei, but have robust cell-cell adhesions. Projected areas of MCS made with ULA were significantly higher in every time point (**c**), since the convection flow makes higher chances for small cell aggregates to bump into each other. However, the circularity was higher in the MCSs made with Matrigel, as they have robust cell-cell junctions (**d**). The qPCR results showed that the spheroids made with Matrigel have significantly higher expression of E-cadherin.

4.3.2 Matrigel spheroids migrate collectively while the ULA spheroids scattered individually

Next, the two groups of spheroids were tested for their invasiveness in 3D collagen gel. The spheroids were embedded in collagen gel with concentrations of 2.0 or 2.9 mg/ml and observed for 15 hours (Fig.4.3a). At the 12th hour, the ULA spheroids had ten times as many single cells scattered from the center mass as the Matrigel spheroids (Fig.4.3b), proving that they migrate individually rather than collectively. In 2.0 mg/ml collagen gel, the ULA spheroids showed elongated frontal processes from the very beginning of the invasion assay. As time passed, the cells got released from the center mass and migrated freely, with some of them featuring mesenchymal-like bipolar phenotype and others showing amoeboid-like phenotype (Fig.4.3c). On the other hand, the cells coming out of the Matrigel spheroids sustained intercellular junctions and developed collective strands penetrating the surroundings.

4.3.3 Matrigel spheroids sustain their thrusts in a dense matrix

Next, invading speeds and displacements of ULA and Matrigel spheroids were quantified as described in Fig.4.4a. The ULA spheroid migrated particularly fast in 2.0 mg/ml gel in terms of averaged speed and displacement. However, when the spheroids were embedded in 2.9 mg/ml collagen gel, both the speed and

displacement were significantly lowered compared to when in the 2.0 mg/ml gel (Fig.4.4b, d). Particularly, the difference in speed depending on the gel conditions became considerable 3 hours after the beginning of the invasion assay, most likely because the single cells began to separate from the center mass at this time, resulting in dramatic alterations to the projected area (Fig.4.4b, d).

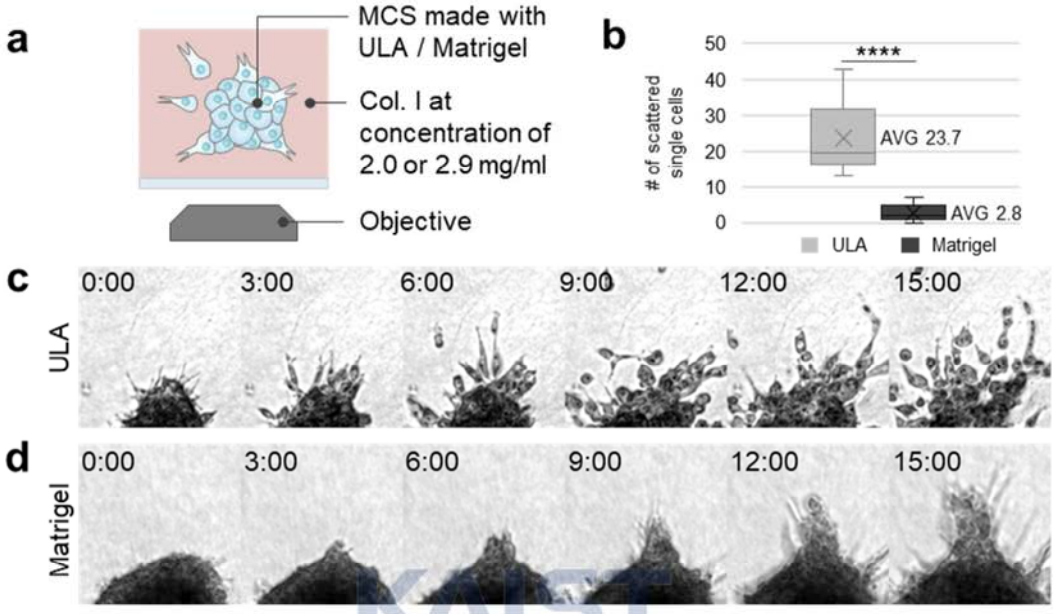

Figure 4.3 Migration modes of cancer models fabricated with ULA or Matrigel. The experimental setup of invasion assay (**a**). The spheroids grown for 4 days in ULA plate or Matrigel were transplanted to collagen I matrices with concentrations of 2.0 or 2.9 mg/ml. In 12 hours, an average of 23.7 cells were isolated from the center mass of ULA spheroids and migrated in single-cell migration mode, while only 2.8 cells from the Matrigel spheroid did the same (**b**). The time-lapse images captured in the invasion assay show that each model has quite different migration modes. The cells located at the periphery of the ULA spheroids showed an obvious single-cell migration mode (**c**). Meanwhile, the cells from the Matrigel spheroids sustained the cell-cell junction while they migrated (**d**).

However, in the case of the Matrigel spheroids, they move almost the same regardless of the collagen concentration. Though the ULA spheroids' speed and displacement were dramatically reduced in high-concentration collagen at all time points, the Matrigel spheroids, despite not being very fast in the 2.0 mg/ml collagen gel, do not lose their motility in a denser matrix (Fig.4.4c, e).

4.3.4 Matrigel-based spheroids exert higher contractility against the surrounding ECMs

Adjusting the contrasts of the images, we could track how the collagen fibers surrounding the spheroids get remodeled using the PIV. We defined the contractility against the surrounding ECMs by the radial components of collagen velocity at every grid point, as shown in Fig.4.5a. When the radial component is negative, it means that the collagen at the point is being drawn toward the center mass, whereas the positive radial component means that the collagen is being pushed outward.

Interestingly, the scattering cells coming out from the ULA spheroids just went through the matrix without deforming the collagen fibers (Fig.4.5b, Supplementary Video 4.3), suggesting that those scattering cells would mainly employ the amoeboid-like migratory phenotype.

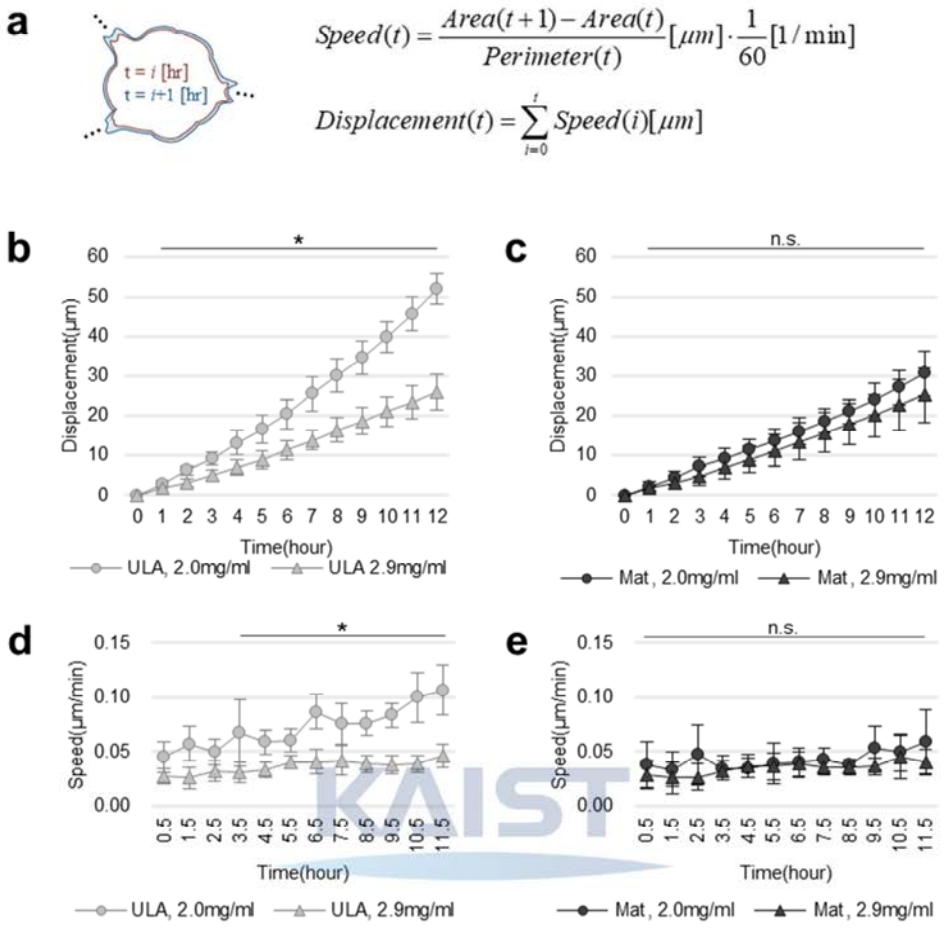

Figure 4.4 Displacement and speed of ULA or Matrigel spheroids. The definition of displacement and speed of cells from MCSs in the invasion assay. To cancel out the inconsistency due to the initial size of spheroids, the displacements were calculated by dividing the area propagated during the unit time by the perimeter of the spheroids at the beginning of the unit time. The speed was in the unit of μm/min (**a**). The spheroids made with ULA moved significantly less distance in collagen matrix of 2.9mg/ml than in collagen of 2.9mg/ml (**b**). However, there were no significant difference between the spheroids seeded in 2.0mg/ml collagen and 2.9mg/ml collagen (**c**). In the case of the spheroids made with ULA, the difference between the speed in the 2.0mg/ml matrix and that in the 2.9mg/ml matrix widened within 4 hours from the onset of the invasion assay (**d**). However, there were barely no difference between the 2 cases of MCSs made with Matrigel (**e**).

However, the Matrigel spheroids strongly pull the surrounding collagen fibers while they collectively migrate (Supplementary Video 4.4). The pulled collagen fibers were highly aligned in radial directions, and this alignment is reminiscent of the tumor-associated collagen signature-3 (TACS-3) which is found near highly invasive *in vivo* tumors. It is known that the actual tumor cells use the aligned collagen fibers as their track to invade neighboring vasculatures. The magnitude of contractility against the ECM turned out to be much larger around the Matrigel spheroids than around the ULA spheroids (Fig.4.5c). The contractility plot shows that the Matrigel spheroids exert significant tractions on the surroundings, but also there are many positive peaks near the spheroid surfaces. These peaks show the tips of cellular strands migrating outward.

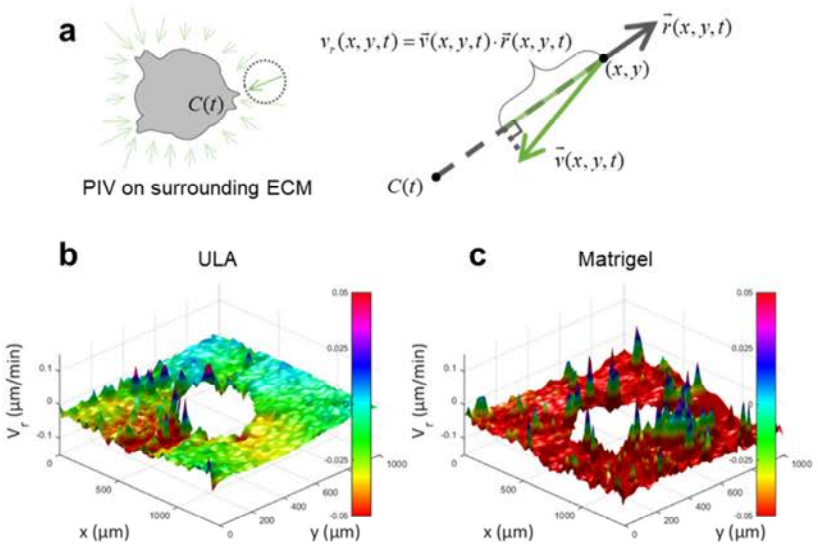

Figure 4.5 Contractility against the surrounding ECM fibers of ULA or Matrigel spheroids. The radial components of collagen velocity is defined as the contractility of each spheroid against the surrounding fibers (**a**). ECM fibers near the ULA spheroids remained hardly affected by the cellular invasion (**b**). On the other hand, the ECM fibers around the MCS made with Matrigel were dragged toward the centroid of the spheroid. The maximum speed of dragged fibers were 6.4 μm/hour, about three times than the speed of propagating cells (2.1μm/hour) (**c**).

4.4 Discussion

As the idea that the 3D-spheroidal cancer models can recapitulate *in vivo* tumors are now widespread, a considerable number of protocols to generate spheroids have been developed. Therefore, standards for choosing an optimal protocol are of growing interest. Here, we focused on the collective migratory modes of cancer cells which are observed commonly in *in vivo* tumors. We took this collectiveness as a new criterion for selecting the cancer models and tried it on two representative protocols for generating spheroids – Liquid overlay technique using Ultra-Low Attachment (ULA) surfaces and pseudo-3D culture using reconstituted basement membrane (Matrigel). MDA-MB-231, a triple-negative breast cancer cell line, exhibited totally distinct phenotypes depending on how they aggregated into spheroids. The results of the invasion assay revealed that the cells from the Matrigel spheroids collectively migrated, sustaining the cell-cell interactions, while the cells from the ULA spheroids scattered and moved individually. 12 hours after the initiation of the invasion assay, 10 times more single cells were found around the spheroids made with ULA than around the spheroids made with Matrigel. Furthermore, the cells from Matrigel spheroids sustained their velocity in 3-D collagen gel regardless of the collagen concentration (2.0 or 2.9 mg/ml), while their counterparts from ULA spheroids significantly get slowed in high-concentration collagen. Matrigel spheroids also could easily remodel and align their surrounding collagen fibers to transform them into TACS3-like arrangements. In conclusion, we suggest the Matrigel-based pseudo-3D culture as the appropriate protocol for generating a physiologically relevant cancer model and also propose criteria for evaluating spheroid generation protocols.

Chapter 5. Microtubule mechanics contributing invasion of glioblastoma model[e]

5.1 Background

Glioblastoma is an incurable disease whose invasion mechanisms are poorly understood. Many solid cancers originate from the epithelial cells and undergo EMT to acquire motile phenotypes, but in the case of GBM, they already originated from the mesenchymal cells, ruling out EMT as a feasible explanation for GBM invasion. To investigate the molecular mechanisms of GBM invaison, mouse GBM models expressing *EGFRviii* were established with CRISPR/Cas9, and single-cell RNA seq was conducted. As a result, platelet-derived growth factor receptor (PDGFR) and tyrosine-protein kinase Fyn were suspected of being major key regulator genes of the GBM invasion (Fig5.1). PDGFR is observed to be overexpressed and activated in most GBM cases; Fyn is also overexpressed in human glioma and is known to limit cellular motility when genetically silenced.

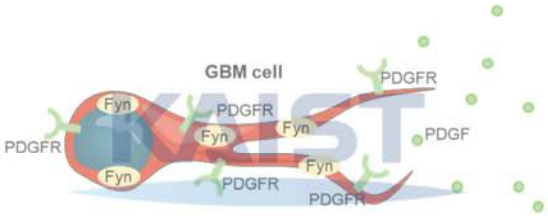

Figure 5.1 Schematic presentation of a GBM cell expressing PDGFR and Fyn, which are potential regulators of GBM invasion.

To interrogate how the GBM cells migrate with or without the target genes, a *in vitro* model mimicking the GBM invasion became necessitated. The *in vivo* mouse model could be examined with intravital imaging or even expansion microscopy. However, the intravital imaging could not capture migrations at the cellular level, though they allowed tracking of invasion trends while the mice were alive (Fig.5.2a). With expansion microscopy, the whole tumor landscape could be reconstructed with a subcellular-level resolution, but it could not capture the temporal progression of GBM (Fig.5.2b). Moreover, the factors like PDGF can be synthesized in neurons, neuronal progenitors, astrocytes, and oligodendrocytes, making the *in vivo* model not suitable for the mechanisms study requiring a controlled environment. Thus, in this study, we established an *in vitro* GBM spheroid model where we can capture the temporal progressions with high resolution in a controlled environment. With the established spheroid model, we comparatively analyzed

[e] Contents of this chapter are extracted from a manuscript in preparation with a title of "Fyn kinase-dependent saltatory migration in white matter invasion of glioblastoma", authored by Haemin Chon[§], Jiwon Kim[§], Joon-Goon Kim[§], Eunyoung Park, Eunhyeong Lee, Jeong Ho Lee, Taeyun Ku[*], Jennifer H Shin[*], and Injune Kim[*] (§ Equal distribution).

how the wild-type GBM cells from spheroids invade when deprived of PDGF-AA, knocked down Fyn, or both. Subsequently, we also studied the roles of cytoskeletal remodeling using drug assays.

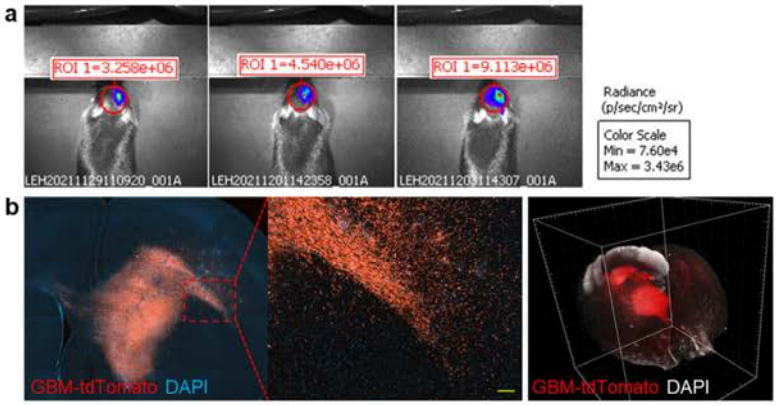

Figure 5.2 tdTomato-expressing GBM cells observed with intravital imaging (a)[f] and expansion microscopy (b)[g].

5.2 Materials and Methods

5.2.1 Single-cell dissociation and fluorescence-activated cell sorting[h]

Mice bearing tdTomato-expressing GBM were, after anesthesia, perfused transcardially with 20 ml of pre-chilled (4 °C) PBS. Brains were harvested, and then specific regions or whole tumor mass were dissected carefully under the fluorescence stereo-microscope (AxioZoom V16, Carl Zeiss). After chopping tissues with a razor blade, collagenase IA (100 U/ml) (C2674-1G, Sigma) was added and incubated for 20 min in a 37 °C water bath to disrupt cell-cell adhesion. Enzymatically digested tissues were triturated using a 200-μl pipette tip for mechanical dissociation, and cell suspension was passed through a 40 μm cell strainer. After lysing red blood cells with 0.8% ammonium chloride (07850, Stem Cell Technologies), single-cell suspension was immunostained with DAPI (1:10,000; Invitrogen) and an anti-CD45 antibody conjugated with APC-Cy7 (1:1,000; 557659, BD Pharmingen). DAPI-negative, CD45-negative, and tdTomato-expressing GBM cells were fractionated using BD FACS Aria II (BD Bioscience) or Moflo Astrios EQ (Beckman coulter). Isolated GBM cells were used for scRNA-seq or 3D GBM spheroid formation.

5.2.2 *In vitro* 3D invasion assay using GBM spheroids

For generating GBM spheroids, we used flat bottom 96-well plates with an ultra-low attachment property. Fractionated GBM cells by FACS sorting were seeded at a density of 30,000 cells per well in DMEM supplemented by 10% heat-inactivated FBS and 1% penicillin/streptomycin. After 96 hours of suspension culture, formed GBM spheroids were collected and washed with PBS. Collagen gel precursor (1.0 mg/ml)

[f] Courtesy of Dr. Haemin Chon
[g] Courtesy of Joon-Goon Kim
[h] Courtesy of Dr. Haemin Chon

was prepared with rat tail collagen type 1 (Advanced Biomatrix), 10× PBS, and distilled water on an ice bucket to prevent untimely solidification. A few drops of sodium hydroxide were added to adjust the solution pH to 7.0–7.4. Adjusted collagen precursors were pipetted into a 96-well plate prechilled on an ice block. Before the precursor polymerizes, harvested 3D GBM spheroids were quickly embedded in each well one by one. Collagen gel precursors embedded with the spheroids were incubated for 45 min. After incubation, each polymerized collagen gel containing the spheroids was submerged with designated media: a neurobasal medium (hereafter NBM, Gibco) and NBM supplemented with recombinant PDGF-AA (SRP-3228, Sigma). The migration of individual cells scattered from the center mass was tracked for 48 h by live-cell imaging with a time interval of 1 h. Live-cell imaging was performed with an epi-fluorescence microscope (Carl Zeiss) equipped with a lab-made microscope mountable incubator that consistently adjusts the temperature and CO_2 level to 37 °C and 5%, respectively.

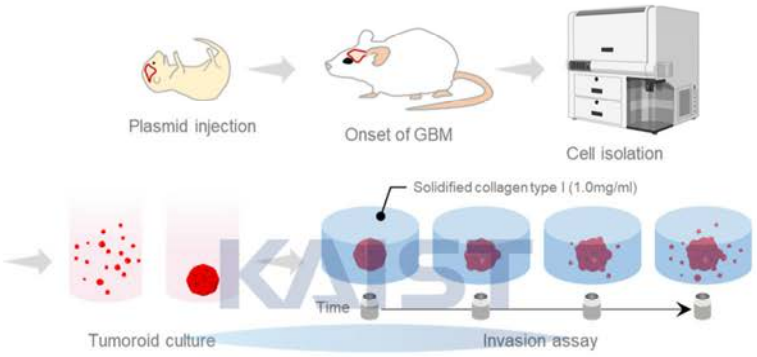

Figure 5.3 Experimental setup of GBM invasion assay. Mouse models bearing spontaneous GBM were sacrificed, and the viable GBM cells were isolated using fluorescence-activated cell sorting (FACS).

5.2.3 Pharmacological inhibition of microtubule remodeling

The effect of microtubule inhibition was also examined with the 3D invasion assay of GBM spheroids. Paclitaxel and nocodazole (Sigma) were dissolved to the stock concentrations of 5.86 mM and 3.32 mM in dimethyl sulfoxide, respectively, and stored at −20 °C until use. Those drugs were diluted to the final concentration of 500 nM in NBM supplemented with recombinant PDGF-AA. Collagen gel blocks embedded with the GBM spheroids were submerged with media containing each inhibitor or vehicle. Spheroids were longitudinally visualized for 48 hours with a time interval of 1 hour.

5.2.4 Bulk RNA-seq and data analysis[i]

Total RNA was purified from fractionated cancer cells from three control GBMs and four ΔFyn GBMs were dissolved using Qiazol Lysis Reagent (79306, Qiagen Sciences) and RNeasy mini plus kit (74134, Qiagen Sciences). The libraries were sequenced on an Illumina NextSeq500 sequencer by the eBiogen.

[i] Courtesy of Dr. Haemin Chon

QuantSeq 3′mRNA-seq reads were aligned to the mouse reference genome (mm10) using TopHat2. The number of reads, which were aligned to the 1,000 bp of 3′ end of each gene, was counted by Bedtools. A DESeq2 package was used to normalize read counts and extract DEGs under R 4.0 and RStudio 1.1.463. Significant DEGs were defined as $P < 0.05$ and an absolute $\log_2$ fold change > 2. GOs were analyzed using Enrichr (http:/maayanlab.cloud/Enrichr). Gene set enrichment analysis was done using GSEA v4.1.0 (Broad Institute).

5.3 Results

5.3.1 Flat bottom ULA plate yields primary GBM spheroids in a consistent manner

First of all, we tried four protocols for GBM spheroid generation; Poly-D-Lysine (control), Matrigel pseudo-3D culture, pCHMA plate, and ULA plate. However, GBM cells cultured with Poly-D-Lysine and Matrigel conditions did not make it to the spheroids (Fig.5.4a, b). Fortunately, the pCHMA and ULA plates succeeded produce GBM spheroids. However, the pCHMA surfaces selectively grabbed a certain subpopulation of GBM cells. It is known that the pCHMA surfaces selectively grabbed the glial cells among the brain cells (Fig. 5.4)[110]. Considering that the GBM cells have heterogeneous populations, we decided to choose the ULA method not to exclude any of the GBM subpopulations. The flat bottom ULA plate yielded GBM spheroids with an average diameter of around 35μmOn the flat bottom ULA plate, only living cells aggregated, but on the round bottom dish, the gravity forced the dead cells to be mixed within the spheroids, deteriorating the viability of the whole spheroid (data not shown). Therefore, we chose the flat-bottom ULA plates over the round-bottom ones.

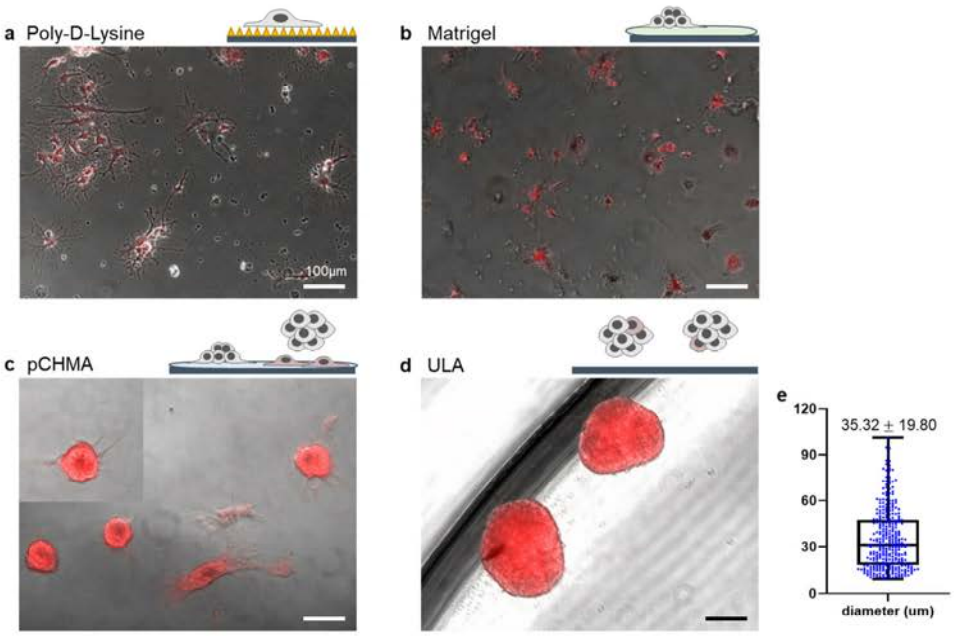

Figure 5.4 GBM spheroids generated with various protocols.[j] GBM cells could not aggregate into spheroids in Poly-D-Lysine and Matrigel conditions (a, b). GBM cells succeeded in forming spheroids, but pCHMA surfaces grabbed some of the cell population (c). GBM cells formed into spheroids with an averaged diameter of 35μm in flat bottom ULA plates (d,e).

5.3.2 PDGF induces process elongation at the front, while Fyn kinase induces rear retraction of GBM cells

As the *in vitro* GBM spheroids were established, we performed the invasion assays to investigate the role of PDGF and Fyn in GBM invasion. To simulate the very compliant environment of the brain, collagen gel with the concentration of 1mg/ml collagen was chosen since it was practically the lowest concentration that could be handled. Spheroids made of Wild-type cells and ΔFyn cells were tested with or without the PDGF-AA supplement.

Invading cells from the WT spheroids that were supplemented with PDGF exhibited long frontal processes and disseminated readily from the center mass. However, cells coming out from the ΔFyn spheroids could not separate from the center mass, though they were supplemented with the PDGF-AA. On the other hand, when the WT spheroids were deprived of the PDGF-AA, they could not develop the frontal processes, though they disseminated easily. Finally, when the cells were deprived of both Fyn and PDGF, they could not disseminate nor make frontal processes (Fig.5.5a, Supplementary Video 5.1). Therefore, we concluded that the Fyn kinase was responsible for the rear retraction while the PDGF was responsible for the process elongation at the front.

5.3.3 GBM cells with both PDGF and Fyn kinase feature saltatory migratory phenotype

Next, we extracted the cellular trajectories. Wild-type cells invaded more vigorously than ΔFyn cells, and when PDGF-AA was added, they invaded even more vigorously. Intriguingly, the WT cells often jumped very far in a short time, as shown with the long line segments in the trajectory plots (Fig.5.5b). In fact, this motion, also known as saltatory migration, is a migratory pattern observed during the developmental stage of oligodendrocytes. Saltatory migration features alternating fast-moving and stationary periods accompanied by dramatic changes in cell shape. Regardless of the PDGF-AA supplements, the WT GBM cells featured the distinguishing velocity trend, which is dramatically alternating (Fig.5.5c).

By definition, a cell undergoing saltatory migration also undergoes drastic changes in cellular morphology. When we zoom in on the migrating cells, we could find that cells supplemented with PDGF-AA deformed actively, whether the Fyn kinase is knock-downed or not. Besides, the magnified FOVs of GBM migration emphasize that the ΔFyn cells are having trouble getting separated from the center mass. Especially, the PDGF-supplemented ΔFyn cell underwent abnormal elongation, resulting in a cell length of more than 200 μm, yet it still failed to retract the rear part and be released from the center mass even after 48 hours. This case implies the dominance of Fyn kinase on the migratory phenotypes of GBM cells (Fig.5.5d,

[j] Experiment with Dr. Eunyoung Park (Fig.5.4), Analysis of Dr. Eunyoung Park (Fig.5.4e).

Supplementary Video 5.2). Overall, GBM cells having both Fyn and PDGF can reproduce two prerequisites of saltatory migration *in vitro*.

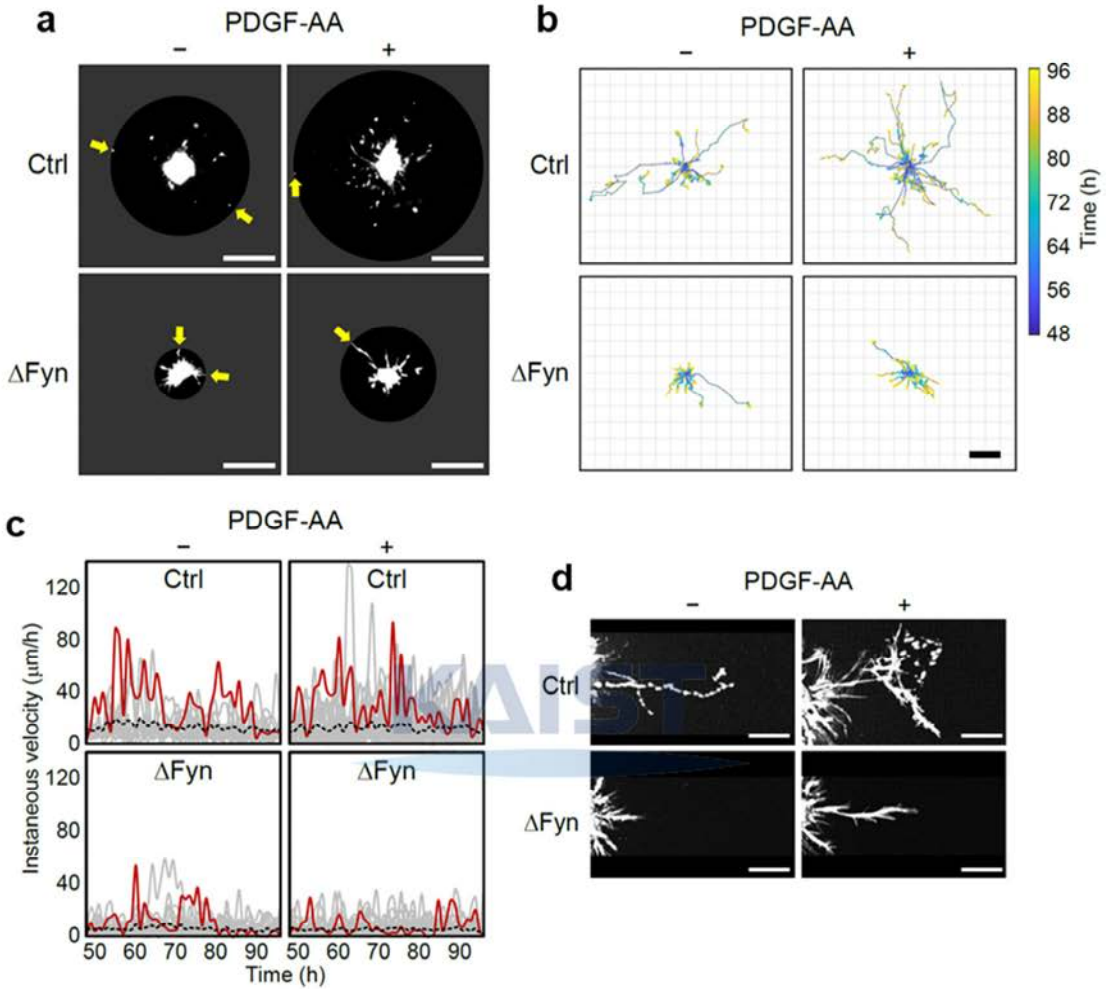

Figure 5.5 Fyn and PDGF-A signaling are necessary for dynamic migration of GBM cells in 3D gels. a Snapshots of Ctrl and ΔFyn GBM spheres at 96 h after embedding, displaying Fyn- and PDGF-AA-dependent spreading of GBM cells. Arrows indicate the most distant cells from the center mass. Scale bars, 500 μm. **b** Trajectory plots of migrating cells, showing faster and persistent migration of Ctrl GBM cells with PDGF-AA. Scale bar, 200 μm. **c** Time-lapse recordings of instantaneous velocity of migrating GBM cells. Red lines marking representative cells for each condition. Black dashed lines showing average velocities at each timepoint. Control GBM cells without PDGF-AA (n = 17 cells from 4 spheroids) and with PDGF-AA (n = 28 cells from 3 spheroids); ΔFyn GBM cells without PDGF-AA (n = 24 cells from 5 spheroids) and with PDGF-AA (n = 30 cells from 4 spheroids) were analyzed. **d** Overlaid time projections of spreading behavior in GBM spheroids from 48 to 96 h after embedding. Scale bars, 100 μm.

5.3.4 Microtubule dynamics are involved in GBM invasion

Bulk NGS analysis revealed another differentiating feature between the WT and ΔFyn GBM cells (Fig.5.6a). The results show that the WT GBM cells are more enriched with the gene related to the microtubules (Fig.5.6b, c). According to this data, the microtubule was presumed to be the most important cytoskeleton regulating the GBM invasion among the three types of cytoskeletons. By pharmacologically modifying the dynamic instability of microtubules, it was examined whether or not microtubules were involved in

saltatory migration. Thus, in the presence of PDGF, WT GBM cells were treated with nocodazole, which depolymerizes the microtubule, or paclitaxel, which stabilizes the microtubule.

Interestingly, cells invaded better when treated with nocodazole than treated with paclitaxel. GBM cells treated with paclitaxel seemed to lose most of their motility (Fig.5.6d, Supplementary Video 5.3). When we zoom in on the migrating cells again, these results are reminiscent of the previous results in Fig.5.5d (Fig.5.6e, Supplementary Video 5.4). WT cells treated with the nocodazole migrate the same as those being deprived of the PDGF in Fig.5.5d, even though they were supplemented with the PDGF-AA. The result implies that the nocodazole cancels out the effect of PDGF. WT cells treated with the paclitaxel migrate the same as the ΔFyn cells, implying that paclitaxel acts on the GBM cells like Fyn deletion. Together, these results show that PDGF is accountable for microtubule polymerization, whereas Fyn is accountable for microtubule dynamics, as summarized in Fig.5.7.

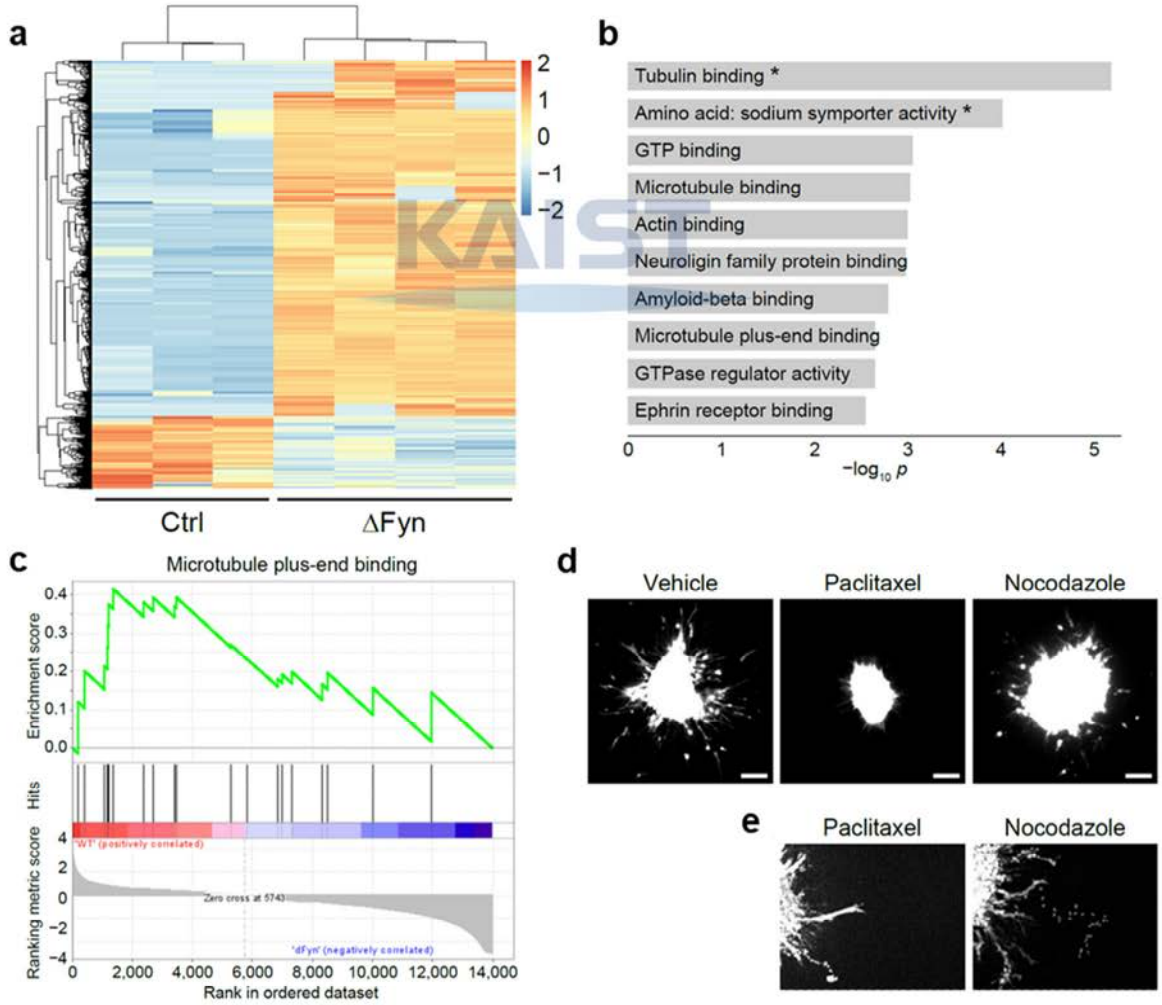

Figure 5.6 Microtubule remodeling fine-tune distinct steps of saltatory 1 GBM migration. a[k] Unsupervised clustering of differentially expressed genes in Ctrl (n = 3) and ΔFyn GBMs (n = 4). **b**[l] Gene ontology (GO) term analysis in molecular function (GO Molecular Function 2021) with differentially expressed genes upregulated in Ctrl GBM. *adjusted $p < 0.05$. Note the regulations associated with 5 microtubule remodeling ranked at the top. **c**[m] The gene set associated with microtubule plus-end binding enriched in Ctrl GBM (normalized enrichment score = 1.4870, p = 0.0638, FDR q = 0.2405). **d** Fluorescence images of tdTomato-expressing control GBM spheres at 48 h after embedding in the presence of vehicle, paclitaxel, or nocodazole. **e** Time projections of Ctrl GBM spheres (upper) and typical single migrating cells (lower) from 48 to 96 h after embedding in the presence of paclitaxel or nocodazole.

5.3.5 Classification of GBM cells by migratory phenotypes

More microscopic observations on the individual cells gave another insight into the GBM dynamics. Recently, it was found that the GBM cells employ similar migratory mechanisms with the neuronal progenitor cells undergoing their developmental processes, namely the branching migration, locomotion, and translocation [111]. In branching migration, the cells branch out the tumor microtubes (TMs) and proceed, alternating protrusion and retraction. Cells employing the locomotion mechanism mostly use uni-process leading the whole soma. Lastly, translocation took place with the TM anchored in one place and the soma being drawn in the direction, making the TM shorter (Fig.5.8a).

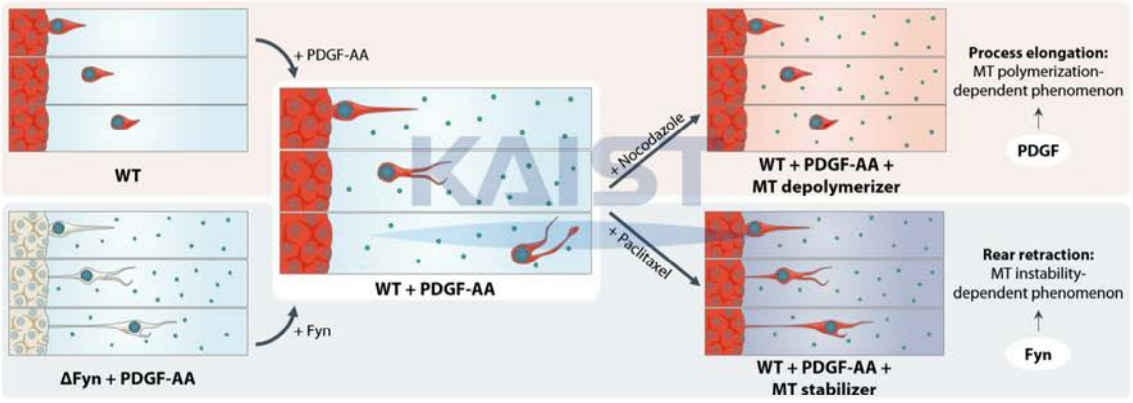

Figure 5.7 Schematic showing the severely suppressed migration by paclitaxel and impaired forward cell protrusion by nocodazole.

These three migratory phenotypes were replicated in our data (Fig.5.8b-d), and we also identified a fourth migratory mode, which we termed the amoeboid-like phenotype, adopted by aggressively invading GBM cells. These cells migrated far more rapidly than those that utilized the other three mechanisms and traveled in random directions while experiencing dramatic morphological alterations (Fig.5.8e, Supplementary Video 5.5). The trajectory graphic demonstrates that the cell traverses significantly larger regions within 48 hours (Fig.5.8f). When the cells were deprived of PDGF from the culture media or knocked out of the Fyn expressions, the cells exhibited defective migratory modes, especially in the case of ΔFyn (Fig.5.8g). Angular change of soma over time plot also shows the distinctive characteristic of amoeboid-like migration (Fig.5.8h-j). The value of 90° in these graphs indicates that the cell continues to advance in the radial

[k] Courtesy of Dr. Haemin Chon
[l] Courtesy of Dr. Haemin Chon
[m] Courtesy of Dr. Haemin Chon

direction, like in the case of locomotion. The amoeboid-like migration was accompanied by a series of sharp changes in soma angle (Fig.5.8j), implying that those cells are particularly good at exploring and infiltrating their surroundings among cells with other migratory phenotypes.

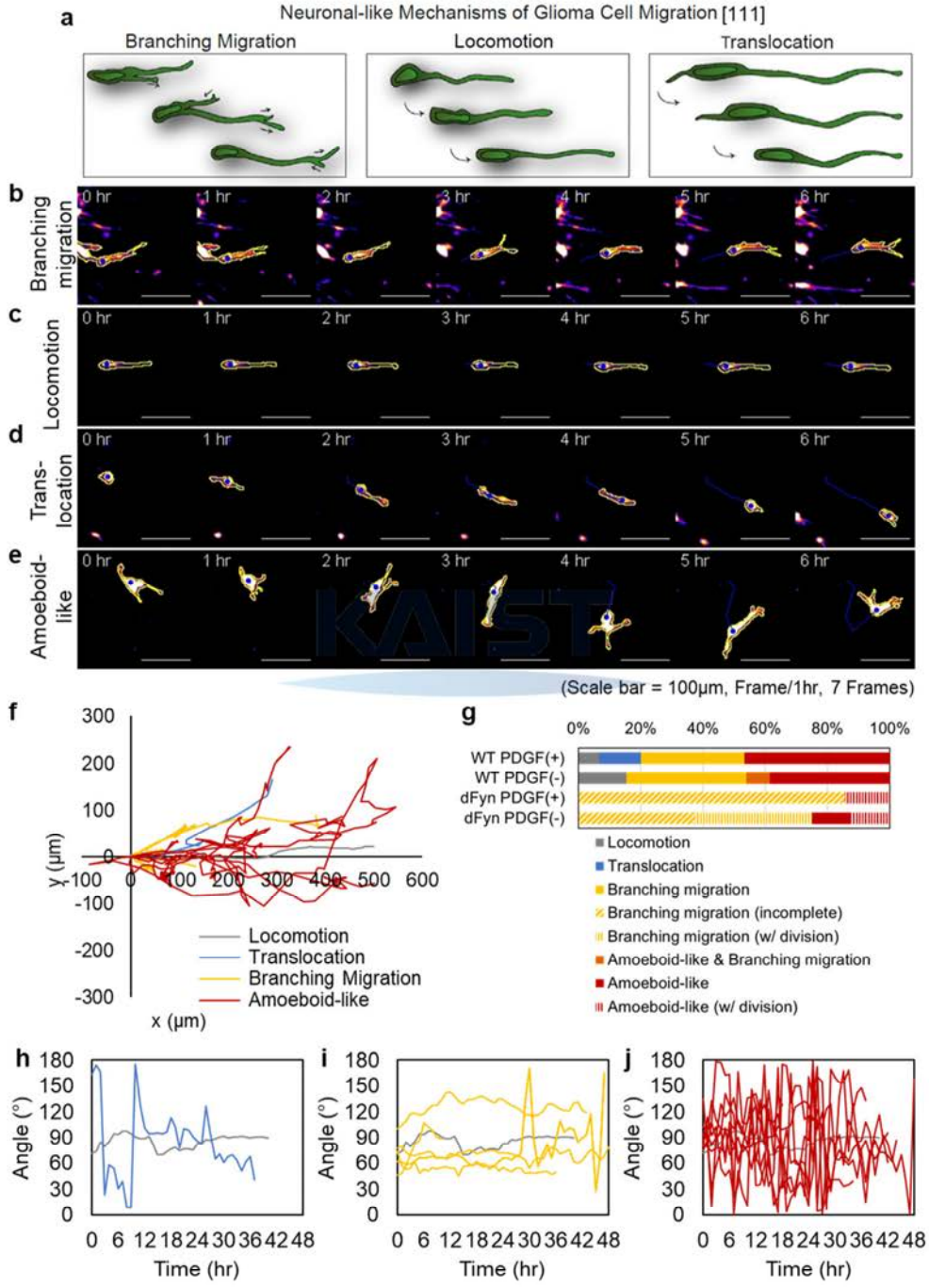

Figure 5.8 A subpopulation of scattering GBM cells features amoeboid-like migration. **a** Neuronal-like Mechanisms of Glioma Cell Migration, adopted from [111]. Examples of **b** branching migration, **c** translocation, **d** locomotion, and **e** amoeboid-like migration. **f** Trajectory plot of cells with each migration type (0~48 hours). **g** Distribution of migratory modes depending on the conditions. Angular change over time of cells migrating with **h** Translocation, **i** Branching migration, and **j** amoeboid-like migration types compared to that of locomoting cells.

5.4 Discussion

Despite the high fatality of GBM, much of the invasion mechanisms remain to be determined, mainly due to the lack of a proper model system mimicking actual human GBM. In this study, we introduced a sophisticatedly designed CRISPR/Cas9 system to establish a GBM mouse model with a highly invasive and heterogeneous signature of human GBM. Using this model, we are working on the framework of GBM invasion with the multi-scaled point of view including molecular/cellular landscapes. In an effort to better understand the mechanisms of GBM invasion, we established an *in vitro* model that allows for high-magnification studies of cellular dynamics in a controlled microenvironment. The method for generating the cellular spheroid model was also chosen regarding whether the spheroids would retain their heterogeneity. Specifically, the two candidates PDGFR and Fyn, selected through single-cell RNA sequencing, were tested on how they are involved in cellular dynamics with the *in vitro* model. As the results, we found that PDGF enables the mechanism by which the GBM cells develop long processes, and it depends on microtubule polymerization, and the Fyn kinase enables the rear retraction and is dependent on microtubule instability, respectively. Moreover, we found a very fast-moving subpopulation showing random angular changes, which is highly expected to be responsible for the distant infiltrating cells. Seen from the overall perspective, including the molecular hierarchies, the significance of PDGFR and Fyn remains to be determined. However, it is also true that invading capability of GBM is greatly attenuated if either of these pieces is missing. Through this study, we were able to establish an *in vitro* model of glioblastoma, allowing tests on multiple candidate genes and verifying cytoskeletal mechanisms. As so, it is anticipated that this finding will illuminate glioblastoma research in the future.

Chapter 6. Concluding Remarks

Human pathophysiological phenomena are so complex and multilayered that they can only be resolved when the various fields of discipline cooperate systematically, similar to how nature works. The preceding four chapters addressed one physiological phenomenon (Chapter 2.) and three pathological phenomena (Chapter 3.-5.) mainly from the physical view but also including the perspectives of the very state-of-art technologies in engineering, biology, and computational sciences.

Chapter 2 is dedicated to explaining the mechanisms by which the mature adipocytes undergo dedifferentiation. Adipocyte dedifferentiation has recently gained attention as a process underpinning adipocyte plasticity; however, a lack of suitable experimental platforms has hampered studies into the underlying mechanisms. Here, we developed a microscope-mountable ceiling culture chip that provides a stable yet tunable culture environment for long-term live imaging of dedifferentiating adipocytes. A detailed spatiotemporal analysis of mature adipocyte dedifferentiation utilizing the culture platform and Cre-recombinase tracers revealed the involvement of dynamic actin remodeling for lipid droplet (LD) secretion during adipocyte dedifferentiation. Additionally, Hippo, Hedgehog, and PPARγ signaling pathways were identified as potent regulators of adipocyte dedifferentiation. Contrary to the belief that adult adipocytes are relatively static, we show that adipocytes are very dynamic, relying on actin-driven mechanical forces to execute LD extrusion and intercellular LD transfer processes. Furthermore, there is chance to find more sophisticated mechanisms involved with the liposecretion and dedifferentiation as the lipid droplet has many contact sites for other proteins and organells[112]. Electro microscope or proximity ligation assays might push the boundaries of knowledge by revealing the endogeneous protein-protein interactions.

In Chapter 3, a brand-new ovarian cancer model reproducing whole processes of peritoneal metastasis was established. Based on this model, the question of whether a cancer cell could remember its prior mechanical microenvironment even after the long journey of metastasis was addressed. Primary ovarian tumors feature a broad range of Young's modulus, presumably resulting in cellular heterogeneity. Since cancer cells are known to alter their response to newly encountered environments depending on experiences in their previous microenvironment, we decided to investigate how exposure to varying mechanical environments impacts the cells' ensuing behaviors. To do so, we established an *in vitro* peritoneal metastasis model of ovarian cancer, which starts with mechanical priming on substrates of different stiffness. Primed cells were then aggregated into spheroids that mimic malignant spheroids in ascites. 2D spreading and 3D invasion assays were used to recapitulate the motile behaviors of the cells during peritoneal dissemination. Intriguingly, soft-primed spheroids spread slower and were less invasive than stiff-primed spheroids due to a dense actin cage enveloping the spheroids. This study confirmed that the metastatic potential of ovarian cancer could be influenced by the mechanical memory obtained from the

primary sites. Still, we have much to investigate regarding the way how the soft-primed cells build concentrated cytoskeleton structures surrounding themselves. This link will be the key to transferring the mechanical memory beyond different culture conditions.

Chapter 4 suggests cellular collectivity as a criterion for choosing an appropriate protocol for cancer spheroid generation. The cellular spheroid is considered a promising candidate for *in vitro* cancer models thanks to its structural similarity to the tumor. However, researchers are having trouble deciding on a protocol since there are so many existing methodologies already. In this study, we generated spheroidal breast cancer models using two representative methods - scaffold-free method (ULA) and scaffold-based method (Matrigel) -, and comparatively analyzed their invading modalities in 3D collagen matrices. The cells from the ULA spheroids had much higher speed, but most of the invading subpopulations scattered individually. However, in the case of Matrigel spheroids, the cells at the periphery moved slowly but in a collective manner. In the collagen matrices of higher density, the motilities of the cells in ULA spheroids were suppressed. However, the Matrigel spheroids sustained their thrust. We then quantified the contractility of each spheroid against collagen using PIV. The collagen fibers surrounding the Matrigel spheroids showed much faster and aligned movement toward the spheroidal center when compared to their counterparts. Overall, we concluded that the spheroids made with the Matrigel, which invaded more in-vivo-like and showed higher ECM contractility, should be a more suitable breast cancer model.

Finally, Chapter 5 describes the cellular dynamics of GBM cells within a highly controlled environment where the candidate molecules for invasion regulators are given or deprived conditionally. We could develop an *in vitro* model system mimicking GBM invasion thanks to the previous establishment of an advanced GBM mouse model using a very advanced CRISPR/Cas9 technique. The function of PDGFR and Fyn, two possible GBM invasion regulator molecules, in cellular dynamics was investigated using this in vitro model. We found that the PDGF helps GBM cells elongate frontal processes by involving microtubule polymerization, while the Fyn kinase helps rear retraction by governing microtubule instability.

All the chapters are devoted to improving the current *in vitro* models for human pathophysiology from physical perspectives. The differences might seem small momentarily, but it is believed to eventually contribute to practical fields, such as the drug industry and regenerative medicine. Physical approaches to cells include considerations of the three-dimensional configurations of the tissues or reflecting the physical properties of the bodily microenvironment accurately. This effort will help establish a disease model with real organism-level drug resistance or develop an efficacious scaffold for cell therapy. Therefore, continued efforts should be undertaken to integrate the physical viewpoint into the biological academy.

Bibliography

1. Morris, Samantha A., *et al.*, *Developmental Plasticity Is Bound by Pluripotency and the Fgf and Wnt Signaling Pathways.* Cell Reports, 2012. **2**(4): p. 756-765.
2. Tarkowski, A.K., *et al.*, *Development of blastomeres of mouse eggs isolated at the 4- and 8-cell stage.* Development, 1967. **18**(1): p. 155-180.
3. Piotrowska-Nitsche, K., *et al.*, *Four-cell stage mouse blastomeres have different developmental properties.* Development, 2005. **132**(3): p. 479-490.
4. Mihajlović, A.I., *et al.*, *The first cell-fate decision of mouse preimplantation embryo development: integrating cell position and polarity.* Open Biology, 2017. **7**(11): p. 170210.
5. Anani, S., *et al.*, *Initiation of Hippo signaling is linked to polarity rather than to cell position in the pre-implantation mouse embryo.* Development, 2014. **141**(14): p. 2813-2824.
6. Moris, N., *et al.*, *Transition states and cell fate decisions in epigenetic landscapes.* Nature Reviews Genetics, 2016. **17**(11): p. 693-703.
7. Nemec, S., *et al.*, *Materials control of the epigenetics underlying cell plasticity.* Nature Reviews Materials, 2021. **6**(1): p. 69-83.
8. Song, T., *et al.*, *Adipocyte dedifferentiation in health and diseases.* Clin Sci (Lond), 2019. **133**(20): p. 2107-2119.
9. Wang, Q.A., *et al.*, *Reversible De-differentiation of Mature White Adipocytes into Preadipocyte-like Precursors during Lactation.* Cell Metabolism, 2018. **28**(2): p. 282-288.e3.
10. Corsa, C.A.S., *et al.*, *Cyclical Dedifferentiation and Redifferentiation of Mammary Adipocytes.* Cell Metabolism, 2018. **28**(2): p. 187-189.
11. Zhang, Z., *et al.*, *Dermal adipose tissue has high plasticity and undergoes reversible dedifferentiation in mice.* The Journal of Clinical Investigation, 2019. **129**(12): p. 5327-5342.
12. Kruglikov, I.L., *et al.*, *The Role of Immature and Mature Adipocytes in Hair Cycling.* Trends in Endocrinology & Metabolism, 2019. **30**(2): p. 93-105.
13. Shook, B.A., *et al.*, *Dermal Adipocyte Lipolysis and Myofibroblast Conversion Are Required for Efficient Skin Repair.* Cell Stem Cell, 2020. **26**(6): p. 880-895.e6.
14. Merrick, D., *et al.*, *Skinny Fat Cells Stimulate Wound Healing.* Cell Stem Cell, 2020. **26**(6): p. 801-803.
15. Kruglikov, I.L., *et al.*, *The Role of Immature and Mature Adipocytes in Hair Cycling.* Trends in endocrinology and metabolism: TEM, 2019. **30**(2): p. 93-105.
16. Siegel, R.L., *et al.*, *Cancer Statistics, 2021.* CA: A Cancer Journal for Clinicians, 2021. **71**(1): p. 7-33.
17. Meirson, T., *et al.*, *Invasion and metastasis: the elusive hallmark of cancer.* Oncogene, 2020. **39**(9): p. 2024-2026.
18. Cortés-Guiral, D., *et al.*, *Primary and metastatic peritoneal surface malignancies.* Nature Reviews Disease Primers, 2021. **7**(1): p. 91.
19. Fares, J., *et al.*, *Molecular principles of metastasis: a hallmark of cancer revisited.* Signal Transduction and Targeted Therapy, 2020. **5**(1): p. 28.
20. Meyers, M.A., *DISTRIBUTION OF INTRA-ABDOMINAL MALIGNANT SEEDING: DEPENDENCY ON DYNAMICS OF FLOW OF ASCITIC FLUID.* American Journal of Roentgenology, 1973. **119**(1): p. 198-206.
21. Liu, J., X. Geng, *et al.*, *Milky spots: omental functional units and hotbeds for peritoneal cancer metastasis.* Tumor Biology, 2016. **37**(5): p. 5715-5726.
22. Lee, W., *et al.*, *Neutrophils facilitate ovarian cancer premetastatic niche formation in the omentum.*

Journal of Experimental Medicine, 2018. **216**(1): p. 176-194.
23. Iwanicki, M.P., *et al*., *Ovarian Cancer Spheroids Use Myosin-Generated Force to Clear the Mesothelium.* Cancer Discovery, 2011. **1**(2): p. 144-157.
24. Lambert, A.W., *et al.*, *Linking EMT programmes to normal and neoplastic epithelial stem cells.* Nature Reviews Cancer, 2021. **21**(5): p. 325-338.
25. Bakir, B., *et al*., *EMT, MET, Plasticity, and Tumor Metastasis.* Trends in Cell Biology, 2020. **30**(10): p. 764-776.
26. Semaan, A., *et al*., *Characterisation of circulating tumour cell phenotypes identifies a partial-EMT sub-population for clinical stratification of pancreatic cancer.* British Journal of Cancer, 2021. **124**(12): p. 1970-1977.
27. Vilchez Mercedes, S.A., *et al*., *Decoding leader cells in collective cancer invasion.* Nature Reviews Cancer, 2021. **21**(9): p. 592-604.
28. Zhang, J., *et al*., *Energetic regulation of coordinated leader–follower dynamics during collective invasion of breast cancer cells.* Proceedings of the National Academy of Sciences, 2019. **116**(16): p. 7867-7872.
29. Zanotelli, M.R., *et al.*, *Mechanoresponsive metabolism in cancer cell migration and metastasis.* Cell Metabolism, 2021. **33**(7): p. 1307-1321.
30. Takeshima, H., *et al.*, *Accumulation of genetic and epigenetic alterations in normal cells and cancer risk.* npj Precision Oncology, 2019. **3**(1): p. 7.
31. Wu, P.-H., *et al*., *Single-cell morphology encodes metastatic potential.* Science Advances, 2020. **6**(4): p. eaaw6938.
32. Vig, Dhruv K., *et al.*, *On the Quantification of Cellular Velocity Fields.* Biophysical Journal, 2016. **110**(7): p. 1469-1475.
33. Saraswathibhatla, A., *et al.*, *Spatiotemporal force and motion in collective cell migration.* Scientific Data, 2020. **7**(1): p. 197.
34. Style, R.W., *et al*., *Traction force microscopy in physics and biology.* Soft Matter, 2014. **10**(23): p. 4047-4055.
35. Scherer, P.E., *The many secret lives of adipocytes: implications for diabetes.* Diabetologia, 2019. **62**(2): p. 223-232.
36. Sakers, A., *et al*., *Adipose-tissue plasticity in health and disease.* Cell, 2022. **185**(3): p. 419-446.
37. Cristancho, A.G., *et al.*, *Forming functional fat: a growing understanding of adipocyte differentiation.* Nat Rev Mol Cell Biol, 2011. **12**(11): p. 722-34.
38. Fu, X., A. Zhao, *et al.*, *Dedifferentiation and Adipose Tissue*, in *Cellular Dedifferentiation and Regenerative Medicine*. 2018, Springer Berlin Heidelberg: Berlin, Heidelberg. p. 175-193.
39. Oki, Y., *et al*., *Mature Adipocyte-Derived Dedifferentiated Fat Cells Can Trans-Differentiate into Osteoblasts In Vitro and In Vivo only by All-Trans Retinoic Acid.* Cell Structure and Function, 2008. **33**(2): p. 211-222.
40. Poloni, A., *et al*., *Human AB serum for generation of mesenchymal stem cells from human chorionic villi: comparison with other source and other media including platelet lysate.* Cell proliferation, 2012. **45**(1): p. 66-75.
41. Sakuma, T., *et al*., *Mature, Adipocyte Derived, Dedifferentiated Fat Cells Can Differentiate Into Smooth Muscle-Like Cells and Contribute to Bladder Tissue Regeneration.* Journal of Urology, 2009. **182**(1): p. 355-365.
42. Poloni, A., *et al*., *Plasticity of human dedifferentiated adipocytes toward endothelial cells.* Experimental Hematology, 2015. **43**(2): p. 137-146.
43. Côté, J.A., *et al*., *Focus on dedifferentiated adipocytes: characteristics, mechanisms, and possible*

applications. Cell and Tissue Research, 2019. **378**(3): p. 385-398.
44. Côté, J.A., *et al.*, *Characterization and visualization of the liposecretion process taking place during ceiling culture of human mature adipocytes.* J Cell Physiol, 2019. **234**(7): p. 10270-10280.
45. Shin, J.H., *et al.*, *Interleukin-17A inhibits adipocyte differentiation in human mesenchymal stem cells and regulates pro-inflammatory responses in adipocytes.* Biochemical Pharmacology, 2009. **77**(12): p. 1835-1844.
46. Maurizi, G., *et al.*, *Human White Adipocytes Convert Into "Rainbow" Adipocytes In Vitro.* Journal of Cellular Physiology, 2017. **232**(10): p. 2887-2899.
47. Sugihara, H., *et al.*, *Primary cultures of unilocular fat cells: Characteristics of growth in vitro and changes in differentiation properties.* Differentiation, 1986. **31**(1): p. 42-49.
48. Côté, J.A., *et al.*, *Role of the TGF-β pathway in dedifferentiation of human mature adipocytes.* FEBS open bio, 2017. **7**(8): p. 1092-1101.
49. Harms, M.J., *et al.*, *Mature Human White Adipocytes Cultured under Membranes Maintain Identity, Function, and Can Transdifferentiate into Brown-like Adipocytes.* Cell Reports, 2019. **27**(1): p. 213-225.e5.
50. Yokomizo, A., *et al.*, *Temporal Observation of Adipocyte Microfiber Using Anchoring Device.* Micromachines, 2019. **10**(6): p. 358.
51. Kim, D., *et al.*, *Novel microwell with a roof capable of buoyant spheroid culture.* Lab on a Chip, 2021. **21**(10): p. 1974-1986.
52. Pope, B.D., *et al.*, *Fattening chips: hypertrophy, feeding, and fasting of human white adipocytes in vitro.* Lab on a Chip, 2020. **20**(22): p. 4152-4165.
53. Eguchi, J., *et al.*, *Transcriptional Control of Adipose Lipid Handling by IRF4.* Cell Metabolism, 2011. **13**(3): p. 249-259.
54. Sassmann, A., *et al.*, *Tamoxifen-inducible Cre-mediated recombination in adipocytes.* genesis, 2010. **48**(10): p. 618-625.
55. He, W., *et al.*, *Adipose-specific peroxisome proliferator-activated receptor γ knockout causes insulin resistance in fat and liver but not in muscle.* Proceedings of the National Academy of Sciences, 2003. **100**(26): p. 15712-15717.
56. Muzumdar, M.D., *et al.*, *A global double-fluorescent Cre reporter mouse.* genesis, 2007. **45**(9): p. 593-605.
57. Heallen, T., *et al.*, *Hippo Pathway Inhibits Wnt Signaling to Restrain Cardiomyocyte Proliferation and Heart Size.* Science, 2011. **332**(6028): p. 458-461.
58. Kim, M., *et al.*, *cAMP/PKA signalling reinforces the LATS–YAP pathway to fully suppress YAP in response to actin cytoskeletal changes.* The EMBO Journal, 2013. **32**(11): p. 1543-1555.
59. Madisen, L., *et al.*, *A robust and high-throughput Cre reporting and characterization system for the whole mouse brain.* Nature Neuroscience, 2010. **13**(1): p. 133-140.
60. Lin, D., *et al.*, *Adipose extracellular matrix remodelling in obesity and insulin resistance.* Biochem Pharmacol, 2016. **119**: p. 8-16.
61. O'Connor, K., *et al.*, *Extracellular matrix substrata alter adipocyte yield and lipogenesis in primary cultures of stromal-vascular cells from human adipose.* Biotechnology letters, 2004. **25**: p. 1967-72.
62. Mariman, E.C.M., *et al.*, *Adipocyte extracellular matrix composition, dynamics and role in obesity.* Cellular and Molecular Life Sciences, 2010. **67**(8): p. 1277-1292.
63. Hong, J.-H., *et al.*, *TAZ, a Transcriptional Modulator of Mesenchymal Stem Cell Differentiation.* Science, 2005. **309**(5737): p. 1074-1078.
64. An, Y., *et al.*, *Lats2 Modulates Adipocyte Proliferation and Differentiation via Hippo Signaling.*

PLOS ONE, 2013. **8**(8): p. e72042.
65. Chen, J., *et al*., *Sulforaphene Inhibition of Adipogenesis via Hedgehog Signaling in 3T3-L1 Adipocytes.* Journal of Agricultural and Food Chemistry, 2018. **66**(45): p. 11926-11934.
66. Tontonoz, P., *et al.*, *Stimulation of adipogenesis in fibroblasts by PPARγ2, a lipid-activated transcription factor.* Cell, 1994. **79**(7): p. 1147-1156.
67. Barak, Y., *et al*., *PPARγ Is Required for Placental, Cardiac, and Adipose Tissue Development.* Molecular Cell, 1999. **4**(4): p. 585-595.
68. Rosen, E.D., *et al*., *PPARγ Is Required for the Differentiation of Adipose Tissue In Vivo and In Vitro.* Molecular Cell, 1999. **4**(4): p. 611-617.
69. Wang, F., *et al*., *Lipoatrophy and severe metabolic disturbance in mice with fat-specific deletion of PPARγ.* Proceedings of the National Academy of Sciences, 2013. **110**(46): p. 18656-18661.
70. Hu, J., *et al*., *Rapid lipolytic oscillations in ex vivo adipose tissue explants revealed through microfluidic droplet sampling at high temporal resolution.* Lab on a Chip, 2020. **20**(8): p. 1503-1512.
71. Evans, A., *et al*., *Differentiating benign from malignant solid breast masses: value of shear wave elastography according to lesion stiffness combined with greyscale ultrasound according to BI-RADS classification.* British Journal of Cancer, 2012. **107**(2): p. 224-229.
72. Ciasca, G., *et al*., *Changes in cellular mechanical properties during onset or progression of colorectal cancer.* World journal of gastroenterology, 2016. **22**(32): p. 7203-7214.
73. Deptuła, P., *et al*., *Tissue Rheology as a Possible Complementary Procedure to Advance Histological Diagnosis of Colon Cancer.* ACS Biomaterials Science & Engineering, 2020. **6**(10): p. 5620-5631.
74. Masuzaki, R., *et al*., *Assessing liver tumor stiffness by transient elastography.* Hepatology international, 2007. **1**(3): p. 394-397.
75. Payen, T., *et al*., *Harmonic Motion Imaging of Pancreatic Tumor Stiffness Indicates Disease State and Treatment Response.* Clinical Cancer Research, 2020. **26**(6): p. 1297-1308.
76. Xie, M., *et al*., *Application of ReaŒ time Ultrasound Elastography for Discrimination of Low and Higˆ grade Serous Ovarian Carcinoma.* Journal of Ultrasound in Medicine, 2013. **32**.
77. Wood, C.D., *et al*., *Multi-modal magnetic resonance elastography for noninvasive assessment of ovarian tissue rigidity in vivo.* Acta Biomaterialia, 2015. **13**: p. 295-300.
78. McKenzie, A.J., *et al*., *The mechanical microenvironment regulates ovarian cancer cell morphology, migration, and spheroid disaggregation.* Scientific Reports, 2018. **8**(1): p. 7228.
79. Mieulet, V., *et al*., *Stiffness increases with myofibroblast content and collagen density in mesenchymal high grade serous ovarian cancer.* Scientific Reports, 2021. **11**(1): p. 4219.
80. Ansardamavandi, A., *et al*., *An AFM-Based Nanomechanical Study of Ovarian Tissues with Pathological Conditions.* International journal of nanomedicine, 2020. **15**: p. 4333-4350.
81. Amargant, F., *et al*., *Ovarian stiffness increases with age in the mammalian ovary and depends on collagen and hyaluronan matrices.* Aging Cell, 2020. **19**(11): p. e13259.
82. McGrail, D.J., *et al.*, *The malignancy of metastatic ovarian cancer cells is increased on soft matrices through a mechanosensitive Rho–ROCK pathway.* Journal of Cell Science, 2014. **127**(12): p. 2621-2626.
83. Fan, Y., *et al*., *Substrate Stiffness Modulates the Growth, Phenotype, and Chemoresistance of Ovarian Cancer Cells.* Frontiers in Cell and Developmental Biology, 2021. **9**.
84. Nasrollahi, S., *et al*., *Past matrix stiffness primes epithelial cells and regulates their future collective migration through a mechanical memory.* Biomaterials, 2017. **146**: p. 146-155.
85. Al Habyan, S., *et al*., *Multicellular detachment generates metastatic spheroids during intra-*

abdominal dissemination in epithelial ovarian cancer. Oncogene, 2018. **37**(37): p. 5127-5135.
86. Burleson, K.M., *et al.*, *Ovarian carcinoma spheroids disaggregate on type I collagen and invade live human mesothelial cell monolayers.* Clinical & Experimental Metastasis, 2005. **21**(8): p. 685-697.
87. Sodek, K.L., *et al.*, *Collagen I but not Matrigel matrices provide an MMP-dependent barrier to ovarian cancer cell penetration.* BMC Cancer, 2008. **8**(1): p. 223.
88. Liu, J., *et al.*, *Milky spots: omental functional units and hotbeds for peritoneal cancer metastasis.* Tumour biology : the journal of the International Society for Oncodevelopmental Biology and Medicine, 2016. **37**(5): p. 5715-5726.
89. Giménez, A., *et al.*, *Elastic properties of hydrogels and decellularized tissue sections used in mechanobiology studies probed by atomic force microscopy.* Microscopy Research and Technique, 2017. **80**(1): p. 85-96.
90. Sabass, B., *et al.*, *High resolution traction force microscopy based on experimental and computational advances.* Biophysical journal, 2008. **94**(1): p. 207-220.
91. Mertz, A.F., *et al.*, *Cadherin-based intercellular adhesions organize epithelial cell–matrix traction forces.* Proceedings of the National Academy of Sciences, 2013. **110**(3): p. 842-847.
92. Mertz, A.F., *et al.*, *Scaling of Traction Forces with the Size of Cohesive Cell Colonies.* Physical Review Letters, 2012. **108**(19): p. 198101.
93. Mohammadi, H., *et al.*, *Mechanisms and impact of altered tumour mechanics.* Nature Cell Biology, 2018. **20**(7): p. 766-774.
94. Stowers, R.S., *et al.*, *Matrix stiffness induces a tumorigenic phenotype in mammary epithelium through changes in chromatin accessibility.* Nature Biomedical Engineering, 2019. **3**(12): p. 1009-1019.
95. Jang, M., *et al.*, *Matrix stiffness epigenetically regulates the oncogenic activation of the Yes-associated protein in gastric cancer.* Nature Biomedical Engineering, 2021. **5**(1): p. 114-123.
96. Watson, A.W., *et al.*, *Breast tumor stiffness instructs bone metastasis via maintenance of mechanical conditioning.* Cell Reports, 2021. **35**(13): p. 109293.
97. Langthasa, J., *et al.*, *Extracellular matrix mediates moruloid-blastuloid morphodynamics in malignant ovarian spheroids.* Life Science Alliance, 2021. **4**(10): p. e202000942.
98. Xu, W., *et al.*, *Cell Stiffness Is a Biomarker of the Metastatic Potential of Ovarian Cancer Cells.* PLOS ONE, 2012. **7**(10): p. e46609.
99. Nath, S., *et al., Three-dimensional culture systems in cancer research: Focus on tumor spheroid model.* Pharmacol Ther, 2016. **163**: p. 94-108.
100. Nagy, J.A., *et al.*, *Why are tumour blood vessels abnormal and why is it important to know?* Br J Cancer, 2009. **100**(6): p. 865-9.
101. Bronsert, P., *et al.*, *Cancer cell invasion and EMT marker expression: a three-dimensional study of the human cancer-host interface.* J Pathol, 2014. **234**(3): p. 410-22.
102. Cheung, K.J., *et al., Illuminating breast cancer invasion: diverse roles for cell-cell interactions.* Curr Opin Cell Biol, 2014. **30**: p. 99-111.
103. Aceto, N., *et al.*, *Circulating tumor cell clusters are oligoclonal precursors of breast cancer metastasis.* Cell, 2014. **158**(5): p. 1110-1122.
104. Cheung, K.J., *et al.*, *Polyclonal breast cancer metastases arise from collective dissemination of keratin 14-expressing tumor cell clusters.* Proc Natl Acad Sci U S A, 2016. **113**(7): p. E854-63.
105. Cheung, K.J., *et al.*, *A collective route to metastasis: Seeding by tumor cell clusters.* Science, 2016. **352**(6282): p. 167-9.
106. Han, S.J., *et al.*, *Challenges of applying multicellular tumor spheroids in preclinical phase.* Cancer

Cell International, 2021. **21**(1): p. 152.
107. Nunes, A.S., *et al*., *3D tumor spheroids as in vitro models to mimic in vivo human solid tumors resistance to therapeutic drugs.* Biotechnology and Bioengineering, 2019. **116**(1): p. 206-226.
108. Nath, S., *et al.*, *Three-dimensional culture systems in cancer research: Focus on tumor spheroid model.* Pharmacology & Therapeutics, 2016. **163**: p. 94-108.
109. Kenny, P.A., *et al*., *The morphologies of breast cancer cell lines in three-dimensional assays correlate with their profiles of gene expression.* Molecular Oncology, 2007. **1**(1): p. 84-96.
110. Park, E., *et al*., *Wettability-Based Cell Sorting: Exploring Label-Free Isolation Strategy for Mixed Primary Glial Cell Population (Adv. Mater. Interfaces 22/2022).* Advanced Materials Interfaces, 2022. **9**(22): p. 2270126.
111. Venkataramani, V., *et al*., *Glioblastoma hijacks neuronal mechanisms for brain invasion.* Cell, 2022. **185**(16): p. 2899-2917.e31.
112. Herker, E., *et al*., *Lipid Droplet Contact Sites in Health and Disease.* Trends in Cell Biology, 2021. **31**(5): p. 345-358.